ÇUKUROVA UNIVERSITY
INSTITUTE OF NATURAL AND APPLIED SCIENCES

PhD THESIS

Mustafa İSTANBULLU

DESIGN AND SIMULATION OF A CARBON NANOTUBE HYBRIDIZED FIELD EFFECT TRANSISTOR BIOPOTENTIAL SENSOR

DEPARTMENT OF ELECTRICAL AND ELECTRONICS ENGINEERING

ADANA-2020

ABSTRACT

PhD THESIS

DESIGN AND SIMULATION OF A CARBON NANOTUBE HYBRIDIZED FIELD EFFECT TRANSISTOR BIOPOTENTIAL SENSOR

Mustafa İSTANBULLU

ÇUKUROVA UNIVERSITY
INSTITUTE OF NATURAL AND APPLIED SCIENCES
DEPARTMENT OF ELECTRICAL AND ELECTRONICS ENGINEERING

Supervisor : Prof. Dr. Mutlu AVCI
Year: 2020, Pages: 106
Jury : Prof. Dr. Mutlu AVCI
: Prof. Dr. Ulus ÇEVİK
: Assoc. Prof. Dr. Fatma LATİFOĞLU
: Assoc. Prof. Dr. M. Yusuf TANRIKULU
: Prof. Dr. Mustafa GÜVEN

Standard biopotential electrodes in clinical applications, require the use of electrolytic gel and skin abrasion for better electrical interface between electrode and skin. Although the pre-gelled skin electrodes present good performance for short duration measurements, signal deterioration occurs on long-duration records, since the gel dries out over a period of time. The gel may also cause skin irritation or allergic reactions. Gel-free dry electrodes are a promising alternative for long-duration recordings. However, high contact impedance, high interface potential, and low signal quality problems appear in dry electrodes. This thesis aims to design a novel carbon nanotube and metal oxide semiconductor field effect transistor based dry electrode to measure biopotentials on the human skin with high signal-to-noise ratio. The vertically aligned multiwalled carbon nanotube arrays are grown on the gate terminal of the the transistor. The multiwalled carbon nanotubes penetrate the outer layer of the skin at the microscales. This penetration eliminates the high impedance and noise effects of electrode-skin contact. The simulation results demonstrate and prove the efficiency of the proposed electrode.

Keywords: Biopotential electrodes, CNT, MWCNT, MOSFET, Semiconductor Device Microfabrication

ÖZ

DOKTORA TEZİ

KARBON NANOTÜP HİBRİDİZE EDİLMİŞ ALAN ETKİLİ TRANSİSTÖRLÜ BİYOPOTANSİYEL SENSÖR TASARIMI VE SİMULASYONU

Mustafa İSTANBULLU

ÇUKUROVA ÜNİVERSİTESİ
FEN BİLİMLERİ ENSTİTÜSÜ
ELEKTRİK - ELEKTRONİK MÜHENDİSLİĞİ ANABİLİM DALI

Danışman : Prof. Dr. Mutlu AVCI
Yıl: 2020, Sayfa Sayısı: 106
Jüri : Prof. Dr. Mutlu AVCI
: Prof. Dr. Ulus ÇEVİK
: Doç. Dr. Fatma LATİFOĞLU
: Doç. Dr. M Yusuf TANRIKULU
: Prof. Dr. Mustafa GÜVEN

Klinik uygulamalarda kullanılan standart biyopotansiyel elektrotlar, elektrot ve cilt arasında daha iyi bir elektriksel arayüz oluşturulması için jel kullanımını ve cildin aşındırılması işlemlerini gerekli kılmaktadır. Kendinden jelli olan elektrotlar kısa süreli ölçümler için iyi bir performans gösterse de, jel bir süre sonra kuruduğu için uzun süreli ölçümlerde sinyalde bozulmalar meydana gelir. Ayrıca, jel ciltte tahrişe ve alerjik reaksiyonlara neden olabilir. Jel içermeyen kuru elektrotlar uzun süreli ölçümler için umut verici bir alternatiftir. Ancak kuru elektrotlarda yüksek temas empedansı, yüksek arayüz potansiyeli ve düşük sinyal kalitesi sorunları ortaya çıkmaktadır. Bu tez çalışması, biyopotansiyelleri cilt üzerinden yüksek sinyal gürültü oranı ile ölçmek için özgün bir karbon nanotüp ve metal oksit yarıiletken alan etkili transistör tabanlı elektrot tasarımını amaçlamaktadır. Dikey yönde hizalanmış olan karbon nanotüp dizileri transistörün geçit terminali üzerinde büyütülmüştür. Çok duvarlı karbon nanotüpler deri yüzeyinin en üst tabakasına mikro ölçeklerde girişimde bulunur. Bu girişim elektrot-deri temasının yüksek empedans ve gürültü etkilerini yok etmektedir. Simulasyon sonuçları önerilen elektrodun etkinliğini kanıtlamıştır.

Anahtar Kelimeler: Biyopotansiyel elektrotlar, KNT, ÇDKNT, MOSFET, Yarıiletken Cihaz Mikrofabrikasyonu

EXTENDED SUMMARY

Many organs and tissues in the human body exhibit their health states or functions with electrical signals called biopotentials. The signals obtained from the activities of the heart (electrocardiogram), brain (electroencephalogram), or muscle (electromyogram) are examples of biopotentials. These electrophysiological signals or the other biopotentials measured from the human body enable to identify diseases.

Biopotentials are small-amplitude signals in the microvolts or millivolts, and their frequencies are between DC to several hundred hertz. Thus, the quality of the measuring electrode is crucial to acquire small amplitude signals from the skin surface with high precision. Artifacts and noises on a biopotential signal generally depend on the measuring electrodes as well as the skin surface. The surface of the human skin contains a high number of dead cells and hairs, leading to increased resistivity and decreased contact surface area with the measuring electrode.

Standard electrodes for electrophysiological signal acquisition in clinical applications, such as electrocardiography or electromyography, require the use of electrolytic gel and skin abrasion to form a better electrical interface between electrode and skin. The electrolytic gel between the skin surface and electrode, diffuses into the skin and enables forming a highly conductive layer. Although the self-gelled skin electrodes present good performance for short duration measurements, signal deterioration occurs on long-duration records, since the gel dries out over a period of time. Gel-free dry electrodes are a promising alternative for long-duration recordings. There are many different dry electrodes, from a simple disk electrode made of stainless steel to silicon-based micro-fabricated electrodes with on-chip amplifiers. However, high contact impedance, high interface potential, and low signal quality problems appear in dry electrodes due to the absence of gel.

The abovementioned problems for bioelectrodes can be solved by designing a novel electrode. This thesis introduces a novel dry electrode to measure biopotentials on the human skin with high signal to noise ratio.

Carbon nanotubes are utilized in cooperation with metal oxide semiconductor field effect transistor (MOSFET) in the proposed electrode design. Vertically aligned metallic multiwalled carbon nanotubes (MWCNTs), grown on the gate terminals of MOSFETs, form the contact surface of the electrode. The MWCNTs penetrate the high amount of dead-cell containing the outer layer of the skin for stable and improved electrical contact without the gel. The proposed electrode benefits from the MOSFET advantages such as direct charge–current conversion, and low noise pre-amplification of electrophysiological signals. The employment of the MOSFET in the electrode enables the insulation between the skin and instrumentation unit due to the electrically isolated gate terminal from the bulk structure.

After a comprehensive introduction, the state of art studies, regarding the design of an electrode, are comparatively discussed in the related works section. The aim of the chapters from third to six are to constitute a theoretical background to the reader. A general overview of the widely used bioelectrodes is given in chapter 3. Properties of an ideal bioelectrode are defined. Then, the assessment of the electrode-skin interface from the electrical aspects is done.

The skin has significant effects on the biopotentials, thus chapter 4 is devoted to the structural and electrical properties of the human skin. Properties of the electrolytic gel are also discussed in this chapter.

Carbon nanotubes are in a key position on today's and the future's technology. Chapter 5 describes the bonding of carbon atoms responsible for the excellent properties of carbon nanotubes. Structural and electronic features, as well as electron transport in a nanotube, are also explained.

In chapter 6, fundamental processes of semiconductor microfabrication are identified in a step by step manner. The growth of substrate material with the epitaxy process is followed by the thermal oxidation step to form a silicon dioxide layer. The dopant diffusion process to alter the resistivity of the substrate material is described. Ion implantation, photolithography and etching processes to form implanted regions, develop patterns on substrate and removal of some specific regions are mentioned in detail. The chapter is concluded by explaining the metallization process to build contacts.

In the 7th chapter, the electrical equivalent of utilized MWCNT is extracted. Resistance, capacitance, and inductance of individual nanotube are calculated. The utilized MOSFET in the proposed novel electrode is designed, and its microfabrication processes are performed, based on chapter 6. The source code of microfabrication processes is available in Appendix A. The MOSFET parameters are extracted from a technology computer-aided design (TCAD) simulation environment and combined with MWCNT parameters in the simulation program for integrated circuits emphasis (SPICE).

Testing of the proposed novel electrode model and conclusıon of the work take place in 8th and 9th sections. Simulations of the proposed electrode circuit equivalent and the commonly used wet electrode circuit model are compared. Two cases of skin condition are taken into consideration for comparison. They are prepared and unprepared skin cases. Electrocardiogram (ECG), electromyogram (EMG) and electroencephalogram (EEG) signals, selected randomly from the Massachusetts Institute of Technology Beth Israel Hospital database, are used as the inputs. The simulation results of the three electrode models show that, signal amplitudes, obtained from the proposed electrode model, maintains the 93.27% of the input signal, whereas the signal amplitudes taken from wet electrodes on prepared and unprepared skin surfaces retain their input amplitudes 48.26% and 0.99%, respectively. Additionally, the half-cell potential of the proposed electrode model is considerably lower than that of the wet electrodes.

The Fourier transforms of obtained biopotential signals also prove the abovementioned considerations. Contrary to the proposed electrode model, amplitudes of noise components for the biopotentials obtained from wet electrodes are increased considerably.

Although it is simulated at the worst case specifications, the proposed model obtained the highest quality signals. The signal to noise ratio of the proposed electrode is higher than that of the wet electrodes. The simulation results demonstrate and prove the efficiency of the proposed electrode.

The proposed electrode increases signal acquisition quality, reduces the noise from the stratum corneum skin layer, eliminates electrolytic gel usage, and provides stable impedance for long periods. The simulations demonstrate the efficiency and importance of the electrode. This electrode may be used without abrasion and gel-free electrophysiological signal acquisitions even for long-term measurements without biocompatibility problems.

GENİŞLETİLMİŞ ÖZET

İnsan vücudundaki birçok organ ve dokunun sağlık durumları ya da fonksiyonları biyopotansiyel olarak adlandırılan sinyallerden anlaşılabilir. Kalbin (elektrokardiyogram), beynin (elektroensefalogram) veya kasın (elektromiyogram) aktivitelerinden elde edilen sinyaller, biyopotansiyellere örnektir. Bu elektrofizyolojik sinyaller veya insan vücudundan ölçülen diğer biyopotansiyeller bazı hastalıkların tanımlanmasını sağlar.

Biyopotansiyeller, mikrovoltlar veya milivoltlardaki küçük genlikli sinyallerdir ve frekansları DC ile birkaç yüz hertz arasındadır. Bu nedenle, ölçüm elektrodunun kalitesi, cilt yüzeyinden yüksek hassasiyetle küçük genlikli sinyalleri elde etmek için çok önemlidir. Biyopotansiyel sinyali üzerindeki bozulmalar ve gürültüler genellikle ölçüm elektrotlarından ve cilt yüzeyinden kaynaklanır. İnsan deri yüzeyinin çok sayıda ölü hücre ve kıl içermesi dirençte artışa ve temas yüzeyi alanında azalmaya yol açar.

Elektrokardiyografi veya elektromiyografi gibi klinik uygulamalarda elektrofizyolojik sinyal ölçümü için kullanılan standart elektrotlar, elektrot ve cilt arasında daha iyi elektriksel arayüz oluşması için elektrolitik jel kullanımını ve cilt aşındırma işlemini gerekli kılar. Cilt yüzeyi ve elektrot arasındaki elektrolitik jel, cilt içine doğru yayılır ve oldukça iletken bir tabaka oluşturulmasını sağlar. Kendiliğinden jelli olan cilt elektrotları kısa süreli ölçümler için iyi performans gösterse de, jel bir süre sonra kuruduğundan uzun süreli kayıtlarda sinyaller üzerinde bozulmalara neden olur. Jel içermeyen kuru elektrotlar uzun süreli ölçümler için umut verici bir alternatiftir. Paslanmaz çelikten yapılmış basit bir disk elektrottan, çip üzerinde bir kuvvetlendiriciye sahip silikon bazlı mikro-fabrikasyon elektrotlara kadar birçok farklı kuru elektrot vardır. Bununla birlikte, kuru elektrotlarda jel olmaması nedeniyle yüksek temas empedansı, yüksek arayüz potansiyeli ve düşük sinyal kalitesi sorunları ortaya çıkar.

Biyoelektrotlar için yukarıda bahsedilen problemlere yeni ve özgün bir elektrot tasarımı ile çözümler getirilebilir. Bu tez çalışması insan cildi üzerinden yüksek sinyal gürültü oranına sahip biyopotansiyelleri elde etmek için özgün bir kuru elektrot tasarımına yer vermektedir.

Karbon nanotüpler, önerilen elektrot tasarımında MOSFET ile bir arada kullanılır. MOSFET'lerin geçit terminalleri üzerinde büyütülen, dikey olarak hizalanmış metalik çok duvarlı karbon nanotüpler (ÇDKNT'ler) elektrotun cilde temas yüzeyini oluşturur. ÇDKNT'ler, cildin yüksek miktarda ölü hücre içeren dış tabakasına jel olmadan, sabit ve iyi bir elektriksel temas oluşturacak şekilde az bir derinlikte girişimde bulunur. Önerilen elektrot, MOSFET'in doğrudan yük-akım dönüşümü ve elektrofizyolojik sinyalleri düşük gürültülü olarak ön-kuvvetlendirmesi gibi avantajlarından yararlanır. MOSFET'in elektrotta kullanılması, yapısı gereği geçit terminalinin transistör gövdesinden elektriksel olarak izole edilmiş olması nedeniyle, cilt ve ölçüm ünitesi arasındaki yalıtımı sağlar.

Kapsamlı bir giriş bölümünün ardından elektrot tasarımı ile ilgili karşılaştırmalı ve güncel çalışmalara, ilgili çalışmalar bölümünde yer verilmiştir. Tezin üçten altıncı bölüme kadar olan kısımları, okuyucuya teorik bir temel oluşturmayı amaçlar. 3. Bölümde, yaygın olarak kullanılan biyoelektrotların genel bir özeti verilmiştir. İdeal bir biyoelektrotun özellikleri açıklanmıştır. Daha sonra, elektrot-deri arayüzünün elektriksel açıdan değerlendirilmesine yer verilmiştir.

Cildin biyopotansiyeller üzerinde önemli etkileri vardır ve bu nedenle 4. bölüm, insan derisinin yapısal ve elektriksel özelliklerine ayrılmıştır. Elektrolitik jelin özellikleri de bu bölümde ele alınmıştır.

Karbon nanotüpler bugünün ve geleceğin teknolojisinde kilit bir konumdadır. 5. bölüm, karbon nanotüplerin mükemmel özelliklerinden sorumlu olan karbon atomlarının bağ yapılarını açıklamaktadır. Bu bölümde ayrıca, nanotüplerin yapısal ve elektronik özellikleri ile birlikte nanotüp içinde elektron iletimi de açıklanmaktadır.

Bölüm 6'da, yarı iletken mikrofabrikasyonunun temel işlemleri adım adım tanımlanmıştır. Alttaş malzemesinin epitaksi işlemi ile büyütülmesini, silikon dioksit tabakası oluşturmak için termal oksidasyon aşaması izler. Alttaş malzemesinin direncini değiştirmek için katkılama atomu difüzyonu işlemi anlatılmıştır. İmplante edilmiş bölgeler oluşturmak, alttaş üzerinde örüntüler şekillendirmek ve bazı bölgelerin kazınması işlemleri için iyon implantasyonu, fotolitografi ve aşındırma adımları ayrıntılı olarak açıklanmıştır. Bu bölüm, cihazın bağlantı pinlerini oluşturan metalizasyon işleminin açıklanmasıyla sona ermektedir.

7. bölümde, kullanılan ÇDKNT'ün elektriksel eşdeğeri çıkartılmıştır. Her bir nanotüpün direnci, kapasitansı ve endüktansı hesaplanmıştır. Önerilen özgün elektrotta kullanılan MOSFET tasarlanmış ve bölüm 6'da belirtilen mikrofabrikasyon adımları gerçekleştirilmiştir. Mikrofabrikasyon işlemlerinin kaynak kodu Ek A'da mevcuttur. MOSFET parametreleri, bilgisayar destekli tasarım programından (TCAD) elde edilmiş ve elektronik devre simulasyon programında (SPICE) ÇDKNT parametreleri ile birleştirilmiştir.

Önerilen yeni elektrot modelinin test edilmesi ve çalışmanın sonucu 8. ve 9. bölümlerde yer almaktadır. Önerilen elektrot devresi eşdeğerinin ve yaygın olarak kullanılan ıslak elektrot devre modelinin simülasyon sonuçları karşılaştırılmıştır. Karşılaştırma için cildin iki farklı durumu dikkate alınır. Bunlar ölçüm için hazırlanmış olan ve ölçüme hazır hale getirilmemiş cilt durumlarıdır. Massachusetts Institute of Technology Beth Israel hastanesi veritabanından seçilen elektrokardiyogram (EKG), elektromiyogram (EMG) ve elektroensefalogram (EEG) sinyalleri karşılaştırılan elektrotlara giriş olarak kullanılır. Üç elektrot modelinin simülasyon sonuçları, önerilen elektrot modelinden elde edilen sinyal genliklerinin giriş sinyalinin % 93,27'sini koruduğunu, buna karşın ölçüme hazır hale getirilmiş ve hazırlanmamış cilt yüzeyleri üzerinden ıslak elektrotlardan alınan sinyal genliklerinin giriş genliklerini sırasıyla % 48,26 ve % 0.99 koruduğunu göstermektedir. Ek olarak, önerilen elektrot modelinin yarı hücre potansiyeli, ıslak elektrotlarınkinden önemli ölçüde daha düşüktür.

Elde edilen biyopotansiyel sinyallerin Fourier dönüşümleri de yukarıda bahsedilen sonuçları desteklemektedir. Önerilen elektrot modelinin aksine, ıslak elektrotlardan elde edilen biyopotansiyeller için gürültü bileşenlerinin genlikleri önemli ölçüde artmıştır.

En kötü durum şartlarında benzetim gerçekleştirilmesine rağmen, önerilen modeli en yüksek kalitede sinyalleri elde etmiştir. Önerilen elektrotun sinyal-gürültü oranı, ıslak elektrotlarınkinden daha yüksektir. Simülasyon sonuçları, önerilen elektrotun verimliliğini göstermiş ve kanıtlamıştır.

Önerilen elektrot, biyolojik sinyallerin ölçüm kalitesini arttırır, stratum korneum tabakasından kaynaklanan gürültüyü azaltır, elektrolitik jel kullanımını ortadan kaldırır ve uzun süreler boyunca durağan bir temas empedansına olanak sağlar niteliktedir. Simülasyonlar, elektrotun kullanılabilirliğini ve önemini göstermektedir. Bu elektrot, biyouyumluluk sorunları göstermeden, cilt yüzeyi aşındırması işlemini ortadan kaldırarak elektrolitik iletken jel kullanımına gerek duymadan uzun vadeli ölçümler için elektrofizyolojik sinyalleri elde etmede kullanılabilir.

ACKNOWLEDGEMENTS

It has been a great learning experience working under the guidance of Prof. Dr. Mutlu AVCI. His patient advice, mentorship and support have helped me to achieve my goal in a steady and progressive manner.

I would like to thank my committee members Prof. Dr. Ulus ÇEVİK and Assoc. Prof. Dr. Fatma LATİFOĞLU for taking the time and reviewing my studies during the PhD. I would also like to thank Assoc. Prof. Dr. M. Yusuf TANRIKULU and Prof. Dr. Mustafa GÜVEN for accepting to be the member of the examining committee for my thesis.

I would like to thank Assoc. Prof. Dr.Ahmet EKİCİBİL and Prof.Dr. Supriyo Datta for giving a chance to attend their amazing solid state physics and quantum mechanics courses.

Many thanks also to my colleagues Res. Asst. Erkan ÖDEMİŞ, Res. Asst. Cemil KESKİNOĞLU and İ. Sefa ÖZYEŞİL for their valuable friendships.

I would like to thank the film crew of the Lord of the Rings and Harry Potter, for making me forget about my troubles and make me feel like I am in a different world in my exasperated moments. I don't know half of you half as well as I should like; and I like less than half of you half as well as you deserve.

I would also like to say a heartfelt thank you to my mum and dad, Yasemin-İhsan İSTANBULLU, for always believing in me and encouraging me. I am grateful to Burak and Çağrı for making me feel the meaning of brotherhood.

Last but not the least; I would like to express my deepest gratitude to my wife, Seda İSTANBULLU for her patience and support. I also thank to my little sweet daughter, my sunshine, Nehir, who always makes me smile. I promise that I will spend more time with both of you from now on.

Our Lord! Grant us from Yourself mercy and prepare for us from our affair right guidance.

TABLE OF CONTENTS **PAGES**

LIST OF TABLES **PAGE**

LIST OF FIGURES **PAGES**

NOTATIONS

R	: Universal gas constant
T	: Absolute temperature
F	: Faraday constant
M	: Mole
σ	: Sigma-bond
π	: Pi-bond
θ	: Chiral angle
E	: Energy
γ	: Bonding energy
α	: Lattice constant
k	: Wave vector
v_F	: Fermi velocity
h	: Planck's constant
c	: Speed of light
$\hbar$	: Reduced Planck's constant
q	: Charge of an electron
μ	: Mobility
n(x)	: Dopant concentration
N_B	: Background concentration
X_j	: Junction depth
ρ	: Resistivity
G_B	: Ballistic conductance
λ	: Mean free path
η	: Learning rate

LIST OF ABBREVIATIONS

EEG	: Electroencephalogram
ECG	: Electrocardiogram
CNT	: Carbon nanotube
MOSFET	: Metal oxide field effect transistor
AC	: Alternating current
DC	: Direct current
SATP	: Standard ambient temperature and pressure
SC	: Stratum corneum
MWCNT	: Multi walled carbon nanotube
SWCNT	: Single walled carbon nanotube
MBE	: Molecular beam epitaxy
PR	: Photoresist
PVD	: Physical vapor deposition
CVD	: Chemical vapor deposition
TCAD	: Technology computer aided design
DDS	: Direct digital synthesis
DSP	: Digital signal processing
ANN	: Artificial neural network
MLPNN	: Multilayer perceptron artificial neural network
DAC	: Digital to analog converter
ADC	: Analog to digital converter
DFT	: Discrete Fourier transform
LS	: Least squares
MSE	: Mean square error
PGA	: Programmable gain array
PCB	: Printed circuit board

1. INTRODUCTION

Bioimpedance, bioelectricity, and the electrical properties of tissue are pretty about similar things except for minor differences. Bioimpedance is the ability to resist (impede) electrical current flow of the related medium. Bioelectricity deals with the generating electricity ability of tissue, for example, done by the brain (electroencephalography, EEG). The electricity formed directly by the tissue itself is called *endogenic*, while the electricity that applied to the tissue for measuring bioimpedance is *exogenic*. Such electricity and the electricity externally applied for controlling the tissue are also concerned bioelectricity.

The electrical properties of tissue behave as a volume conductor or a dielectric. A dielectric material is characteristically an insulator that is capable of storing electrical energy under an electrostatic field. Tissues are generally electrolytic conductors in the frequency range smaller than 100 kHz. It is possible to extract some essential electrical parameters of tissue, such as resistive and capacitive properties, by modeling techniques even in low frequencies.

Endogenic bioelectrical signals, also called electrophysiological signals occur in the nervous, muscular, and glandular tissues originated from electrochemical activities of excitable cells. Tissues of the human body act as a volume conductor and related electrophysiological signals propagate through the tissues. Therefore, an electrophysiological signal can be measured by electrodes from the human skin surface. Tissue contacted electrodes are used in the bioimpedance and bioelectricity applications. The instrumentation device is composed of electronic circuits and cables connected to electrodes. In the instrumentation device part, charge carriers are electrons, while the charge carriers in the tissue part are ions. The electrode is a device that converts charge carriers from electrons into ions or vice versa.

The electrophysiological signals, captured on the skin surface, contain important information about concerned organ functions, whether regular or

pathological. In addition to the electrophysiological signals, there are also undesired signals due to noise, artifacts, and interference occurring in the order of microvolts or millivolts. Briefly, a biological potential must be noise-free to be clinically valuable. Since undesired signals mainly appear by depending on the measuring electrode, electrodes are crucial in terms of signal quality in a biological measurement system.

In clinical applications, standard biopotential electrodes, described in section 3.1.4, require the use of electrolytic gel and skin abrasion for better electrical interface between the electrode and skin. Since gel dries out over time, signal deterioration occurs on long-duration recordings with wet electrodes. Dry electrodes are a promising alternative for long-duration recording; nevertheless, they suffer from high contact impedance and motion artifacts. In this section of the thesis, the design of a novel MWCNT modified MOSFET based skin electrode to overcome mentioned problems is introduced.

Electrophysiological signals in the nervous, muscular, and glandular tissues originate from electrochemical activities of excitable cells. These electrical signals contain essential information about concerned organ functions, whether healthy or pathological. In addition to required bio information signals, there are also undesired signals due to noise, artifacts, and interference occurring in the order of microvolts or millivolts. Briefly, a biological potential must be noise-free to be clinically valuable. Since undesired signals mainly appear by depending on the measuring electrode, electrodes are crucial in terms of signal quality in a biological measurement system.

Electrodes made of many various materials with different arrangements can be found in the literature. Today, silver/silver chloride electrodes are the most widely used in clinical practice due to their low and stable half-cell potential, low noise level, non-polarity, and small metal–electrolyte resistance. Additionally, electrodes made of platinum, gold, and steel are also available.

While measuring electrophysiological signals from the body surface, the contact impedance between the electrode and the skin surface also has a significant effect. The surface of the skin is abraded to reduce this impedance by cleansing the skin surface from dead cells, fat layer, and hair. This process may cause pain and/or irritation of the skin surface. Furthermore, in multiple electrode measurements, it is a time-consuming process to prepare the surface for each electrode. On the other hand, measurements taken from non-abraded surfaces suffer from high electrode–skin impedance, motion artifacts, high power-line interference, and noise.

In clinical applications, a conductive electrolytic gel is generally used for increasing the conductivity and contact surface area between the skin and the electrode. The conductive gel diffuses inward through the skin surface and reduces the contact impedance. However, in long-term measurements, the gel dries out, and the measurement quality of the signal decreases gradually (Abu-Saude & Morshed, 2015). Allergic reactions on the skin surface may also occur.

In order to develop an electrode or design a novel measurement system, circuit equivalent models of skin, gel, and electrodes are required. Figure 1.1 shows the electrical equivalent circuit model of standard commonly used wet electrode in contact with skin. The use of electrolytic gel adds extra layers increasing the complexity of the electrode equivalent circuit model.

The interface between the electrode and electrolytic gel consists of a capacitance (C_d) and a resistance (R_d) parallel to each other. These components refer to the polarizing effect resulting from the ionic differences between the electrode and the electrolyte. Similarly, at the interface of electrolyte and living epidermis tissue, a potential difference (E_{se}), capacitance (C_p), and resistance (R_p) develop. Additionally, the resistive effect of the dermis and subcutaneous tissue is also modeled with a resistance (R_m).

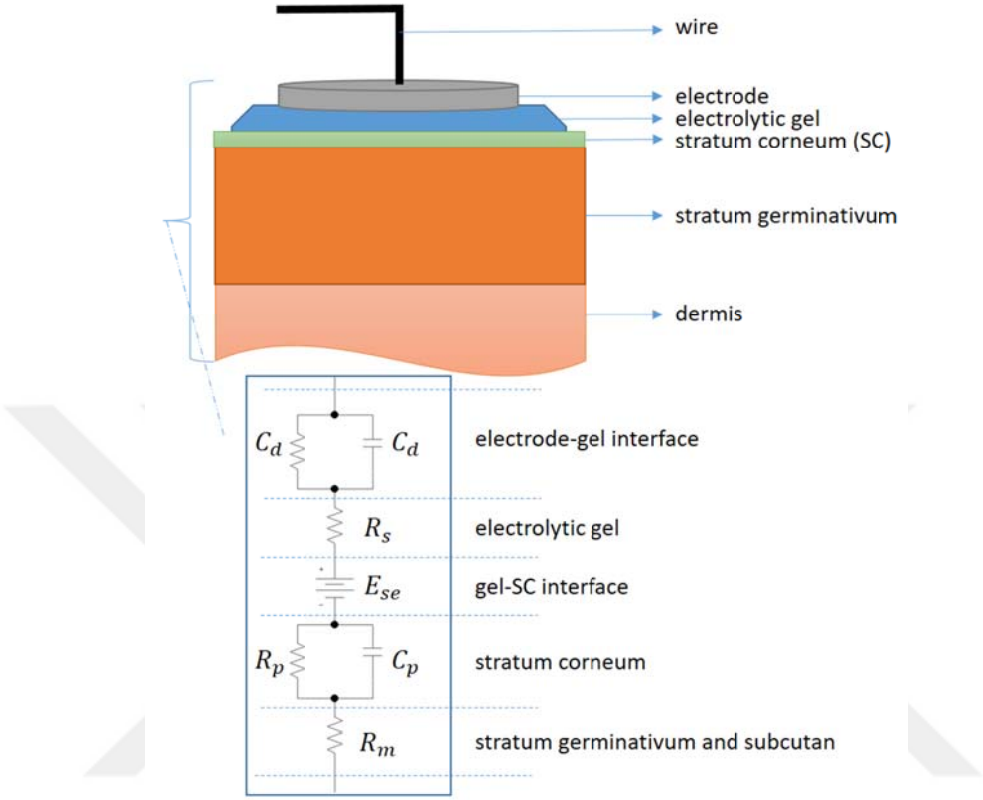

Figure 1.1 Equivalent electrical circuit model of *the standard wet electrode in* contact with the skin surface.

On the other hand, dry electrodes allowing gel-free measurements are often preferred for long-term measurements. There are many different dry electrodes, from a simple disk electrode made of stainless steel to silicon-based micro-fabricated electrodes with an on-chip amplifier. However, high contact impedance, high interface potential, and low signal quality problems appear in dry electrodes due to the absence of gel (Chi et. al., 2010).

2. RELATED WORKS

The purest form of a dry electrode is a flat conductive metal that contacts the body surface. Valchinov and Pallikarakis redesigned this electrode with a built-in amplifier to measure as successful as the wet electrodes (Valchinov & Pallikarakis, 2004). Rubber, fabric, and foam-based dry electrode types became popular with easy to use flexible structures. They also increase the contact surface (Gargiulo et al., 2008), (Mestrovic et al., 2007), (J. Yoo et al., 2009). However, conductive polymer-based promising electrodes, such as polypyrrole and polydimethylsiloxane, have contact problems to the human skin. To improve skin contact, Wang et al. have designed a polydimethylsiloxane-based electrode utilizing needle tips through hair (Wang et al., 2012). Nevertheless, the uncomfortable usage of these electrodes in the literature is unfavorable for long-term measurements (Chiou et al., 2006), (Grozea et al., 2011). Although the electrode design based on the inkjet principle using silver ink has low electrode impedance, these devices have toxicity problems (Xie et al., 2012).

The literature also includes dry biopotential electrodes designed using carbon nanotubes. Jung et al. designed an electrode consisting of a carbon nanotube and polydimethylsiloxane compound. The electrical and mechanical characteristics of the electrode were investigated depending on the density and thickness of the carbon nanotube. The electrode exhibited acceptable results despite the motion of the measured region and the sweating. Carbon nanotube utilization also exhibits biocompatibility (Jung et al., 2012). Electrocardiogram signals taken with the electrodes for seven days did not show any time-dependent deterioration. Additionally, no allergic reaction was observed on the body surface.

In general, the aforementioned dry electrodes have suffered from problems, such as low-quality surface contact with high impedance, the large potential difference at the interface, polarization, and high interface noise. Griss et al. have proposed a biopotential electrode designed by the micro-manufacturing method to

overcome these problems. In that work, the electrode has a very sharp array of needles in micron dimensions. These needles are intended to penetrate deep into the upper layer, which causes high impedance problems on the body surface. The needles were coated with silver-silver chloride. The electrode–skin impedance of the electrode designed in 4x4 mm^2 dimensions was reduced with respect to commercially available wet and dry electrodes. The electrodes also applied low amplitude electroencephalogram signal acquisition, and high measurement quality was achieved. Although these electrodes performed high-quality signal acquisition, they are not suitable for long-term measurements, in terms of hygiene, patient comfort, and safety. Additionally, researchers have noted that the electrode causes irritation and pain on the skin surface. The electrode should be disposable and must be sterilized before each use for the mentioned reasons (Griss et al., 2001).

Carbon nanotubes are also used in dry electrode designs to overcome high skin surface impedance problems by the absence of electrolytic gels as an alternative to metallic needle electrodes. The carbon nanotube utilized dry electrophysiological electrode model developed by Ruffini et al. is based on multi-walled carbon nanotubes (MWCNT) grown on a silicon disk (Ruffini et al., 2006). In the mentioned study, MWCNT arrays of 10–15 μm length with 50 nm diameter were grown on the silicon discs. Next, the silicon disk with carbon nanotubes is connected to a commercially available active electrode. The results demonstrated the robustness and affectivity of the carbon nanotube containing dry electrode with respect to commercially available Biosemi Active 2 wet electrodes (Ruffini et al., 2006).

Abu-Saude et al. investigated the feasibility of vertically aligned carbon nanotubes for dry electrodes. MWCNTs were grown on circular stainless steel to obtain the dry electrode. Carbon nanotubes were in 1–1.5 mm in length on discs with gaps ranging from 50 to 200 μm. It was observed that the vertically aligned carbon nanotube electrode has low interface impedance and comparable signal quality with respect to standard dry and commercially available wet electrodes

(GS-26, Bio-Medical Instruments, USA). In the long recordings taken over a week, a very small deterioration has occurred on signals. Although electrode attached to skin provides high signal quality, nanotubes can reach nerve cells and cause pain due to millimeter range length (Abu-saude et al., 2015).

Studies in the literature show that electrodes designed by carbon nanotubes usage in proper sizes can easily reduce the high contact impedance and overcome problems encountered in electrophysiological signal acquisition.

In this thesis, a new active electrode with an increased contact surface by utilizing carbon nanotube is proposed. Carbon nanotube utilization also provides stable contact that leads to reduce motion artifacts. Additionally, the proposed electrode overcomes the necessity of electrolytic gel. These advantages are obtained using vertically aligned metallic carbon nanotube array grown on the gate of depletion type n-channel MOSFET. MOSFET in the electrode provides some advantages for the system, such as direct charge–current conversion, high dielectric insulation between skin and instrumentation unit, and low-noise pre-amplification of electrophysiological signals.

The MOSFET parameters are extracted from a technology computer-aided design simulation environment and combined with carbon nanotube parameters in a simulation program for integrated circuits emphasis. A simulation program for integrated circuits emphasis model of the proposed electrode is interfaced with the skin circuit equivalent for integrated circuits emphasis. The proposed electrode model was compared with a wet electrode model on contact with prepared and unprepared skin. The simulation results demonstrated the efficiency and signal acquisition quality of the proposed active electrode.

3. BIOELECTRODES

Electrodes made of many various materials with different arrangements are used in the biomedical applications, including:

a. Observing electrophysiological signals such as electroencephalogram (EEG).
b. Therapeutic impulse applications such as defibrillation and transcutaneous electrical nerve stimulation.
c. Transdermal drug delivery processes by use of electrical potentials.
d. Electrical property extraction of tissues such as impedance by using the alternating current (AC) signals.

Charge carriers are ions in the tissue and are electrons in the instrumentation system. The transfer of charges between electrons and ions occurs at the electrode-skin interface. The charge transfer process has significant importance for designing an electrode. Undesirable impedances and potentials that leading distortions on the measured electrophysiological signal take place at the electrode-electrolyte interface and the electrode-skin contact.

Body-implanted electrodes are usually produced from noble and inert materials to avoid interactions with surrounding tissues. However, this choice induces arising interface impedances and potentials. Low and stable interface impedance and potential at electrode contact are imperative to minimize artifacts and distortions on measured signals. Non-implanted electrodes, in other words, external electrodes do not require noble or inert materials but generally use high electrical performance materials like silver-silver chloride (Janz & Ives, 1968). Nonetheless, by using this type of electrodes, the problem of the skin with impedance and unstable potential must be considered. Additionally to the electrophysiological signal, the potential difference between two electrode-skin

contacts is amplified by the instrumentation system. The difference amplifier part of the measurement system is saturated and could not cancel the contact potential mismatches if they were in large amplitudes. If electrode-skin contact potential mismatches are in small amplitudes and stable, it is amplified with the desired signal. Thus, a constant voltage shifting, as called *baseline-drift*, takes place on the scope screen. The baseline-drift generally not a significant problem and can easily be removed. The major problem, in this case, is a non-stable (fluctuations with time) mismatch of the contact potentials. The non-stability varies the baseline-drift, and it is no longer constant. In such a case, the filtering process is not an optimum solution since some critical components of the desired signal are eventually removed. The contact impedances in nonignorable amplitudes according to the input impedance of the amplifier also lead to signal attenuation as a result of the voltage divider effect. The contact impedance is a frequency-dependent parameter. The frequency-dependency induces a parallel capacitance at the electrode-skin interface. In the high frequencies, the impedance of the parallel capacitance effect is minimal, and no attenuation of the electrophysiological signal exists. However, low-frequency components of the desired signal can be attenuated since the impedance of the parallel capacitance effect is very large in low frequencies. The entire signal is not only attenuated but also distorted. Such a case the instrumentation system behaves as a high pass filter, and for an electrocardiogram (ECG) signal, amplitudes of P, S, T waves are reduced.

Powerline interference can be amplified together with captured electrophysiological signals due to the contact impedance mismatches. A displacement current flows through from 50/60 Hz power line to instrumentation system, patient, and ground. The displacement currents may also flow through between two electrode contacts if the contact impedances are not identical. At the differential amplifier part of the measurement system, a 50/60 Hz offset voltage proportional to the impedance mismatch occurs on the measured electrophysiological signal (Neuman, 2010).

Some other biomedical applications, such as electrical impedance tomography, apply small voltages or currents to the tissue and capture the resulting signal. Then the electrical properties of related tissue can be extracted. In these types of applications, contact impedance mismatches and magnitudes may cause distortions (McAdams et. al., 1996).

The electrical properties of the electrode-skin contacts have significant importance in biomedical applications. Ideally, an electrode-skin contact should possess the following properties.

a. Low (ideally zero) and stable electrode-skin contact potential
b. Low (ideally zero) and identical electrode-skin impedance at two contact

The contact impedance and contact potential concepts at the electrode-electrolyte and electrode-skin interfaces are described in profoundly in the following sections.

3.1.Electrical Properties of Electrode-Skin Interface

As briefly summarized in the previous section, the electrode-skin interface cause to contact impedance and contact potential that lead to distortions on the captured electrophysiological signal.

3.1.1. The Electrode-Electrolyte Potential

When an electrode is contacted to skin with an electrolyte, charge transfer over the metal-electrolyte interface takes place, as a result of oxidation-reduction reactions.

$$M \rightleftharpoons M^{n+} + ne^{-} \tag{3.1}$$

In the equilibrium circumstances, the rate of losing electrons of metal atoms is completely the same as the rate of gaining metal ions from the electrolyte. The amount of current from metal to the electrolyte is the same as current from the electrolyte to metal. Thus, the total current is zero since the currents in opposite directions cancel out each other. Although the total current at the electrode-electrolyte interface is zero, a voltage difference takes place at the interface. The voltage difference or potential depends on the charge concentrations of equilibrium given in (3.1). In general, the electrolyte is positive with respect to the metal. The potential at the interface under equilibrium conditions is called half-cell potential (Bard et al., 1944). It is impossible to measure the half-cell potential of an electrode, and researchers measure this interface potential with respect to a standard hydrogen electrode (SHE). SHE is the universal reference electrode, and its half-cell potential assumed as zero.

If two electrodes with the same metal attached to the skin, each interface constitutes the same half-cell potentials. At the input of the differential amplifier, two identical potentials cancel each other, and the effect of potential is eliminated. On the other hand, electrolyte and metal concentration differences lead to an offset voltage on the measured electrophysiological signal. The offset voltage is not a significant problem; however, fluctuations over time lead distortions on the desired signal, as stated before.

3.1.2. The Electrode-Electrolyte Impedance

Charge carriers are electrons in the instrumentation unit, while are ions in the electrolytic gel or the tissue. An electrical charge transfer occurs at the interface of electrode skin contact. When an electrode is in contact with an electrolytic gel, the ion concentration at the interface plane will be distributed. Metallic ions tend to adsorb into the gel, while ions from the gel tend to combine with metal under the effect of the electrostatic attraction. Eventually, an ion separation between the electrode and its surroundings is formed. Negatively charged metal ions are

grouped at the boundary of the electrolyte, and equal but positively charged ions are grouped at the boundary of the metal electrode. Two layers with a small distance between each other are called double-layer, and such forming acts as a capacitor. This capacitance is termed as interface capacitance, C_d (Webster, 2006).

Due to the redox reactions at the interface, given in (3.1), a dc leakage current that shunting interface capacitance, flows between the double layers. The resistance which resists to dc leakage current is called charge transfer resistance R_d and can be obtained from the Butler-Volmer equation (Rubi & Kjelstrup, 2003).

$$R_d = \frac{RT}{nF}\frac{1}{i_0} \tag{3.2}$$

where R is the universal gas constant, T is the absolute temperature (K), n is the number of electrons involved in the reaction, F is the Faraday constant, i_0 is the exchange current under equilibrium conditions.

It is obvious from the equation (3.2), interface resistance is inversely proportional to i_0. If the exchange current under the equilibrium conditions is large enough (depending on the electrode), charge transfer resistance is said to be small. A suitable electrode is characterized by small charge transfer resistance, and the desired signal can be transferred by a small voltage drop at the interface. The electrode-skin interface can be represented by an electrical circuit model shown in Figure 3.1. E_{hc} and R_s represent the half-cell potential and relatively small resistance of the electrolyte, respectively.

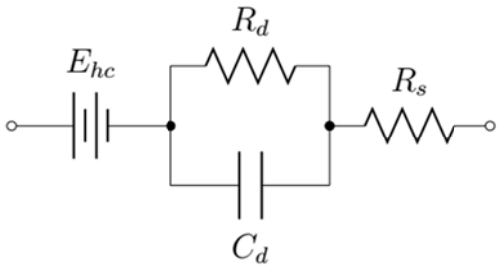

Figure 3.1 Equivalent circuit model of the electrode-electrolyte interface.

At low frequencies, the total impedance of the electrode-electrolyte interface is equal to $R_s + R_d$ since the C_d is open circuit. Note that the impedance will be varied by increasing frequency due to the frequency dependency of C_d capacitance. At a specific frequency f_0, the impedance of the C_d becomes very small compared to R_d and can be negligible. In such a case, the total impedance of the electrode-electrolyte interface is equal to only R_s.

3.1.3. Polarization

The half cell of an electrode is measured in the case of non-existence electric current between electrode-electrolyte in the standard ambient temperature and pressure (SATP) conditions (T=25°C and P=100kPa) (Council, 2011). However, the half cell potential highly depends on temperature, ionic activities, and current. The difference between reference and measured half cell potentials is called *overpotential* (Plonsey & Barr, 2007). Three specific factors cause this phenomenon. The first is current existence at the electrode-electrolyte interface. The current flow unbalances the equilibrium conditions and leads to variations on the half cell potential. The resistivity of the electrolyte also depends on the amount of current flow. Therefore a voltage drop occurs along the path of the current in the electrolyte. The second factor is the concentration overpotential. In the equilibrium conditions, redox reaction rates in both directions are equal. During the current flow, the equilibrium can not remain its conditions, and ion distribution is changed

in the electrolyte. Thus, the redox reaction balance is failed and leads to alter half cell potential. The third factor is the activation energies of the redox reactions. In the state of equilibrium, activation energies of the reactions are equal. Due to the dominance of any of these reactions in the non-equilibrium state, activation energies can not remain equal. This situation is called *activation overpotential* and causes to variations on half cell potential. Three situations described above unbalance the equilibrium conditions of the electrode and lead to change electrode interface potential. This change is defined as *polarization*.

If an electrode said to be polarizable, no current occurs between electrode-electrolyte interfaces. Polarizable electrodes show the same characteristics as an ideal capacitor. However, if a current flow through the interface, the electrode is described as non-polarizable. In practice, there not exist either perfectly polarizable or perfectly non-polarizable electrode. Characteristics of an electrode are situated between these two extremities (Yazicioglu, Hoof, & Puers, 2008).

An electrode with a small value of charge transfer resistance (R_d) can transfer the current nearly unimpeded, wastes minimum energy, leads to very low overpotential, and assumed comparatively non-polarizable (McAdams et al., 1996).

3.1.4. Electrodes For Electrophysiological Measurements

Electrodes for electrophysiological recordings are designed not only to capture biopotentials but also to reduce the noise. The design of the electrode should concentrate on obtaining biopotentials with high quality, long term usage ability, and reducing the manufacturing cost.

An electrophysiological electrode is usually excessively conductive metal that connected to the skin via an electrolytic gel (Neuman, 2010). Silver-silver chloride electrodes are commonly used in practice and have the lowest and stable interface potentials (Geddes & Baker, 1970). Measurements require the use of an electrolytic gel that generally consist of sodium-potassium chloride since the

interface characteristics are the fundamental origin of the noise. The molar concentration of the electrolytic gel is about 0.1 M and constitutes increases contact surface area between electrode and skin (Thakor, 2014). Figure 3.2a shows the typical reusable electrophysiological electrode that is generally made of silver-silver chloride disks. The electrolytic gel is typically available on the center of the electrode or applied by the practitioner externally. The electrode is fixed to the skin by an adhesive tape and wired to the instrumentation unit by a snap connector. Disposable electrodes shown in Figure 3.2b are designed with similar principles as silver-silver chloride electrodes and usually suitable for long-term applications.

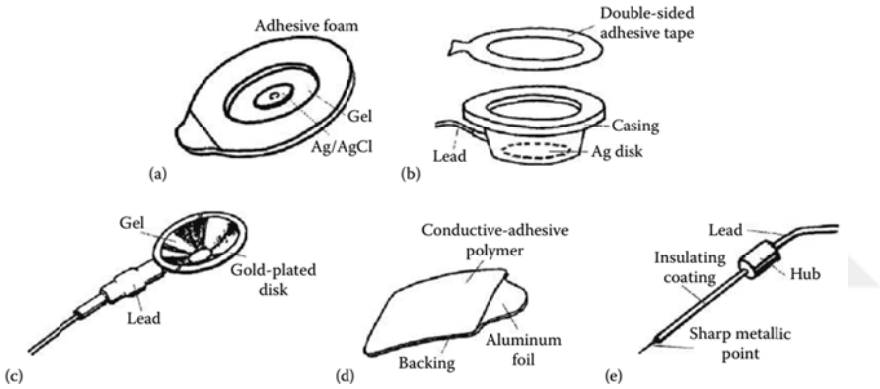

Figure 3.2 Commonly used electrophysiological electrodes: (a) Disposable Ag-AgCl electrode, (b) reusable disk electrode, (c) reusable gold electrode, (d) disposable conductive polymer electrode, (e) needle electrode (Thakor, 2014).

The gold is a highly conductive and inert material. In order to measure small amplitudes such as EEG, reusable gold electrodes given in Figure 3.2c are often preferable (Neuman, 2010). The electrode is designed as inwardly recessed to apply electrolytic gel externally (Schomer & da Silva, 2017). The elastic bandages are used to attach the electrodes on hair-free sites of the scalp. Although gold electrodes provide low interface impedance and inertness, they suffer from high

interface potential and expensiveness with respect to silver-silver chloride electrodes.

Some specific polymer materials are conductive, as well as self-adhesive and used for the electrophysiological electrode. The polymer electrode is in contact with a metallic back to constitute an electrical connection with the instrumentation unit, as seen in Figure 3.2d. These type of electrodes does not require the use of electrolytic gel. The electrical properties of polymer electrodes indicate higher resistivity and the possibility of artifact on signal than metallic electrodes. Signal to noise ratio of polymeric electrodes is also smaller than metallic electrodes. Although it suffers mentioned disadvantages, polymer electrodes are cheap and desirable for the recording high amplitude signals in the sites of restricted movement (Thakor, 2014).

Practitioners or researchers used metallic electrodes such as stainless steel in the earlier times due to its robustness and reusability; however, they are rarely preferred since high-quality and cheaper electrodes are available today (Webster, 2006). The metallic electrodes are highly resistive, noisier, and lead to generate more artifacts on the signal according to its competitors. On the other hand, due to their cheapness, reusability, and flexibility, they are preferred for electrical stimulation applications (Neuman, 2010).

In the case of recording signals not from skin surface but from tissue or organ itself are required, needle electrodes given in Figure 3.2e are used. The needle electrodes are a specific class of invasive electrodes. Its most common applications are capturing signals directly from muscle fiber, heart, or the motor unit itself. Due to this type of electrodes are invasive and have infection risks, their use is limited (Thakor, 2014).

Finally, considering the clinical requirements and designs mentioned above, a high-quality electrophysiological electrode should ensure the following electrical characteristics (Webster, 2006):

a. Low and stable interface potential.
b. Low interface impedance.
c. Low inherent noise.
d. A small value of charge transfer resistance.

4. THE SKIN

4.1.Structure of the Skin

The skin is a layered organ that covers the human body. There are three primary layers, which are named as epidermis, dermis, and subcutaneous layer. The cross-section area of the human skin is given in the Figure 4.1. The outermost layer with a thickness of about 50µm on the scalp and 100µm on the foot sole is called the epidermis. The epidermis behaves as a high strength barrier to protect the body from the environment and renews itself consistently. It is also composed of a layered structure. The outer layer, stratum corneum (SC), is highly inhomogeneous and contains compacted, flattened, and non-nucleated cells. This dead cell layer has an average thickness of about 10-15 µm.

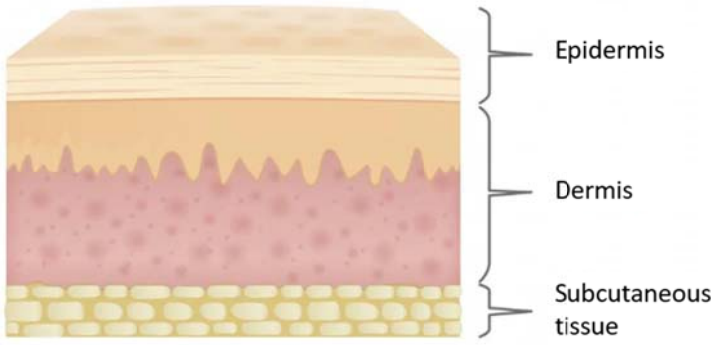

Figure 4.1 The cross-section area of the human skin

The layer containing blood vessels, hair follicles, sweat glands, and oil is called dermis. The thickness of the dermis layer is approximately 2 mm, and the nerve endings exist in this layer. Finally, the subcutaneous layer is found underneath the dermis that contains connective tissues and fat storage.

4.2.Electrical Properties Of The Human Skin

The SC layer of the skin is a highly resistive medium and exhibits high impedance to the electrical current transmission (Plonsey & Barr, 2007). The skin impedance produces the maximum contribution to the overall interface impedance. Additionally, a capacitive effect of SC layer occurs, since the SC is sandwiched between two conductive medium, the electrode, and the conductive tissue. This construction can be thought of as a parallel plate capacitor (Neuman, 2010). The circuit equivalent of the SC layer can be represented by a high-value resistance (R_p), and a capacitance (C_p), parallel to each other. The conductive subcutaneous tissue is represented electrically by a resistance (R_m).

Electrical equivalents of the skin and electrode can be combined to model the overall circuit equivalent of an electrode in contact with the skin, as given in Figure 4.2.

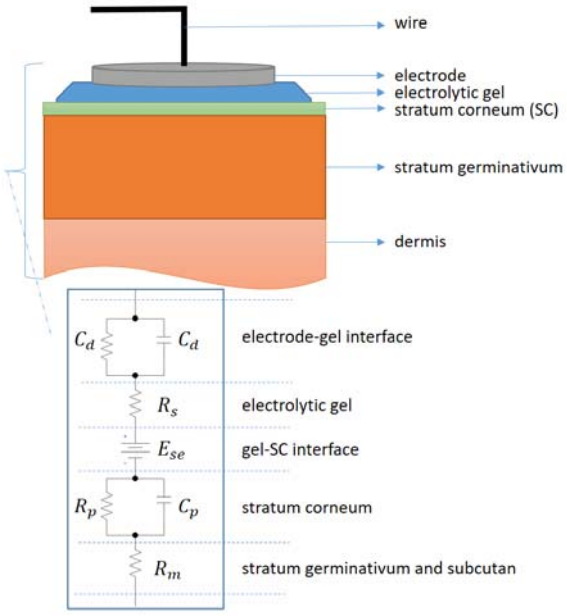

Figure 4.2 Equivalent electrical circuit model of the standard wet electrode in contact with the skin surface.

The SC layer highly determines the impedance of the human skin in the frequencies below 10 kHz. However, the impedance mostly depends on the living skin at higher frequencies. According to the literature, the SC layer causes %98 of the skin impedance at 10 Hz, while it causes only %10 at 100 kHz (Grimnes, 2014).

4.3.The Electrolytic Gel

Dry electrodes are used in some types of biomedical applications (McLaughlin, McAdams, & Anderson, 1994). Washable and reusable noncorroding electrodes such as stainless steel are available for using home environment applications; however, they suffer from their poor electrical properties. A typical dry electrode is a simple flat metal; conversely, the skin surface is crinkled. Thus, the surface area of contact is not uniform. Researches in the literature show that the dry electrode impedance decreases over time since the sweating or hydration of underlying tissue increases the contact surface area over time (Searle & Kirkup, 2000).

The electrolytic gel application increases the contact surface area between the electrode and skin that provides better electrical performance. The ions in the electrolytic gel enable the charge transfer at the interface, and therefore contact resistance is reduced (Webster & Clark, 2010).

In practice, there are mainly two types of electrolytic gels as wet gels and hydrogels. The wet gels usually consist of water, a thickening agent, a bactericide/fungicide, an ionic salt, and a surfactant (Webster, 2006). The ionic salt (generally NaCl or KCl) supplies the electrical conductance. The electrolytic gel diffuses to the skin over time and leads to a decrease in the SC layer impedance. The parallel resistance of the SC layer (R_p) also decreases exponentially over time, as seen in Figure 4.3 (McAdams & Jossinet, 2000). The duration of reaching a steady-state of skin resistance is inversely proportional to the electrolytic gel

concentration. However, the tissue can not stand with long-term application of high concentration electrolytic gel. The NaCl concentration of body fluids is about %0.9, and during the long-term high concentration gel application, skin irritation or allergic reactions may occur (Abu-Saude & Morshed, 2015).

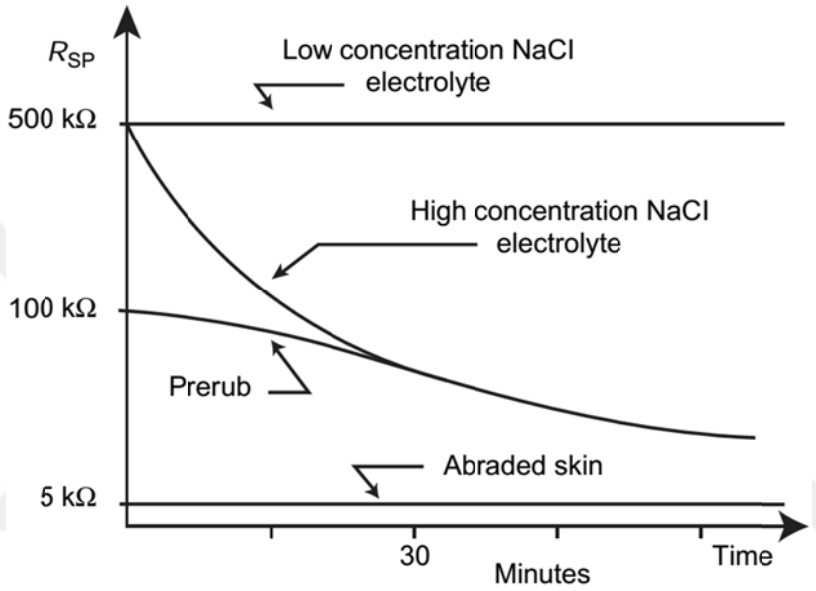

Figure 4.3 The change of skin resistance over time

The hydrogels are solid and based on the use of natural hydrocolloids. The hydrogel applications do not require the sponge in electrodes and produced by serigraphy techniques. This type of gels are preferred for flexible electrode array applications and causes fewer skin irritations. Since the gel is solid and flexible, they provide better interface contact of the electrode to the skin. However, hydrogels show more resistive properties according to the wet gels.

5. CARBON NANOTUBES

Since the discovery of multiwalled carbon nanotubes (MWCNTs) in 1991, carbon nanostructures, particularly carbon nanotubes, have attracted considerable attention due to their excellent electrical, mechanical, and chemical properties. Nowadays, CNTs are used pretty much in researches and applications such as chemical/biological separation, energy storage, composites for coating, sensors, nanoelectronic devices, and field emissions (Meyyappan, 2005). There are several synthesis methods of CNTs, such as arc discharge, laser ablation, and chemical vapor deposition. All techniques also have their variants, and all of them have advantages as well as disadvantages (Harris, 1999).

To understand its structure, a single-walled CNT (SWCNT) can be basically presumed as a rolled-up sheet of graphene, as given in Figure 5.1. CNTs are categorized according to the rolling orientation of graphene, such as zigzag, armchair and chiral. On the other hand, MWCNTs consist of many concentric shells of SWCNTs with different diameter. Thus, properties of MWCNT are pretty different from SWCNT's.

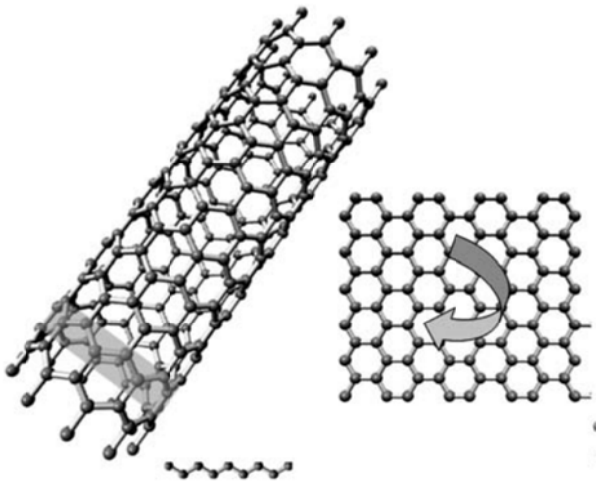

Figure 5.1 A CNT as a rolled-up graphene sheet.

5.1. Bonding of Carbon Atoms

The bonding characteristic of carbon atoms must be explained first to understand the structure and electronic properties of CNTs.

A carbon atom contains six electrons and two of them occupy the 1s orbital. Other four electrons fill the sp, sp^2 or sp^3 hybrid orbitals. These hybridized orbitals are responsible for forming of fullerene, diamond, nanotube or graphite structures as shown in Figure 5.2.

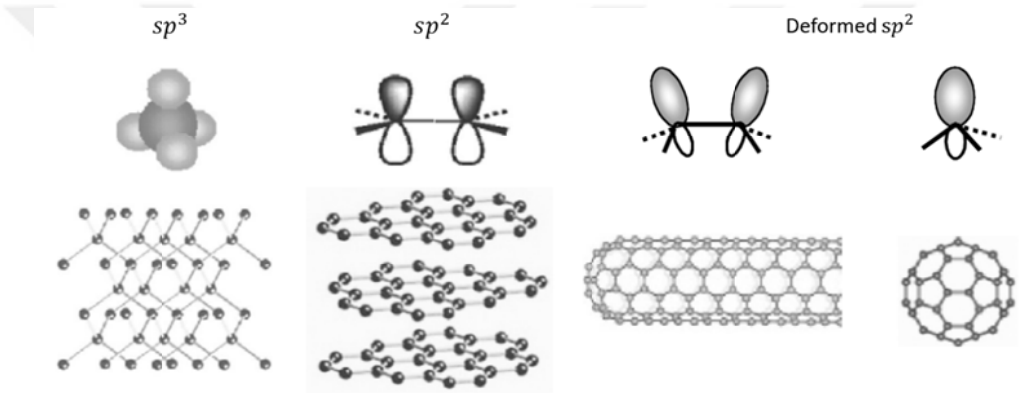

Figure 5.2 Bonding structures of carbon atoms.

In diamond, the four valence electrons of an atom forms the sp^3 hybridization (Prelas et. al., 1998). These electrons constitute four covalent σ bonds with other four carbon atoms. This bonding structure is responsible for the hardness of the diamond. Since all electrons form covalent σ bonds and nonexistence of free electrons, the diamond is electrically insulating.

In graphite, three valance electrons of a carbon atom form sp^2 hybridization in a planar structure. The three outer-shell electrons, covalent σ bonded with the other three carbon atoms, form a hexagonal sheet. Van der Waals force holds these planar sheets in parallel to each other. The space between two

successive sheets is 0.34 nm. The remaining fourth out-of-plane electron makes the graphite electrically and thermally conductive (Kelly, 1981).

As mentioned above, a carbon nanotube can be viewed as a rolled-up sheet of graphene (graphite sheet). The bonding in a nanotube is fundamentally sp^2. On the other hand, the nanotube's cylinder structure leads to quantum confinement, and $\sigma - \pi$ hybridization occurs. In this curvy structure, three σ bonds are partially out of the plane. On the contrary, π bonds are distributed over outside of the nanotube. This specific bonding structure is responsible for the unique properties of CNT. A CNT is electrically and thermally more conductive, mechanically more reliable and chemically more active than graphite.

5.2.Electronic Properties of Carbon Nanotubes

As the physical and electronic properties of CNTs are derived from those of graphene, some characteristic properties of graphene are explained concisely, and then properties of CNTs are given.

A graphite sheet, graphene, is a two-dimensional honeycomb crystal structure, as shown in Figure 5.3. It can be represented by a C vector with regard to two integers (n,m), and $n \geq m$. This set of integers corresponds to unit cell vectors of the graphene, a_1 and a_2 (Reich et. al., 2004).

$$C = na_1 + ma_2 \tag{5.1}$$

where $|a_1| = |a_2| = 0.246nm$. Diameter of the nanotube denoted as (n,m) is given in Equation 5.2.

$$D = 0.246\frac{\sqrt{n^2 + nm + m^2}}{\pi} \tag{5.2}$$

The chiral angle, θ, is given by Equation 5.3.

$$\theta = \sin^{-1} \frac{\sqrt{3}}{2\sqrt{n^2 + nm + m^2}} \tag{5.3}$$

Theoretical and experimental studies show that a carbon-carbon bond length is 0.142nm, while the spacing between two tubes is 0.34nm (Harris, 1999). Thereby, Equations (5.1) to (5.3) can be used to model and simulate different nanotube structures.

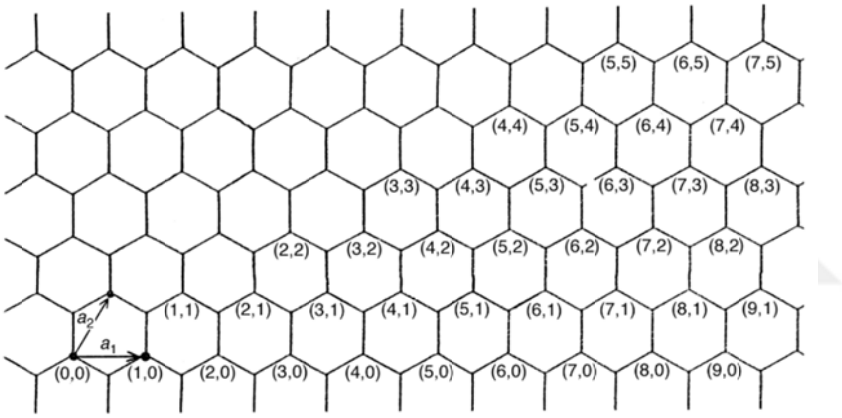

Figure 5.3 Structure of a graphene layer annotated with (n,m).

Rolling graphene in different directions results in different structure nanotubes such as zigzag, armchair, and chiral. Nanotubes in $n = m$ arrangement are called armchair, while in $m = 0$ is referred zigzag. All other (n,m) combinations are called chiral nanotubes with a specific chiral angle, θ (Meyyappan, 2005). Figure 5.4 shows the three types of SWCNTs.

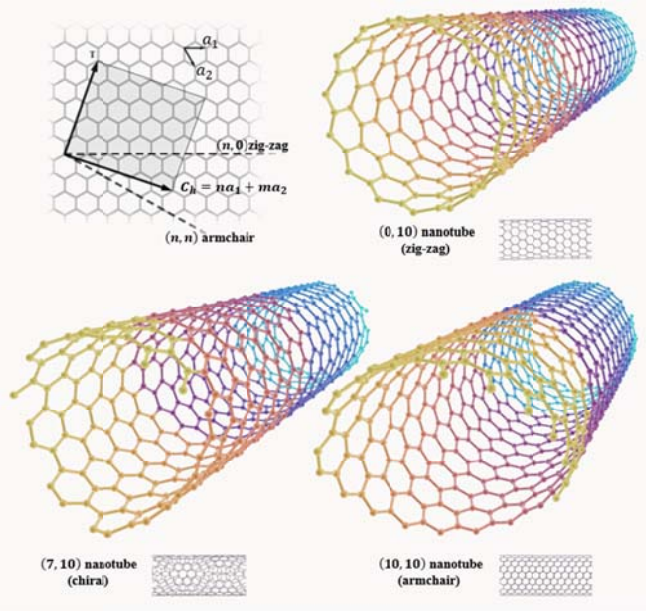

Figure 5.4 3-dimensional models of zigzag,chiral and armchair nanotubes

The rolled graphene forming CNT enables the periodic boundary conditions along the nanotube circumference (C direction). From this point, (n,m) indices not also specify the structure of CNT but also determine the conductance type. Dresselhaus et al. show that, in the condition given in Equation 5.4, metallic conduction occurs in CNT (Saito et al., 1998).

$$n - m = 3q \tag{5.4}$$

where q is an integer. As a summary, all CNTs in the armchair arrangement are metallic, while one-third of zigzag and chiral CNTs are metallic, and the others are semiconducting.

The $E - k$ function or, in other words, the dispersion relation of graphene is given in Equation 5.5 (Hanson, 2008).

$$E(k_x,k_y)=\pm\gamma\sqrt{1+4\cos(\frac{\sqrt{3}k_x a}{2})\cos(\frac{k_y a}{2})+4\cos^2\frac{k_y a}{2}} \tag{5.5}$$

where γ is the bonding energy, a is lattice constant, and (k_x,k_y) are electron wave vectors in x and y directions, respectively.

The energy dispersion diagram of the graphene crystal is shown in Figure 5.5. The circles in the figure show the $E-k$ function around the Fermi level. The energy at the Fermi level is defined as in Equation 5.6 (Hanson, 2008).

$$E=v_F\frac{h}{2\pi}k \tag{5.6}$$

where v_F is Fermi velocity, h is Planck's constant and k is the wave vector.

Dispersion for the photon is given as $E=c\hbar k$, where c is speed of light and $\hbar$ is reduced Planck's constant. The $E-k$ form of graphene is in the same $E-k$ form of photon's. Therefore, in graphene, near the π-band crossing point electrons act more like photons than particles with mass. This makes the velocity of the electrons in graphene faster than other semiconductor structures. The ballistic transport in CNT is verified by experimental studies (Fediai et. al., 2015).

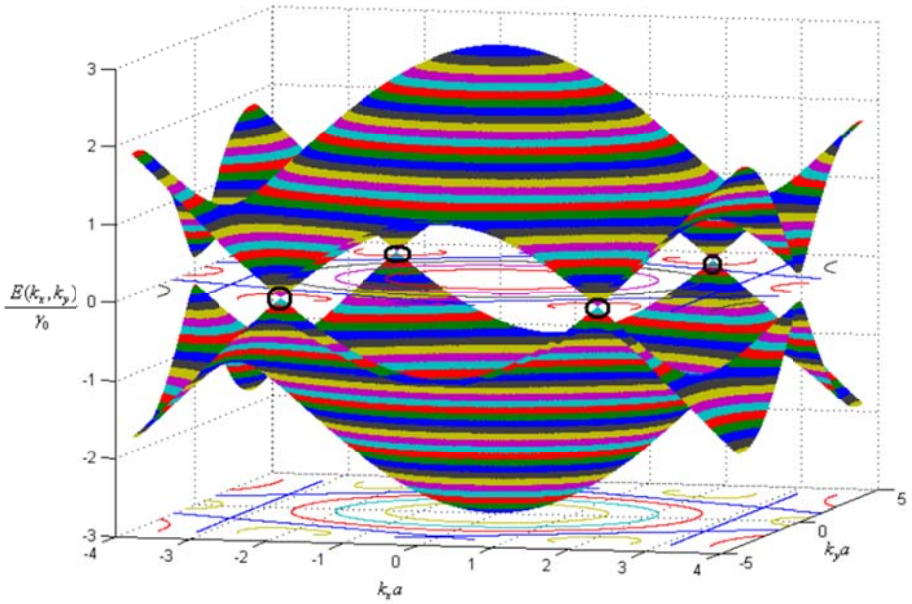

Figure 5.5 Energy dispersion of graphene

Some important physical and electrical characteristics of CNTs are listed in Table 5.1.

Table 5.1 Some characteristic properties of CNTs

Conduction Type	Metallic or Semiconducting
Electrical Transport	Ballistic
Max. Current Density	10^{10} A/cm^2
Diameter	1-100 nm
Length	Up to milimeters

6. MICROFABRICATION PROCESSES

Semiconductor manufacturing has gained a critical role in enabling technology revolution after the invention of integrated circuits (IC) in the early 1960s. Due to the developments in semiconductor fabrication, dimensions of ICs has been reduced from 20µm in 1960 to about 10nm today. In the meantime, while the manufacturing costs have decreased, the reliability and functionality of the devices have increased (Singh et. al., 2013).

Semiconductor fabrication is based on several numbers of detailed and well-organized processes. All these steps, such as *oxidation, diffusion*, and *ion implantation*, have to be studied intensively to successfully perform the whole fabrication process.

The first step of the fabrication process is subject to silicon crystal. The silicon, in its intrinsic form, is a semiconducting material. However, its electrical conductivity can be altered dramatically by doping impurity atoms into the crystal lattice. The impurity atoms, called dopant, provide holes or electrons to the intrinsic silicon crystal, called acceptor. When a silicon crystal doped with either n-type or p-type dopants, it transforms to n or p substrate. The region in the doped crystal, where the n and p substrates are in contact, is called junction. A diverse range of semiconductor devices is constructed by arranging junctions in a specific order and doping at absolute rates. The following subsections describe the fabrication process steps of a semiconductor device.

6.1. Epitaxial Growth

Epitaxy is a type of oriented crystal growth process on top of the crystalline substrate. Two fundamental types of epitaxy are homoepitaxy and heteroepitaxy. In homoepitaxy, materials of the grown crystal and substrate are the same. An oriented silicon grown process on top of the silicon wafer is an example

of homoepitaxy. The grown material can be doped or undoped (Weste & Eshraghian, 1993). Generally, diborane (B_2H_6) and phosphine (PH_3) dopants are used to form p-type and n-type doping, respectively. During the doping process, $SiCl_4$ and H gases are sprayed with the dopant. Doping concentration that changes the resistivity of the crystal is varied between 10^{13}-10^{20}/cm^3 (Allen & Holberg, 2016). Figure 6.1 shows the resistivity of a p-type and n-type silicon wafer according to dopant concentration.

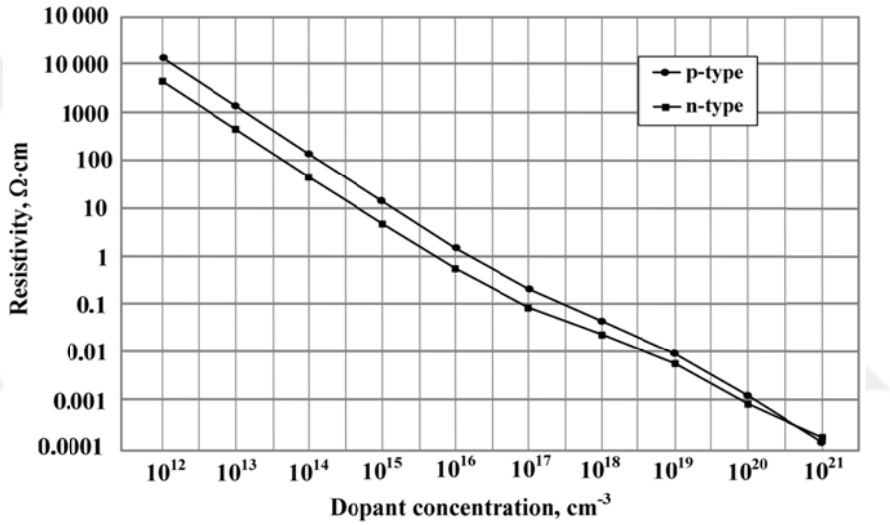

Figure 6.1 The change of n and p-type silicon wafer resistivity with a dopant concentration

The following chemical reactions of $SiCl_4$ and H express the epitaxial growth of intrinsic silicon.

$$SiCl_4 + 2H_2 \leftrightarrow Si + 4HCl \tag{6.1}$$

or decomposing silane:

$$SiH_4 \rightarrow Si + 2H_2 \quad (6.2)$$

In the epitaxial growth process, doping is performed at high temperatures as 1000-1250°C, while the pressure is traditionally at 1atm. However, molecular beam epitaxy (MBE) is used for the low temperatures (500-800°C). In heteroepitaxy, materials of the grown crystal and substrate are not the same. AlAs on GaAs, SiGe on Si or GaN on SiC are the examples of heteroepitaxy.

In this thesis, all the microfabrication process steps are simulated. The followings are the input parameters of the epitaxial growth step.

- Orientation of material
- Dopant type and concentration of wafer
- Temperature
- Growth rate
- Growth time
- Doping type and concentration of process

6.2. Thermal Oxidation

The oxidation step in semiconductor fabrication fundamentally has two goals. The first is the isolation of differen devices in a circuit or isolation of specific areas in a device. The second is to prevent doping into a material by forming a mask. Forming a SiO_2 layer is done by heating the wafer in an oxygen or water vapor containing environment. The process of using oxygen is called dry oxidation while using water vapor is called wet oxidation. Dry oxidation can be represented by following reaction,

$$Si + O_2 \rightarrow SiO_2 \quad (6.3)$$

and wet oxidation reaction is given in (6.4).

$$Si + 2H_2O \rightarrow SiO_2 + 2H_2 \tag{6.4}$$

For dry oxidation, the required temperature is about 1200°C, whereas it is usually between 900°C-1000°C for wet oxidation (Weste & Eshraghian, 1993). The thickness of the grown oxide has critical importance, and process temperature promotes the growth rate. Oxidation time, oxidation pressure, and oxidation temperature are the parameters that affect the speed of growing. Figure 6.2 exhibits the grown oxide thickness according to oxidation temperature and time.

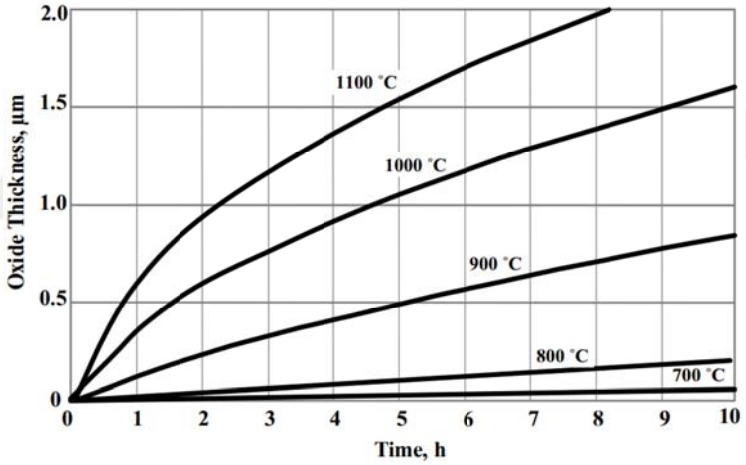

Figure 6.2 Oxide thickness alteration with time and temperature for wet oxidation

The percent of the HCl and Cl_2 (used in order to obviate metallic contamination), doping rate of the wafer, and crystal orientation are other parameters affecting the oxidation rate.

During the oxidation process, the oxide grows both sides of the silicon surface as shown in the Figure 6.3. Typically, 56% of the oxide thickness grows

upward to the Si surface, while 44% of the oxide grows inward (Allen & Holberg, 2016).

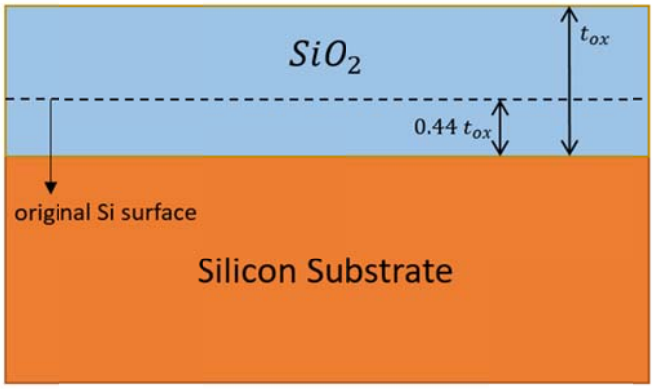

Figure 6.3 Silicon dioxide growth at the surface of a silicon wafer.

6.3. Dopant Diffusion

The aim of the doping process is adding specific atoms into the silicon wafer to modify its resistivity. The doping process also determines the type of the semiconductor as either p-type or n-type. Adding group 3A atoms of the periodic table into the Si wafer, such as boron B or gallium Ga, leads to produce p-type material, whereas group 5A atoms, such as arsenic As, antimony Sb or phosphorus P, results in n-type material. Dopant diffusion and ion implantation (described in section 6.4) are the most commonly used doping methods (Neamen, 2012).

The movement of doping atoms from the wafer surface into the bulk is called diffusion. The diffusion process can be described in two steps. The first one, deposition (or pre-deposition), is placing the high-concentration dopant atoms on the silicon surface. The solid solubility limits the amount of the diffusible dopant concentration, and it is in the range of $5x10^{20}$ to $2x10^{21}$ atoms/cm^3 (Yoo, 2008). The second one, drive-in step, is applied to distribute the dopants deeper into the wafer. During the drive-in step, an additional process is performed. An oxidation

layer is grown on the wafer surface to prevent the leak of dopants from the surface during the drive-in process.

A junction occurs between the n-type and p-type materials, after the drive-in step. Distance between the silicon wafer surface and the junction is called junction depth. The junction depth is a parameter that affects the sheet resistance of the doped layer. The sheet resistance is expressed as in equation (6.5) (Franssila, 2010).

$$\rho_s = \frac{1}{\bar{\sigma} X_j} = \frac{1}{q \int_0^{X_j} [n(x) - N_B] \mu[n(x)] dx} \tag{6.5}$$

where $q, \mu, n(x), N_B, X_j$ are charge of electron, mobility, dopant concentration, background concentration and junction depth, respectively.

In this thesis, all the microfabrication process steps are simulated. After performing the simulation sheet resistance, junction depth, and surface concentration parameters are obtained. The followings are the input parameters of the dopant diffusion step.

- Wafer orientation ((100) or (111))
- Dopant concentration level
- Dopant type
- Temperature
- Ambient (oxidizing, inert or reducing)

6.4. Ion Implantation

Ion implantation is an alternative method of doping impurity atoms to the silicon wafer. In this low temperature method, specific dopant ions are accelerated

by an electric field to high velocities and shot into the silicon wafer. The ion energy and striking angle between the ion and Si surface alter the penetration depth. The penetration depth generally varies from 0.1 to 0.6 μm (Allen & Holberg, 2012). The doping ions follow a random route in the crystal due to the scattering effects. Because of this random process, the average depth of implanted ions can be modeled using standard deviation and Gaussian distribution calculations.

The impurity ions sometimes penetrate the Si crystal more than its predicted depth. This case is called ion channelling and occurs due to the position regularity of the silicon atoms in the crystal. In order to prevent the ion channelling, the ions are implanted with an angle or implanted through the silicon dioxide. Basically tilt of an ion beam is between 7-10° (May & Spanos, 2006).

In the ion implantation process, implanted ions cause damage to the Si crystal structure. After the process, some of the implanted ions may become electrically inactive. Thermal annealing process, increasing the temperature of the semiconductor to about 800°C, leads to activate dopants in the crystal lattice. During the thermal annealing process, dopant ions are diffused deep into the silicon crystal and form the final profile (Yoo, 2008).

Both of dopant diffusion and ion implantation processes are used to insert impurity atoms into the semiconductor crystal. However, the ion implantation method has some advantages, according to dopant diffusion. The first advantage is controlling the doping more precise. Second, ion implantation can be performed at the room temperatures, except the annealing process. It permits the implantation of thin layers, as a third advantage. Additionally, the ion implantation process allows to implant dopants through the SiO_2, whereas thermal diffusion requires the surface to be free of SiO_2 or Si_3N_4 layers (Allen & Holberg, 2012).

Following parameters are inputs of the ion implantation process for the simulation.

- Wafer type
- Dopant concentration
- Ion type
- Implantation energy
- Tilt angle

6.5. Photolithography

Fabrication processes described thus far were about modifying properties of a specific region of the semiconductor wafer. These specific regions are defined by photolithography process with high precision. In the simplest terms, photolithography is the whole transferring process of a pattern to the semiconductor wafer. Therefore, the photolithography process is the most critical step of microfabrication since all the other processes depend on it (Weste & Eshraghian, 1993).

Photoresist (PR) and photomask are fundamental components of the photolithography process. The photomask, used to expose or shield some areas, represents the physical pattern of the interested region. Nontransparent sections of the photomask are made of ultraviolet (UV) light absorbing material. The photoresist is a photosensitive polymer material. When a photoresist exposed to UV light, its characteristics are altered. There are two types of photoresist: positive and negative photoresist. A region of the positive photoresist exposed to the UV light becomes soluble, whereas the unexposed region remains insoluble. For the negative photoresist, it is vice versa (Allen & Holberg, 2016).

The first step of the photolithography is the spreading the photoresist over the semiconductor substrate by spinning the wafer. The thickness of the photoresist depends on the speed of spinning. Soft bake process is performed after the applying photoresist onto wafer to get rid of the solvents. The photoresist is then exposed to the UV light through the photomask. In the next step, the exposed portions of

photoresist (in the case of positive photoresist application) is removed by a chemical solution. The exposure and removal of the photoresist process is named as developing. After the removal of unexposed photoresist, a hard bake process is applied at higher temperatures to ensure maximum adhesion of the remainder photoresist on the wafer. Thus, the hardened photoresist preserves the related regions from the etching step. The lithography process is repeated for all layers of the fabricated device. Figure 6.4 shows the basic steps up to photolithography (Neamen, 2012).

The lithography is the most complicated and expensive process of the microfabrication. The resolution, accuracy of placement, defect density are crucial problems of this process (Baker, 2019).

Following parameters are inputs of the photolithography process for the simulation.

- Photoresist coating
- Soft bake parameters
- Alignment
- Exposure level
- Post-exposure bake
- Development
- Hard bake parameters

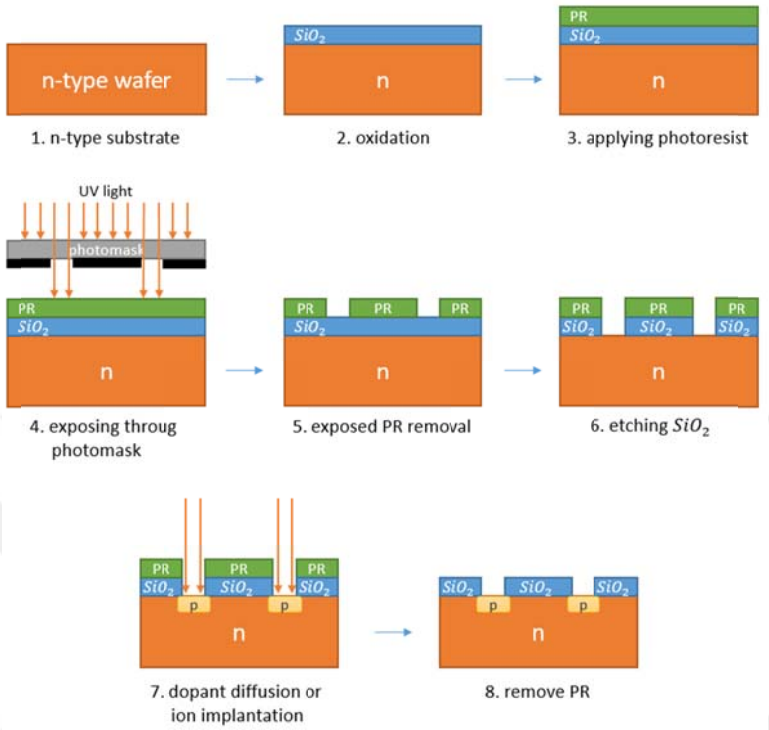

Figure 6.4 The schematic of basic fabrication steps up to photolithography process

6.6.Etching Process

The final process of semiconductor microfabrication explained here is the etching. The etching is a step of removing specific regions of materials as shown in Figure 6.4. Wet and dry etching (or plasma etching) are two basic methods in use. In the wet etching method, etchants in liquid form are applied for removing parts, and some chemical reactions occur. However, etchants in gas form, like chlorofluorocarbons, are used for the dry etching process (Stepanova & Dew, 2011).

For now, the illustration shown in Figure 6.5 (a) is assumed to be etched. A silicon wafer is coated by two thin layers (SiO_2 and PR) as shown in the figure. A PR layer covers the thin SiO_2 layer except for a part where to be etched. The aim of

the etching process is the removal of the SiO2 layer existed in the uncovered PR section (Allen & Holberg, 2012).

Figure 6.5 (a) A structure ready for etching and (b) result of etching

To understand the etching process deeply, the *selectivity* and *anisotropy* issues have to be considered. The selectivity is the etching rate of the just desired portion, with no effect on the other parts. The mathematical definition of selectivity is given in Equation 6.6.

$$S = \frac{Etching\ rate\ of\ desired\ porion}{Etching\ rate\ of\ undesired\ portion} \tag{6.6}$$

The anisotropy is the etching rate in only one direction. However, just a perfect anisotropic etchant etches in one direction only. The level of anisotropy is defined as Equation given in 6.7 (Cui, 2009).

$$A = 1 - \frac{Lateral\ ething\ rate}{Vertical\ etching\ rate} \tag{6.7}$$

There is no etchant have either perfect selectivity or perfect anisotropy in the practice. Figure 6.5 (b) illustrates the result of an etching process. In the figure,

dimensions a and b represent the lack of selectivity with respect to PR and n-type substrate, respectively, whereas the dimension c shows the level of anisotropy.

The most commonly used wet etchants to etch silicon dioxide, silicon nitride and silicon are hydrofluoric acid, phosphoric acid and potassium hydroxide, respectively. Nitric acid, acetic acid and hydrofluoric acid are used to etch polysilicon layer, whereas phosphoric acid mixture is used for etching metal layers. In the wet etching process, the etching rate and resulting surface quality strongly depend on the chemical composition mentioned above, temperature and agitating. Therefore, it is difficult to control the etching with high precision and for desired geometries (Papadopoulos, 2016).

Reactive ion etching (RIE) is the most common dry etching method in practice. In this method, a radio frequency (RF) power supply energizes the ions in the gas to the desired energy state. The field of interest is then exposed to the energized gas and the etching process starts. The energy of RF power supply, gas flow rate and pressure has to be well optimized to achieve quality ethching. Trifluoromethane and tetrafluoromethane are used to etch silicon dioxide and silicon nitride, whereas oxygen is used to remove the photoresist (May & Sze, 2004).

6.7.Metallization Process

The metallization is forming metal films on the wafer surface to contact devices or device terminals. In this step metallic or alloy layers, such as Al, Cu, Ag, Au, Pt, TiN or TiW, can be formed. The resistance of these interconnects can be calculated by Equation 6.8 (Yoo, 2008).

$$R = \rho \frac{L}{Wh} \tag{6.8}$$

where ρ is resistivity and L,W,h are length, width and thickness, respectively. The resistance of thin films is greater than thick ones, as also understood from the equation. Generally, the thickness of the metallization is around 0.5-2μm. The list of commonly used metals for the metallization process and some of their characteristic properties are given in Table 6.1. Since the resistivity is highly dependent on the deposition process, data in the table should be used just as guidance (Franssila, 2010).

Table 6.1 Properties of metals for the metallization process

Metal	Resistivity (μΩ.cm)	Coef. of Thermal Expansion (ppm/°C)	Thermal conductivity (W/cm.K)	Melting point (°C)
Al	3	23	2.4	650
Cu	1.7	16	4	1083
Au	1.7	14	3	1064
Ag	1.6	19.2	4.2	961
Mo	5.6	5	1.4	2610
W	5.6	4.5	1.7	3387
Ta	12	6.5	0.6	3000
Ti	48	8.6	0.2	1660
Co	6.2	12.5	0.7	1500
Ni	6.8	13	0.9	1455
Cr	13	6	0.7	1875
Pt	10	9	0.7	1064

Noble metals, such as Au and Pt, do not adhere to the semiconductor substrates strongly. In those cases, adhesion layers, such as Ti or Cr, are required. Sometimes a barrier layer is needed to prevent undesired reactions between thin films. Tungsten nitride, titanium-tungsten, tantalum nitride and titanium nitride are used as the barrier layer (Cui, 2009).

Physical vapor deposition (PVD) is a fundamental method for the metallization process. In this method, metal atoms, i.e., Al, are vaporized to the substrate and deposited on the surface layer by layer to form a thin film (May & Spanos, 2006).

Electron beam evaporation and *sputtering* are widely used techniques in the PVD process. In the electron beam evaporation technique, the Al source is evaporated by an electron beam, and Al atoms are produced. The heated and vaporized Al atoms are then deposited on the semiconductor wafer surface. In the sputtering technique, a high energy argon atom beam is bombarded to the Al source and results in displacement of Al atoms from the source. These displaced (or sputtered) Al atoms are then deposited on the semiconductor wafer surface. The sputtering technique is more preferred than electron beam evaporation. The semiconductor wafer is rotated continuously during the PVD process to obtain uniform deposition (Allen & Holberg, 2016).

The chemical vapor deposition (CVD) is also used for metallization process and has several advantages compared to PVD, such as excellent step coverage, large throughput and low-temperature processing. In the CVD method, the process chamber is filled with highly reactive organo-metallic aluminium gas. The molecules in the compound are applied to the surface of the semiconductor wafer and chemical reactions start by increasing temperature. During the chemical reactions, the molecules on the heated wafer are decomposed and Al atoms get deposited on the surface. The process leads to form a thin Al film on the semiconductor surface. In CVD method several type thin films, such as Al, Cu, WSi_2, TiN or W, can be formed (Papadopoulos, 2016).

7. DESIGN OF MWCNT MODIFIED MOSFET BASED SKIN ELECTRODE

7.1.Circuit Equivalent Model of Metallic MWCNT

A carbon nanotube can be viewed as a rolled-up sheet of graphene with a diameter typically between one and two nanometers (Krueger, 2014). The nanotube can be either metallic or semiconducting, depending on how it is rolled up from the graphene sheet. The electron transfer rate of carbon nanotube tip 10^5 to 10^6 times higher than its lateral surface (Charlier & Roche, 2007). This makes the carbon nanotube a very convenient material for taking signals from its tip and transmitting them to any instrumentation circuit. Carbon nanotube utilized electrodes can acquire the signal with high quality and less noise. They can be adapted to up-to-date platinum, gold, or silver chloride electrodes. Additionally, the transmission in a carbon nanotube is ballistic in certain cases (Datta, 2005).

The proposed electrode is modeled by considering the individual MWCNT model. It is crucial to characterize the response of the MWCNT to obtain efficient model extraction. During this task, the physical structure of MWCNT is taken in the consideration in detail. A schematic of only one metallic MWCNT grown on the gate of the depletion type MOSFET is shown in Figure 7.1. The diameter of the outermost shell is $D_{\max}$, the innermost shell is $D_{\min}$, and the gap between the two neighboring shells is $d = 3.4$ Å, which is the van der Waals gap. In order to simulate the proposed electrode, the circuit equivalent of MWCNTs has to be modeled. During this modeling resistance, inductance and capacitance are used to express the electrical characteristic of metallic MWCNT.

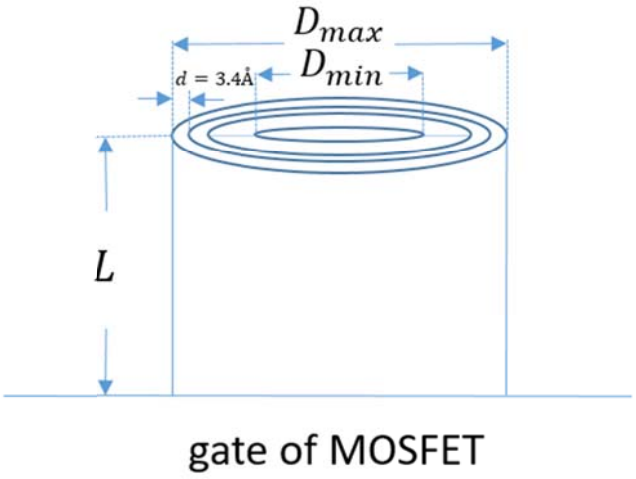

Figure 7.1 Schematic of MWCNT on the gate terminal of MOSFET

7.1.1. Resistance

The number of occupied sub-bands in a carbon nanotube, making a contribution to conduction, is dependent on the chirality of the carbon nanotube. The probability of a sub-band being occupied can be represented by Fermi distribution function,

$$f = \frac{1}{e^{\left(\frac{|E_i - E_f|}{KT}\right)} + 1} \tag{7.1}$$

where E_i is the peak value for the sub-bands below the Fermi level E_f. According to the study by Banerjee and Srivastava, the number of conducting channels in any shell by considering the spin degeneracy can be acquired by adding up all of the probabilities (Banerjee & Srivastava, 2006).

$$N_{shell} = \sum_{sub-bands} \frac{1}{e^{\left(\frac{|E_i - E_f|}{KT}\right)} + 1} \tag{7.2}$$

Naeemi and Mein proposed an approximate form of the number of the shell as in Equation 7.3. In this thesis, this approximate form of the number of shell equation is used as:

$$N_{shell}(D) = a.D + b \qquad if \quad D > 3nm \tag{7.3}$$

where D is diameter of the shell, $a = 0.0612nm^{-1}$ and $b = 0.425$ (Naeemi & Mein, 2006). The ratio of diameters of the innermost shell to the outermost shell assumed approximately to be 1/2 (Naeemi & Mein, 2006), (Li et al., 2005). Thus, the number of shells p of the MWCNT can be determined by Equation 7.4.

$$p = \left[\frac{D_{\max} - D_{\min}}{2d} \right] + 1 \tag{7.4}$$

where the integer part of the calculation obtained from the expression in the brackets is taken in to account. If the shells from outer to the inner are indexed as $1, 2, ..., i, ..., p$ the diameter of the i^{th} shell is given by the following expression.

$$D_i = D_{\max} - 2d(i-1), \qquad 1 \le i \le p \tag{7.5}$$

Additionally, the number of conducting channels of the i^{th} shell is described by Equation 7.6.

$$N_i = a.D_i + b \tag{7.6}$$

Thus, the total conducting channel number is the sum of conducting channels of all the shells.

In the case of ballistic transport for a single-walled carbon nanotube (SWCNT), the conductivity is independent of the nanotube lengths.

$$G_{SWCNT} = \frac{2q^2}{h} xN \tag{7.7}$$

where q, h, N are charge of electron, Planck's constant, and number of the conductive channels in a nanotube, respectively. Since the mechanical durability of MWCNT is higher than for SWCNTs, MWCNT was used in the proposed structure of this work. The conductivity of an MWCNT in the case of ballistic transport is given as follows (Datta, 2012).

$$G_{MWCNT} = nmG_B T \tag{7.8}$$

where n is the number of the shell, m is the number of modes, G_B is the ballistic conductance $(2q^2 / h)$, and T is probability of an electron transmission in carbon nanotube. Experimental studies show that MWCNTs can exhibit ballistic transport up to several micrometers in length (Hanson, 2008).

The length of the MWCNT designed in this study is about 100 μm. This length is much larger than the mean free length of the carbon nanotube. According to Park et al., the main reason for the resistance of carbon nanotube is the scattering originating from acoustic phonons (Park et al., 2004). The nanotube resistance for lengths exceeding the mean free path varies depending on the length.

$$R = \frac{h}{4q^2}\left(1 + \frac{L}{L_m}\right) \tag{7.9}$$

where L and L_m are the length of carbon nanotube and the mean free length of carbon nanotube, respectively. Similarly, the resistance of an MWCNT whose length is much longer than the mean free length is given by:

$$R_{MWCNT} = \frac{h}{2q^2 N}\left(1 + \frac{L}{L_m}\right) \tag{7.10}$$

The total resistance of a metallic carbon nanotube (R_{CNT}) can be divided into three parts (Yamacli & Avci, 2009): the quantum resistance $(R_{quantum})$, length-dependent resistance (R_{length_dep}) and voltage-dependent resistance (R_{volt_dep}) given by,

$$R_{CNT} = R_{quantum} + R_{length\_dep} + R_{volt\_dep} \tag{7.11}$$

According to Hanson, at low voltages, the length-dependent resistance equation given above keeps its validity up to centimeter lengths (Hanson, 2008).

In this work, electrophysiological signals with low amplitude voltages are applied to carbon nanotubes. As seen in Table 7.1, since the voltage range of biopotentials is between 5 μV and 100 mV, the low voltage excitation condition of carbon nanotube is provided.

Table 7.1 Voltage and frequency ranges of the fundamental electrophysiological signals

Signal	**Voltage Range**	**Frequency Range (hz)**
Electrocardiogram, ECG	0.5-4 mV	0.01-250
Electroencephalogram, EEG	5-300 μV	DC-150
Electromyogram, EMG	10-1000 μV	DC-1
Electrogastrogram, EGG	0.5-100 mV	DC-1
Nerve cell potential	0.01-3 mV	DC-10000

Under low voltage excitation, the total resistance equation of the carbon nanotube can be simplified as Equation 7.12 by neglecting the voltage-dependent resistance.

$$R_{CNT} = R_{quantum} + R_{length\_dep} \tag{7.12}$$

The value of the intrinsic resistance of a shell can be determined by;

$$R_{shell} = R_{quantum} + R_{length\_dep} = \frac{h}{2q^2 N} + \frac{h}{2q^2 N}\frac{L}{\lambda} \tag{7.13}$$

where $h/2q^2 = 12.9k\Omega$ and L, λ, N are the length, the mean free path, and number of conducting channels of the shell, respectively (H. Li et al.,2008). In Equation 7.13, the mean free path has a significant effect on determining the resistance of carbon nanotube. In a metallic or semiconducting MWCNT, the mean free path of a shell always depends on the diameter of the corresponding nanotube, approximately $\lambda \approx 1000D$ (H. Li et al., 2008).

In addition to shell resistances, intershell resistances, (R_{is}), must also be taken into consideration for MWCNT. The magnitude of an intershell resistance is constant and is given by $R_{is} = 10k\Omega/\mu m$ (Bourlon et al., 2004). Assuming all the inner shells are in conduction, the total resistance of the MWCNT can be calculated by using parallelism of the shell resistances as given by Equation 7.14 (Kordrostami et al., 2008).

$$R_{total} = \frac{1}{\sum_{shells} \frac{N(D)}{R_Q\left(1 + \frac{L}{1000D}\right)}} \tag{7.14}$$

In this thesis, according to mentioned explanations, quantum resistance, length-dependent resistance, and intershell resistance are used for modeling resistance of MWCNTs.

7.1.2. Inductance

The inductance of MWCNT is similar to that of SWCNT composed of kinetic (L_K) and magnetic (L_M) inductance (Burke, 2002). The kinetic inductance and magnetic inductance expressions are given in Equations 7.15 and 7.16, respectively.

$$L_K = \frac{h}{2q^2 v_F} = 16nH / \mu m \tag{7.15}$$

where h, q, v_F are Planck's constant, charge of an electron, and Fermi velocity, respectively.

$$L_M = \frac{\mu}{2\pi} \cosh^{-1}\left(2H / D\right) \tag{7.16}$$

where μ is permeability and H is the distance between carbon nanotube and ground plane. Since the magnetic inductance is much smaller than the kinetic inductance, it has not been included in the MWCNT model.

7.1.3. Capacitance

The capacitance of MWCNT consists of two parts as quantum capacitance (C_Q) and intershell capacitance (C_{int}). The quantum and intershell capacitance expressions are given as in Equations 7.17 and 7.18.

$$C_Q = \frac{2q^2}{hv_F} \approx 100aF / \mu m \tag{7.17}$$

where q, h, v_F represent charge of an electron, Planck's constant, and Fermi velocity, respectively.

By using the coaxial capacitance formula, the shell-to-shell capacitance can be defined by,

$$C_{\text{int}} = \frac{2\pi\varepsilon}{\ln\left(D_{out} / D_{in}\right)} = \frac{2\pi\varepsilon}{\ln\left(D_{out} / \left(D_{out} - 2d\right)\right)} \tag{7.18}$$

Where D_{out} represents the diameter of the exterior shell, and D_{in} is the diameter of the interior shell. Since all of the conducting shells in each MWCNT are connected to the same metal on the gate terminal of the MOSFET, the effective shell-to-shell capacitance is bypassed.

7.1.4. The Final Circuit Equivalent of the MWCNT

An MWCNT consists of many concentric shells of different diameters. Thus, each shell has different mean free paths and different circuit parameters. The resistance of carbon nanotube depends on the number of channels where the nanotube diameter specifies them. The mean free path also depends on the diameter of the carbon nanotube.

Based upon the analysis mentioned above, the circuit equivalent of a shell is composed of quantum resistance, length-dependent resistance, and kinetic inductance connected in series. In this manner, the circuit equivalent of MWCNT is composed of circuit equivalents of all the concentric shells in parallel, as shown in Figure 7.2. Additionally, intershell resistance and quantum capacitance

components are in parallel between successive shells (H. Li et al., 2008). In the model used in this work, intershell capacitances are neglected for MWCNT.

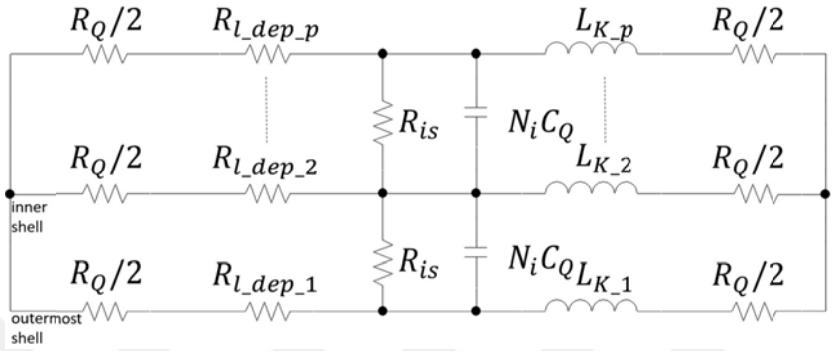

Figure 7.2 Equivalent circuit model of an MWCNT with p shell

Since the carbon nanotubes grown on the gate terminal of the MOSFET are vertically aligned and arranged in parallel, the resistance of carbon nanotube forest can be expressed by Equation 7.19.

$$R_{CNT\ forest} = \frac{R_{total}}{\#of\ CNT} \tag{7.19}$$

If the carbon nanotubes are grown with 50 µm successive spacing, the total number of carbon nanotubes is approximately 10^4 for an electrode designed with dimensions of 5 mm x 5 mm. Thus, the interface resistances of carbon nanotubes are extremely reduced in the overall electrode model.

7.2.Design and Microfabrication of The Proposed MOSFET

7.2.1. MOSFET Type Selection

The MOSFET is fundamentally three-terminal semiconductor device that the current flowing between two terminals is controlled by the third terminal

voltage. Figure 7.3 shows the physical structure of the n-channel enhancement-type MOSFET. The transistor shown in the figure is fabricated on a p-type substrate. Two heavily doped n-type regions represent the source and drain terminals. Electrically insulator thin silicon dioxide layer is grown on the substrate surface between source and drain regions. The metal covering the oxide layer is called the gate terminal.

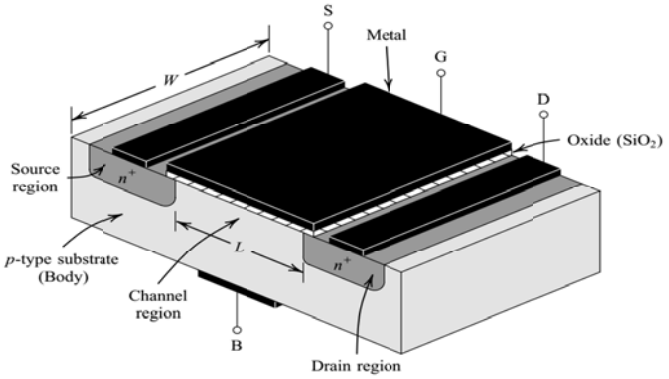

Figure 7.3 Basic physical structure of n-type enhancement MOSFET

Assuming the drain terminal is positively charged according to the source terminal, connecting the substrate to the source terminal makes two pn junctions cut off. A positive voltage higher than the threshold has to be applied on the gate terminal to permit current flow from drain to the source by forming an electron inversion layer.

In this thesis work, low-amplitude electrophysiological signals, some of them listed in Table 7.1, are signals to be measured. As seen in the table, the maximum amplitudes of the signals are about 100mV. The proposed electrode model explained in the next chapter in detail requires MOSFET utilization to convert the biopotential to an amplified current form, and the MWCNT's, capturing signals from the skin surface, are connected to the gate of the MOSFET. Thus, the threshold of the MOSFET has to be low enough to be ON state for all

biopotentials, or the MOSFET has to operate in the saturation region continually. Another type of MOSFET, depletion mode, is selected to fulfill the requirement.

The depletion type MOSFET structure is similar to that of the enhancement-type. The depletion-type MOSFET has a built-in channel as a difference. Therefore, if the drain terminal is positively charged with respect to the source terminal, the current flows through between source and drain, even if a positive voltage is not applied to the gate terminal. However, the channel depth (or conductivity) can be altered by the applied voltage to the gate terminal. Increasing the gate voltage leads to an increase in the channel depth and thus results in an increase in current flow. On the other hand, applying a negative voltage to the gate terminal cause to decrease the conductivity of the channel. Consequentially, voltage fluctuations on the gate terminal lead to fluctuations in the current flowing through the source and drain terminal.

7.2.2. Microfabrication of the MOSFET

The structural design and fabrication of the n-channel depletion type MOSFET in the proposed electrode was simulated in the Silvaco electronic design automation and technology computer-aided design program (İstanbullu & Avci, 2019). The simulation of the transistor is done in a two-dimensional numerical semiconductor processing simulator. The flow chart of microfabrication process is shown in Figure 7.4 and methodology is given below.

The physical structures of the each process is shown on the left-hand side, whereas the color counter of the structure, indicating the doping concentrations, is shown on the right-hand side. Process names are given in the titles of each figure.

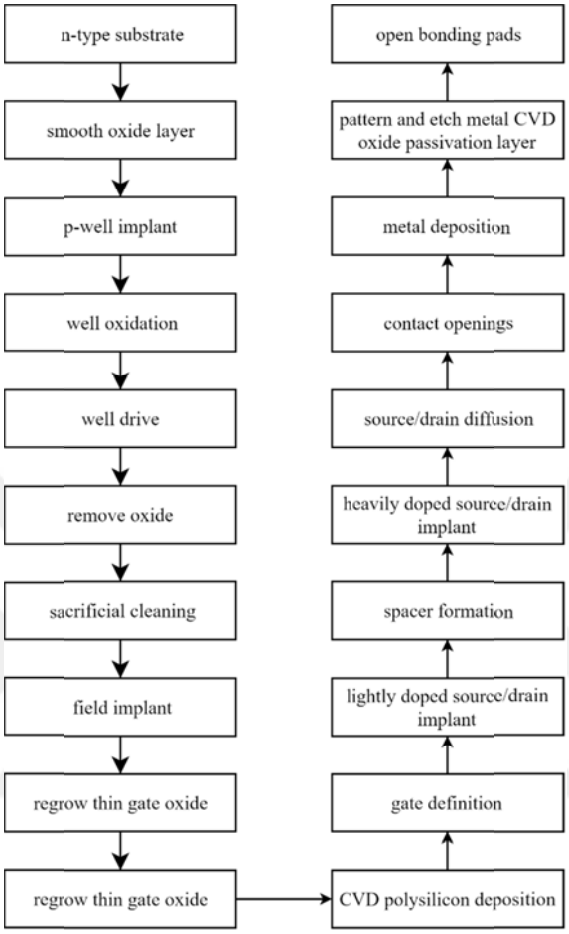

Figure 7.4 Flow chart of n-type depletion mode MOSFET microfabrication

Silicon (Si) wafer in the <100> orientation was selected as a substrate material of n-channel depletion type MOSFET development. The wafer was doped with phosphorus at a concentration of $1x10^{14}$ cm^{-2} for background doping. The screening oxide was created through the diffusion process at 1000°C and 1 atm for 30 min with dry oxide, as shown in Figure 7.5.

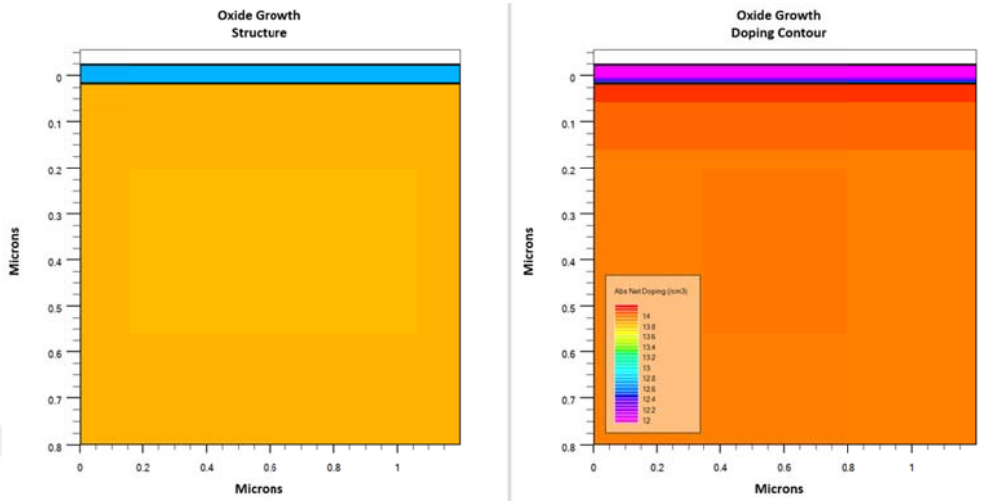

Figure 7.5 MOSFET structure and doping concentration after oxide growth

The p-well was formed using boron implantation with an energy of 100 keV and a dose of $8x10^{12}$ cm^{-2}. The implantation was modeled using the Pearson model. The physical structure and doping concentration of p-well substrate after the implantation step is shown in Figure 7.6.

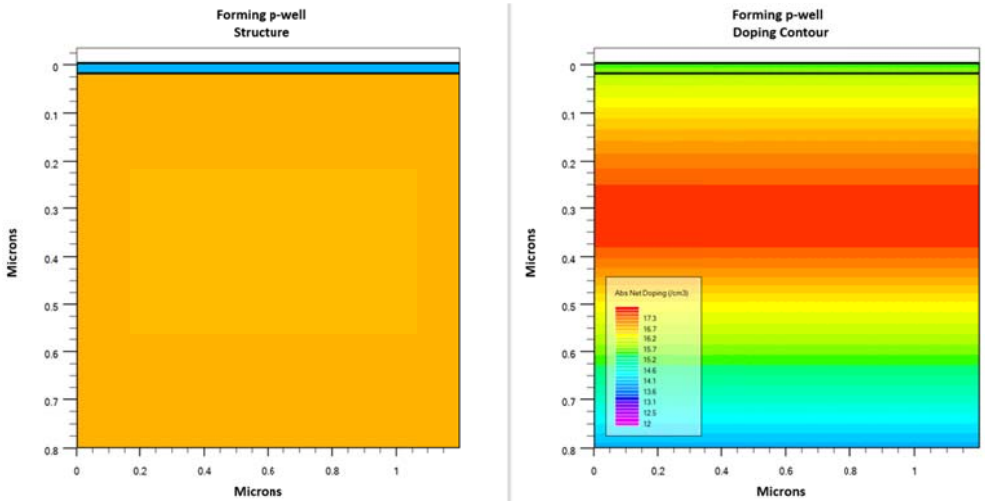

Figure 7.6 MOSFET structure and doping concentration after p-well implantation

The next step was well oxidation, and it was developed through the diffusion process at 950°C and 3 atm for 100 min with wet oxide. The simulation result of this process is shown in Figure 7.7.

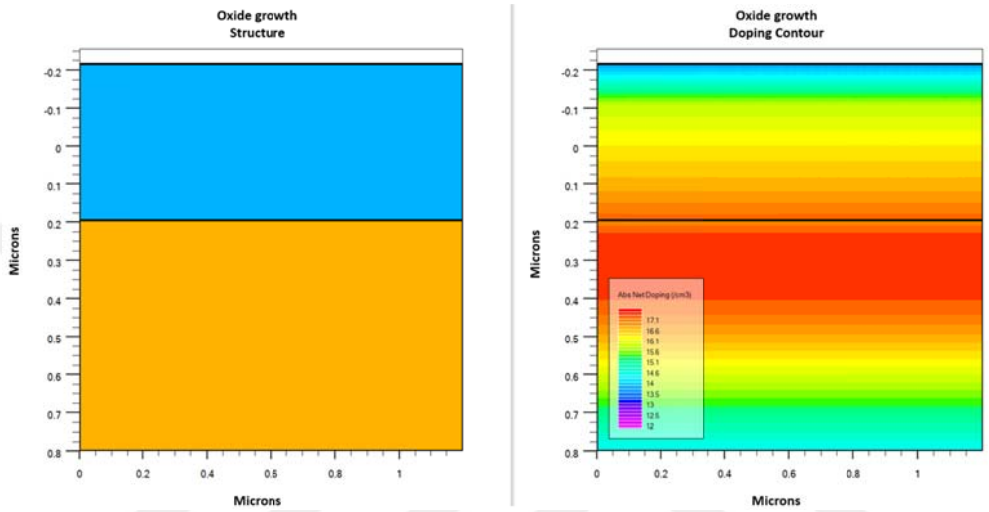

Figure 7.7 MOSFET structure and doping concentration after well oxidation

The well drive-in step was performed with varying durations (50–220–90 min), varying temperatures (1000, 1200°C), temperature change rates (4, –4.4), and processing environments (dry oxide, nitrogen). After the well drive step completed, the more uniform doping concentration along the depth was found as in Figure 7.8.

The grown oxide was etched from the wafer to form the substrate surface ready for defining MOSFET features. Sacrificial cleaning requires oxidation, followed by the removal of the grown oxide. The oxygen in the oxidation step reacts with the surface silicon forming the silicon dioxide before it is etched away. This oxidation process was performed by diffusion at 1000°C, and 1 atm for 20 min with 3 percent hydrochloric acid mixed dry oxide.

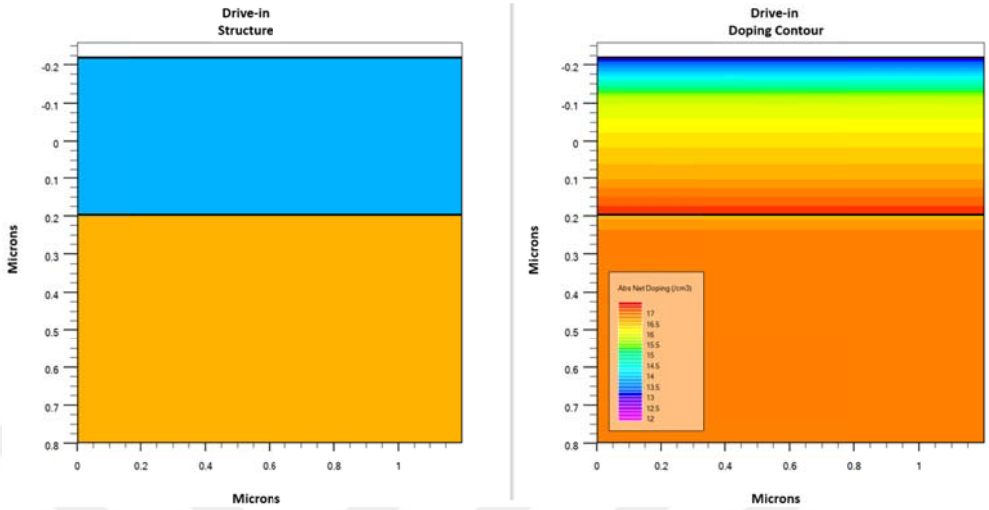

Figure 7.8 MOSFET structure and doping concentration after well drive

As a result, a thin substrate layer is also removed as shown in Figure 7.9.

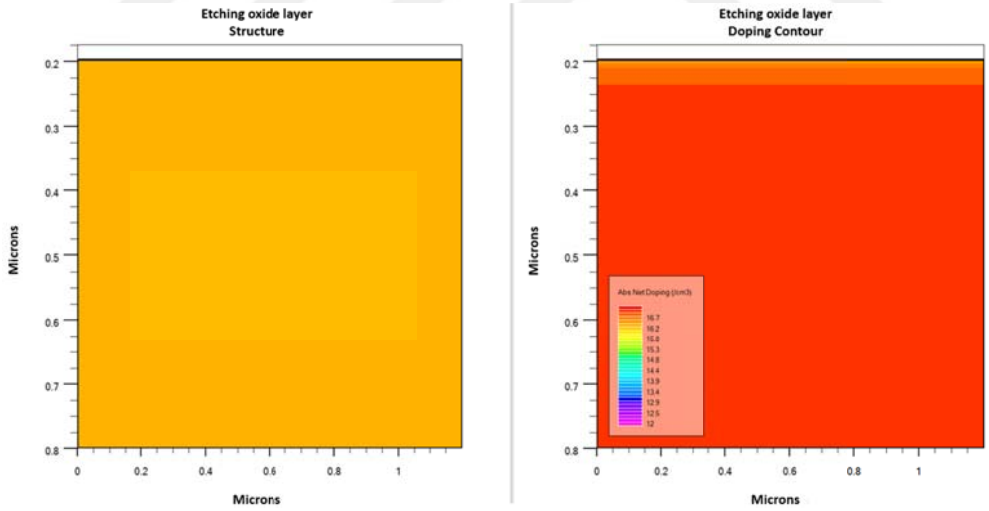

Figure 7.9 MOSFET structure and doping concentration after oxide removal

The field implant to form light doped drain (LDD) was realized by implanting phosphorus with an energy of 20 keV and a dose of $3x10^{13}$ cm^{-2}. The

implantation was modeled using the dual Pearson model. Doping concentration after the LDD process is shown in Figure 7.10.

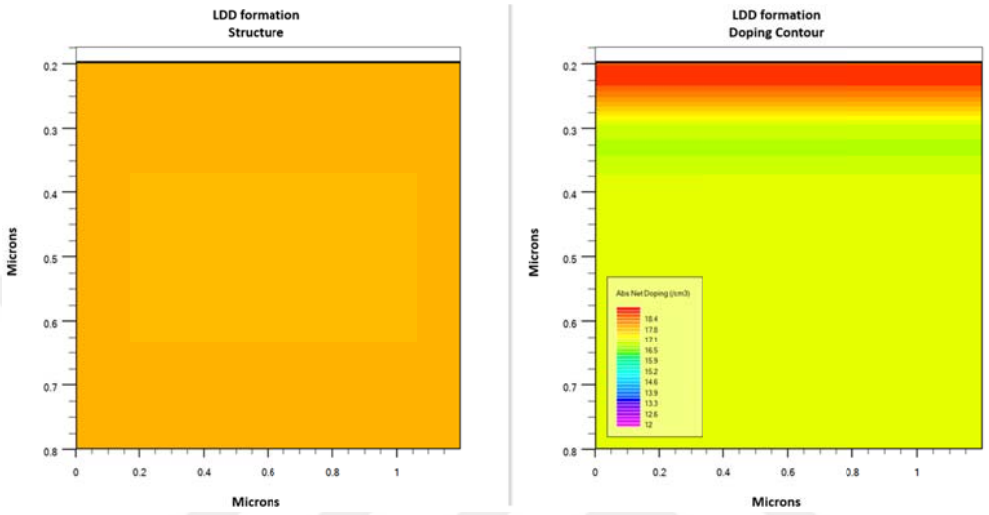

Figure 7.10 MOSFET structure and doping concentration after LDD formation

The gate oxide was grown on the wafer by deposition at 700°C, and 1 atm oxidation pressure for 1 min with 3 percent hydrochloric acid mixed dry oxide. The thickness of the oxide layer can be altered by changing the time, temperature or type of the oxidation. The thickness of the gate oxide, shown as a blue layer on the substrate structure in Figure 7.11, has an important role on MOSFET characteristics.

Next, in order to adjust the threshold voltage of the n-channel depletion type MOSFET device, boron atoms of 10 keV energy and a dose of 9.5×10^{11} cm^{-2} were implanted. This is a similar process to the implantation step to form p-well substrate as shown previously in Figure 7.6. A higher dose of the implanted boron atoms leads to increase in threshold of the MOSFET.

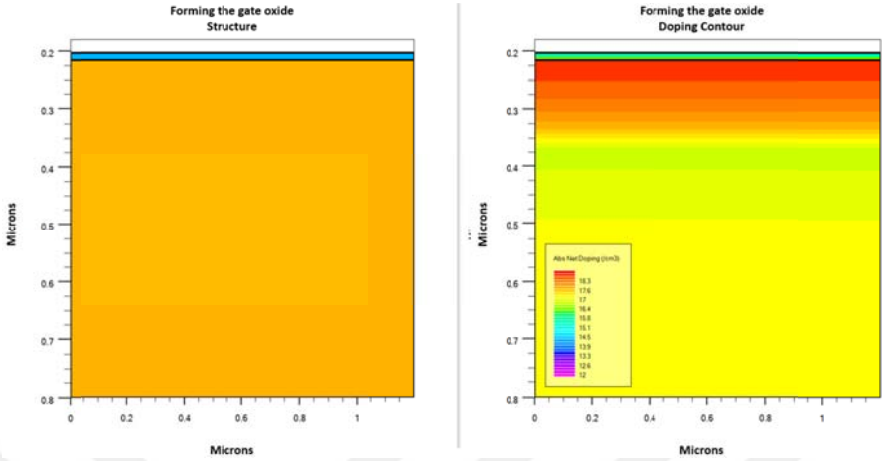

Figure 7.11 MOSFET structure and doping concentration after gate oxide deposition

The next step in the microfabrication is the polysilicon deposition to create the gate terminal of the MOSFET. It is similar step to previously explained oxide deposition. The polysilicon gate layer was deposited with a thickness of 0.3 µm on the gate oxide layer, and then a specified region polysilicon layer was etched. The two dimensional structure of the polysilicon gate is shown in Figure 7.12.

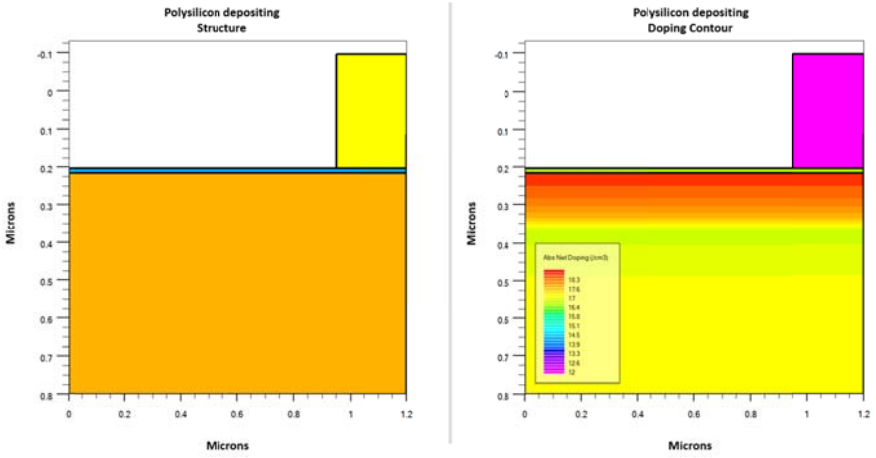

Figure 7.12 MOSFET structure and doping concentration after polysilicon deposition

In the next step, phosphor atoms with 20 keV, and a dose of $3x10^{3}$ cm^{-2} was implanted through the deposited oxide layer to form lightly doped drain/source junction. The light drain or source region is shown in Figure 7.13.

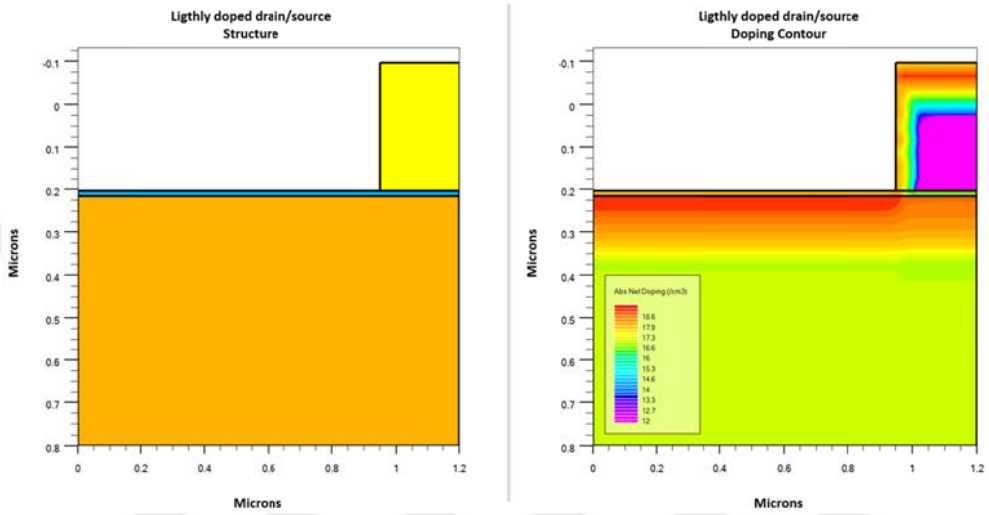

Figure 7.13 MOSFET structure and doping concentration after LDD process

An oxide spacer is formed as a barrier, and then etched anisotropically. Approximately 0.35 μm oxide was deposited using low-pressure chemical vapor deposition to generate oxide spacers at the polysilicon edges as shown in Figure 7.14.

The heavy source/drain implantation, similar to the LDD process, is performed to form source and drain regions in the wafer. Doping concentration of heavy implantation is several orders of magnitude greater than light drain/source implantation concentration. Implanted atoms of this process are arsenic instead of phosphorus. The source and drain formation were done by implanting arsenic with an energy of 50 keV and a dose of $3x10^{15}$ cm^{-2}. It is necessary to diffuse implanted atoms deep into the wafer. In this case, the thermal annealing was done to electrically activate and diffuse implanted ions at 1000°C and 1 atm for 1 min with nitrogen.

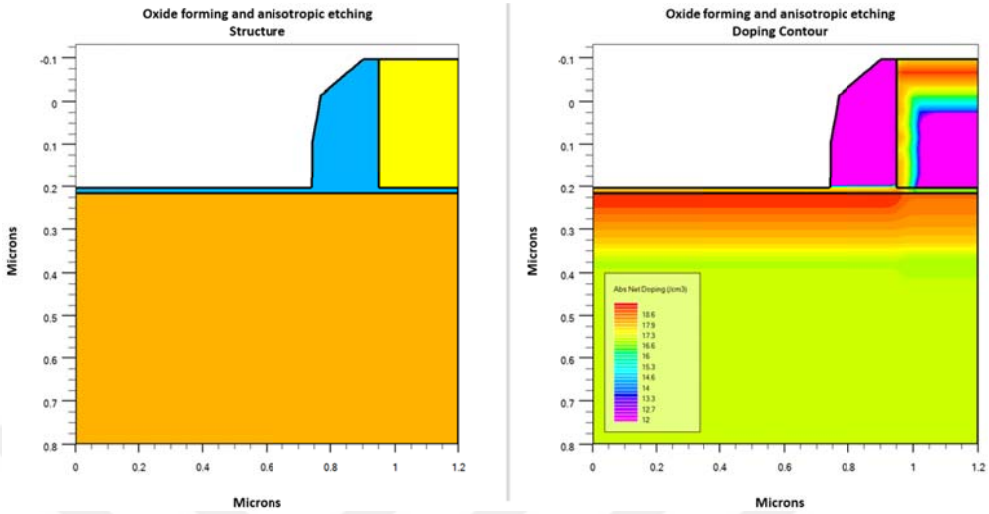

Figure 7.14 MOSFET structure and doping concentration after oxide spacer step

This diffusion process was modeled by the Fermi compression method and the process is done in an inert environment to prevent undesirable reactions. The formation of the source/drain region is shown in Figure 7.15.

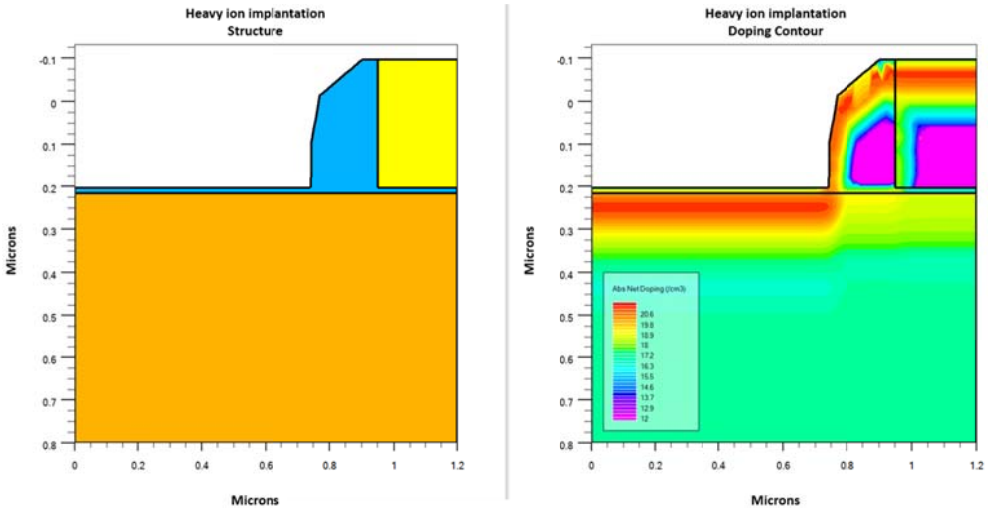

Figure 7.15 MOSFET structure and doping concentration after heavy ion implantation

In this step, etching of the oxide layer on the source/drain region is required to make wafer surface suitable for metal contacts, as shown in Figure 7.16.

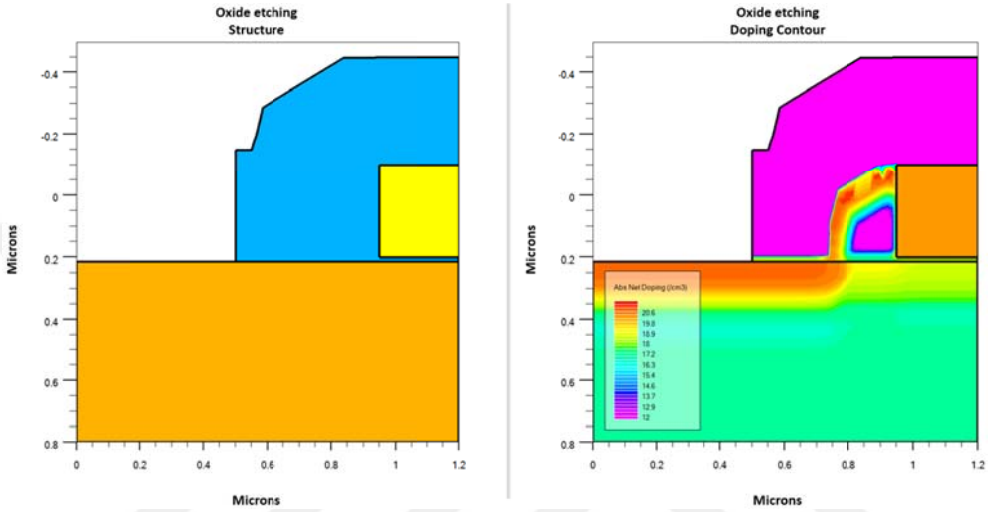

Figure 7.16 MOSFET structure and doping concentration after oxide etching

After the process of the contact opening, the metallization step is performed. To create metal contact electrodes, a metal (aluminum) with low resistance is deposited over the entire structure by sputtering technique. Then, some specific regions of deposited metal are etched away from the surface geometrically to develop terminals of the MOSFET. Figure 7.17 shows the structure of device after the metallization process.

Up to this point, all processes of the n-type depletion mode MOSFET microfacrication are developed for only half of the device. Since the MOSFET is a symmetrical device, the complete device layout can be obtained by mirroring. The mirroring defines all the above-mentioned steps for the right half of the device as same as for the left half of the device. The complete microfabricated MOSFET device is shown in Figure 7.18. The final step is defining the regions of MOSFET

as the gate, source and drain teminals. After the terminals are defined, the device is ready for simulation to obtain electrical characteristics.

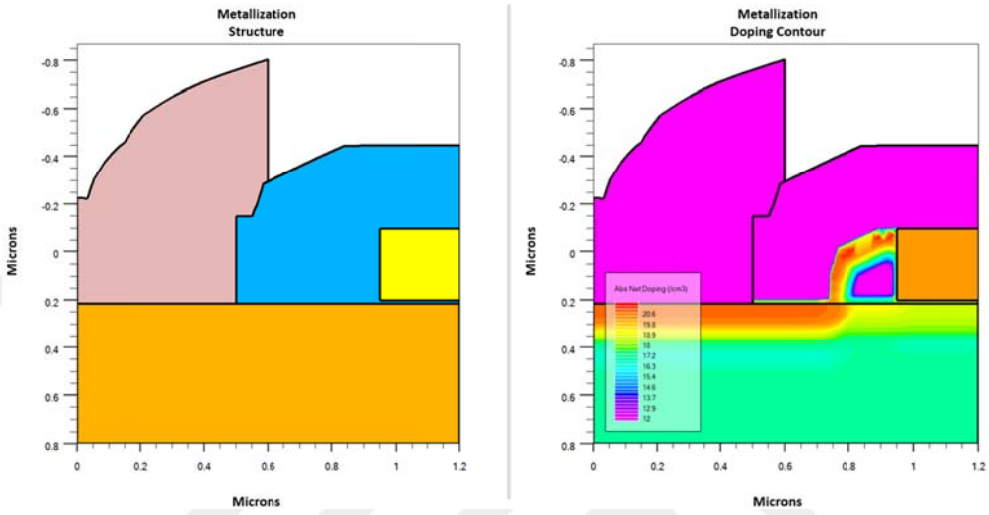

Figure 7.17 MOSFET structure and doping concentration after the metallization

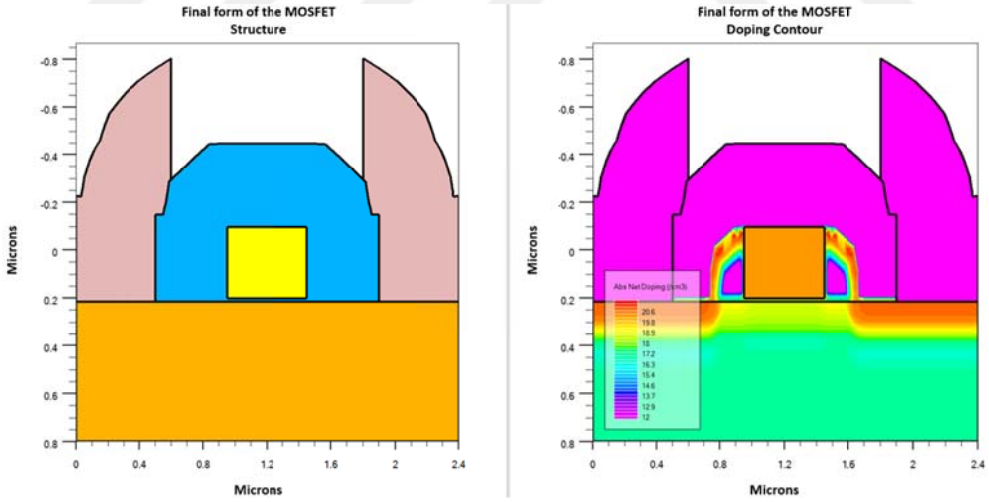

Figure 7.18 Final MOSFET structure and doping concentration

The characteristic current-voltage $(I-V)$ curve of the designed transistor is given in the Figure 7.19.(a) for high gate voltages (V_G from –3 V to 3 V) with the various drain to source voltages $V_{DS}=1, 1.5, 2, 2.5,$ and $3\,V$. Furthermore, Figure 7.19.(b), the characteristic $(I-V)$ curve of the device for the gate voltages in the biopotential voltage range, is almost linear. These characteristic curves show the suitability of the microfabricated MOSFET in this range of biopotentials.

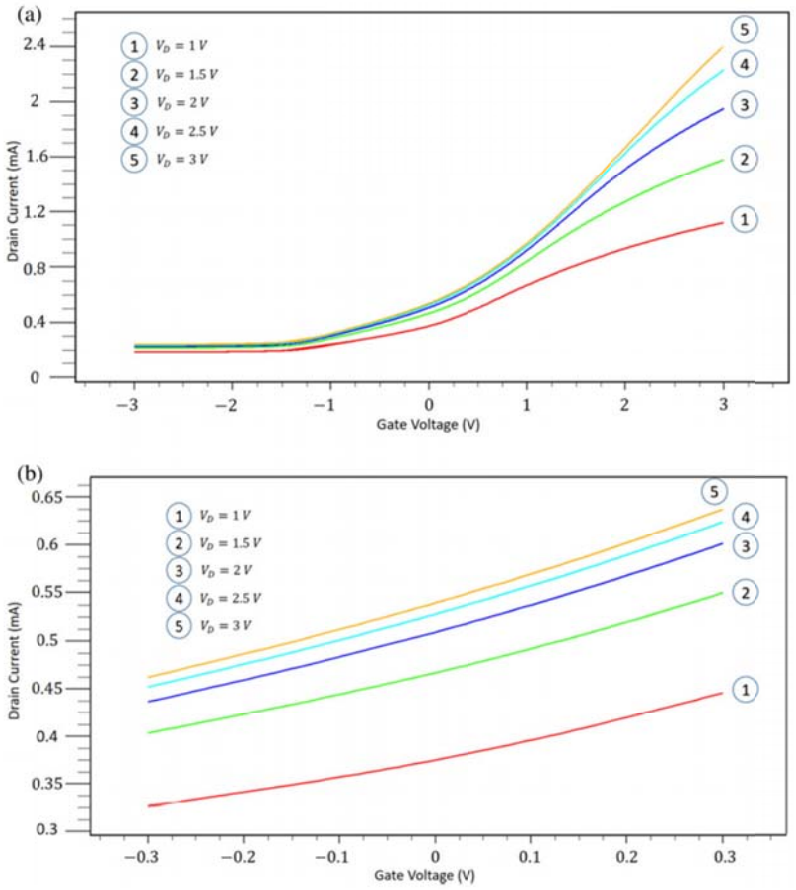

Figure 7.19 (a) Drain current (I_D) versus gate voltage (V_G) plot of the MOSFET in $[-3V, 3V]$ range for different drain voltages (V_D). (b) (I_D-V_G) plot of MOSFET in the $[-0.3V, 0.3V]$ range.

7.3.CNT Integrated Active Electrode

When a metal electrode is contacted to a non-prepared skin surface for electrophysiological measurements, a high electrode–skin impedance occurs. This condition is due to the unformed direct electrode-electrolyte electrochemical interface with the body fluid.

The measurement surface must be prepared before recording to achieve low electrode–skin impedance. It is necessary to use the electrolytic gel or abrade the dead stratum corneum layer on top of the skin. The goal of skin abrasion is to reduce the thickness of the stratum corneum layer causing high impedance. The process of completely removing the stratum corneum layer is painful and unhealthy; thus, this task is not recommended. Alternatively, the electrolytic gel containing conductive ions at high concentrations can be applied to the stratum corneum. The electrolytic gel passes into the stratum corneum by diffusion and increases the conductivity. However, in long-term measurements, the gel dries out after a few hours, and various noises, resulting from the unstable gel-skin interface, occurs on the signal. The stratum corneum layer must either be removed or bypassed to overcome the mentioned measurement stability problems.

The electrode designed in this work abolishes the use of the gel and abrasion process of stratum corneum. The electrode contains needle-like carbon nanotube arrays grown vertically aligned at the gate of an n-channel depletion type MOSFET. The vertically aligned MWCNTs penetrate the stratum corneum layer, which causes the noise; thus, bypass of stratum corneum eliminates the noises on the biopotential signal acquisition. The carbon nanotube array penetrated to the skin also provides a stable contact to the skin by increasing the surface area. Thereby this supplies a low electrode–skin interface impedance advantage for the electrode. Since the electrode is attached more firmly to the skin surface, it prevents artifacts caused by breathing or limb movements. In the electrode model given in Figure 7.20, carbon nanotubes pass over the stratum corneum layer, which is composed of dead cells.

Since each carbon nanotube in an array is not sufficiently long to reach the nerve cells or living cells, pain and infection risk does not exist. This approach has fewer penetrations into the skin surface than needle electrode models that work on similar principles.

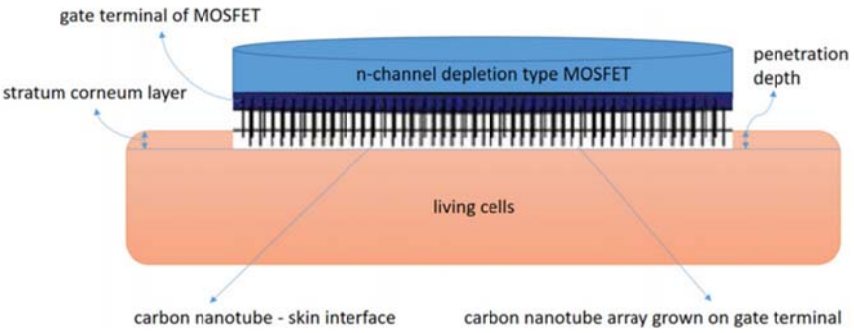

Figure 7.20 Two-dimensional view of the complete proposed electrode on the skin.

In the proposed electrode model, since the stratum corneum layer is bypassed by employing carbon nanotubes, the use of the gel is no longer required. Therefore, undesirable effects such as the electrolytic gel resistance (R_s), gel–stratum corneum interface potential (E_{se}), and stratum corneum impedance effect $(R_p - C_p)$ on measuring biopotentials are eliminated, and the equivalent circuit of Figure 3.2 is reduced to a much simpler form as shown in Figure 7.21.

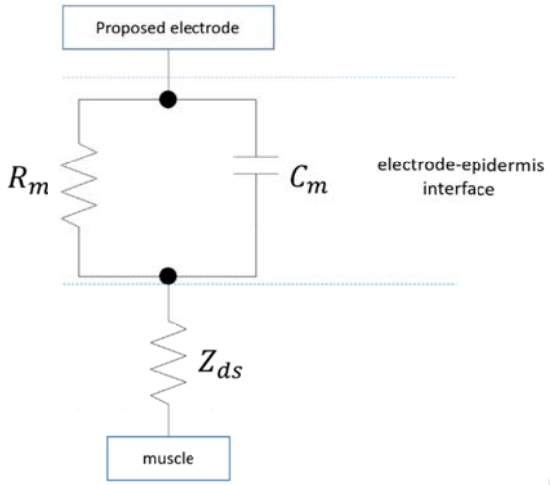

Figure 7.21 Electrical equivalent circuit of the proposed electrode-skin interface

The proposed electrode model and wet electrode model comparison can be made according to the electrical equivalent circuits in the simulation environment. By considering the wet electrode equivalent circuit shown in Figure 3.2, the equivalent impedance can be written as Equation 7.20.

$$Z_{wet} = Z_{ds} + \frac{R_e}{\sqrt{1+(wR_eC_e)}} + R_s + \frac{R_d}{\sqrt{1+(wR_dC_d)}} \tag{7.20}$$

where Z_{ds} indicates the combination of the living dermis and subcutaneous tissue while Rs specifies the resistance of electrolytic gel. $R_e - C_e$ and $R_d - C_d$ pairs depend on the electrolytic gel, as shown in Figure 3.2. In long-term measurements, the gel dries out. Additionally, other factors, such as perspiration, may change the electrical properties of the electrolytic gel. Deteriorations on the gel affect the contact impedance. The electrode–skin contact impedance dependence of certain noises has been surveyed in the literature (Huigen et al., 2002), (Assambo et al., 2007), (Kaczmarek & Webster, 1989), (Toazza et al., 1998). The signal quality is

unstable when the wet electrode is used for long-duration measurements since certain parts of noise depend on impedance. Instead of this design, in the proposed electrode, since the electrode is directly in contact with the living cells without conductive gel, parameters retain certain values for the long term. Thus, the electrode designed in this study guarantees a more stable signal quality without time dependence.

As shown in Figure 7.20, the gate terminal of the n-channel depletion type MOSFET is covered with vertically aligned carbon nanotube arrays. Due to the depletion-type transistor characteristics, the channel between the drain and source is conducting, and current flow even though there is no voltage at the gate terminal. When the proposed electrode is attached to the skin surface, the carbon nanotubes at the gate terminal sense the biopotential signal. Oscillations of electrophysiological signals sensed by carbon nanotubes appear on the current flowing through the drain to source. AC equivalent of the proposed electrode model is shown in Figure 7.22.

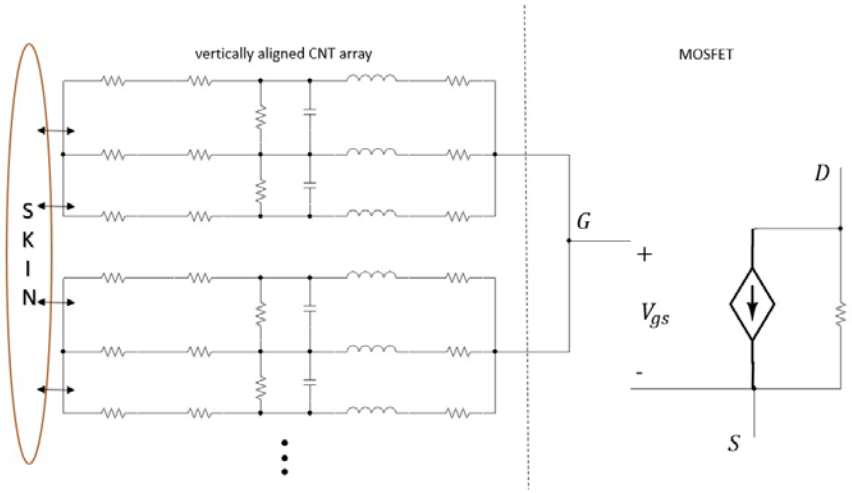

Figure 7.22 AC equivalent circuit of the proposed electrode model

The drain and source terminals of the transistors in the proposed electrode model are electrically connected, as shown in Figure 7.23. Thereby biopotential signals from different regions of the skin surface are accumulated. The measured signals on the gate terminal control the drain current. At low frequencies (~1–5 Hz), the gate terminal of MOSFET exhibits an impedance that is too high to affect the measured biopotential signal. Additionally, the n-channel depletion-type MOSFET provides direct charge–current conversion, high dielectric insulation with skin, and low-noise pre-amplification of electrophysiological signals.

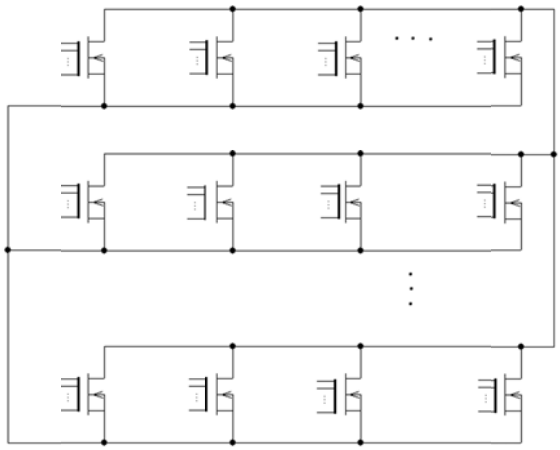

Figure 7.23 Circuit diagram of the proposed electrode that consisted MOSFETs

8. SIMULATION RESULTS

In this section, simulations of the proposed electrode circuit equivalent and the commonly used wet electrode circuit model are compared. Two cases of skin condition are taken into consideration for comparison. They are prepared and unprepared skin cases. The range of the typical numerical values of skin, gel, and electrode parameters are taken from the study of Liu et al (Liu et al., 2004).

In this work, electrocardiogram, electromyogram and electroencephalogram signals, selected randomly from the Massachusetts Institute of Technology Beth Israel Hospital database, are used as the inputs as shown in Figure 8.1 (a), Figure 8.1 (b) and Figure 8.1 (c), respectively. Fourier transforms of the input signals are also given in Figure 8.2 (a), (b) and (c).

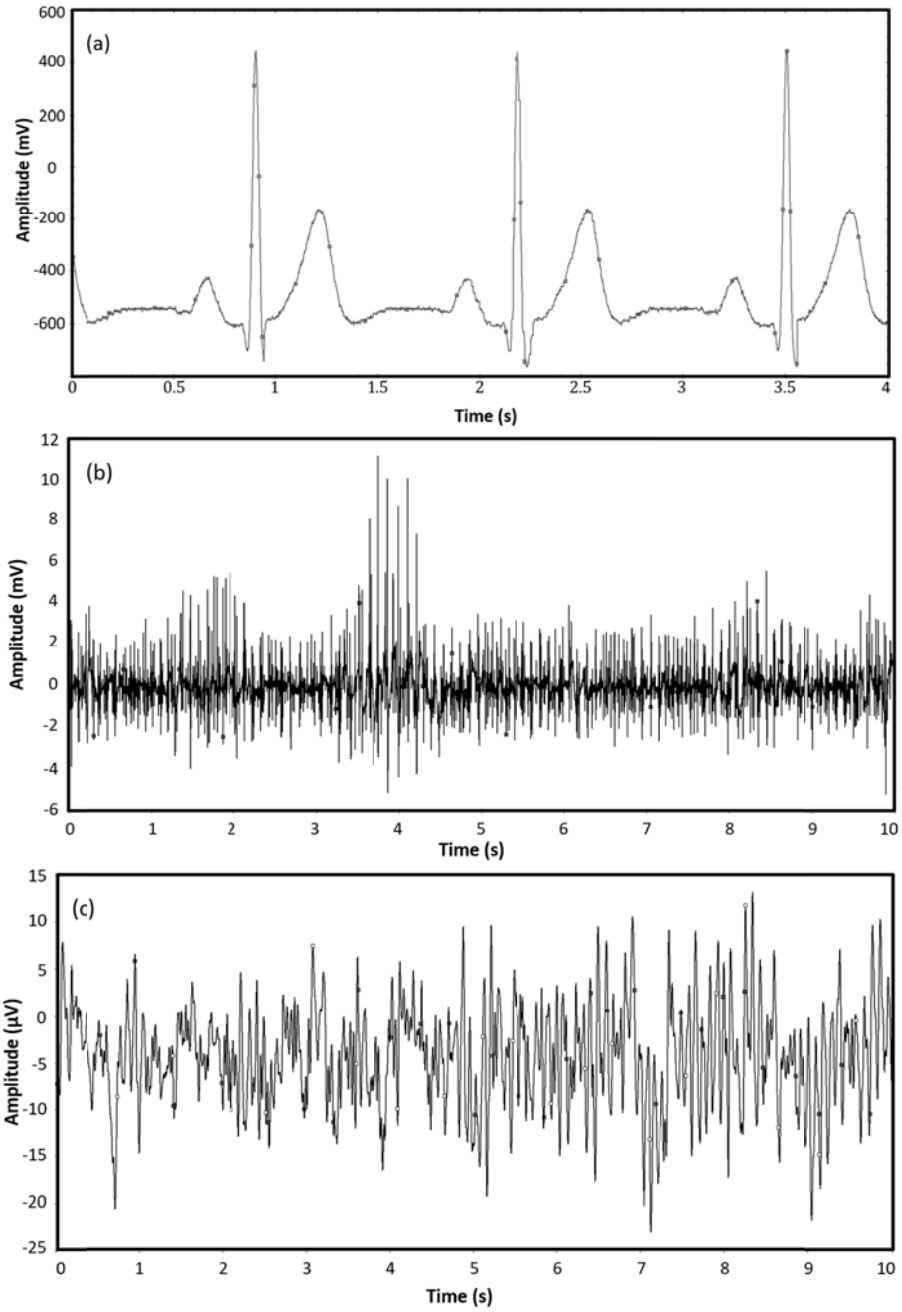

Figure 8.1 Input signals of the proposed electrodes: a) ECG, b) EMG, c) EEG

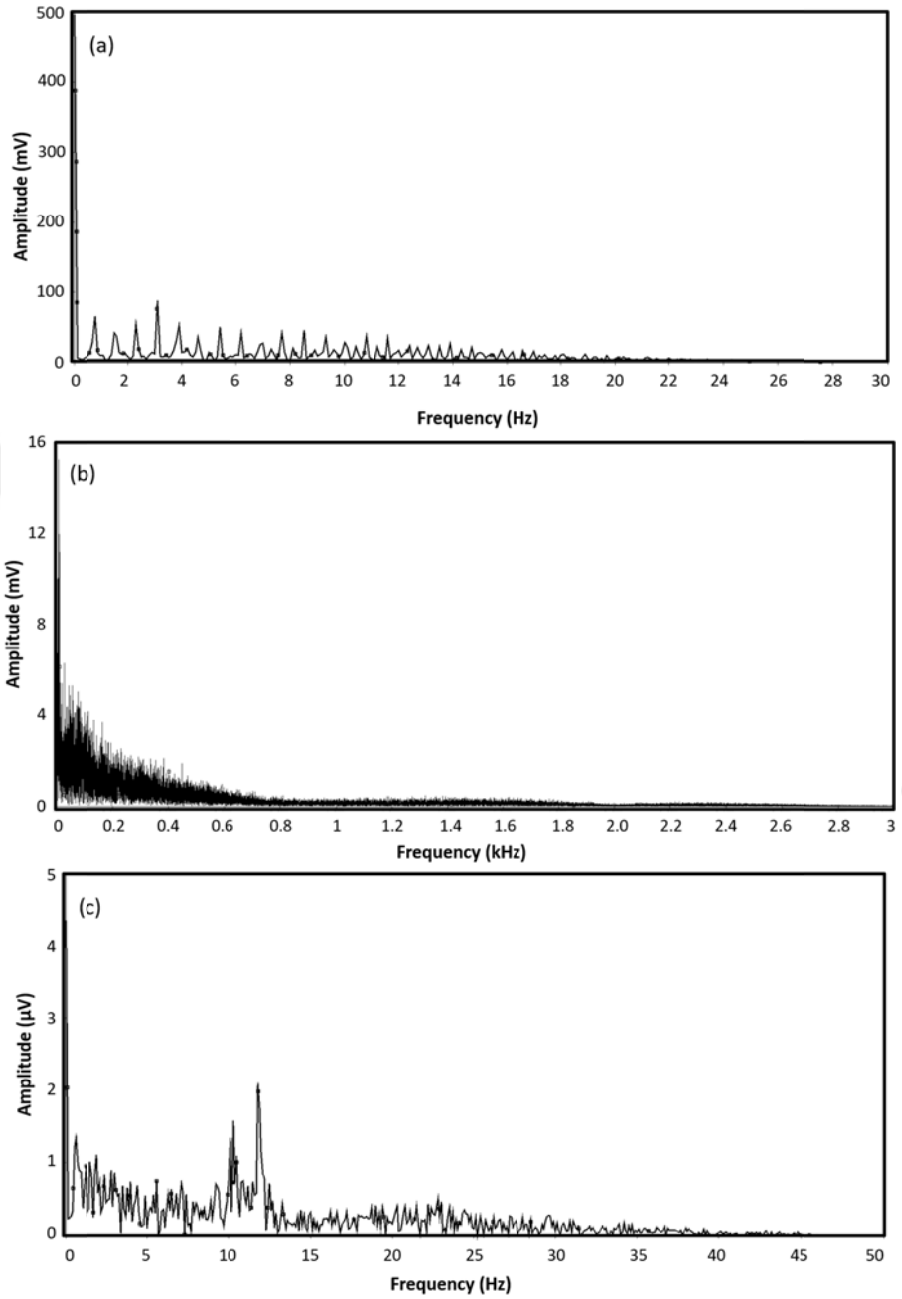

Figure 8.2 Fourier transforms of the input signals: a) ECG, b) EMG, c) EEG

The stratum corneum layer parameters in the circuit equivalent shown in Figure 3.2 are swept from the numerical values of prepared skin $\left(R_p = 10\ k\Omega / C_p = 10\ nF\right)$ to the unprepared skin $\left(R_p = 1\ M\Omega / C_p = 40\ nF\right)$. The effect of stratum corneum layer parameters on the peak value of the captured signal is shown in Figure 8.3. Obviously, an increase in the thickness of the stratum corneum layer increases the contact impedance. Additionally, an increase in the resistance of stratum corneum causes attenuation dramatically on the amplitude of the captured signal, as shown in Figure 8.3.

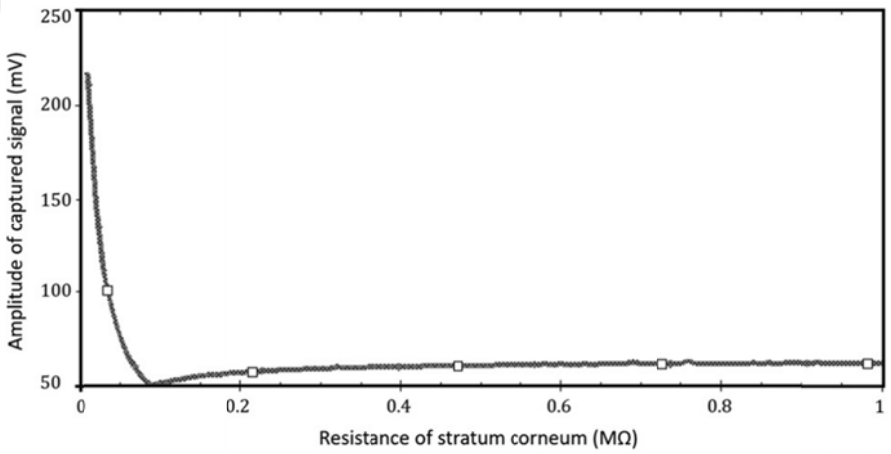

Figure 8.3 Change of the captured electrocardiogram signal amplitude depending on the stratum corneum layer resistance.

In this case, circuit equivalent model responses of the proposed electrode on unprepared skin, wet electrode on prepared skin with gel and wet electrode on unprepared skin with gel are simulated. Figure 8.4 shows the simulation results of the three electrode models to the 2 Hz, 100 mV sinusoidal wave. Signal amplitude obtained from the proposed electrode model maintains the 93.27% of the input signal, whereas the signal amplitudes taken from wet electrodes on prepared and

unprepared skin surfaces retain their input amplitudes 48.26% and 0.99%, respectively.

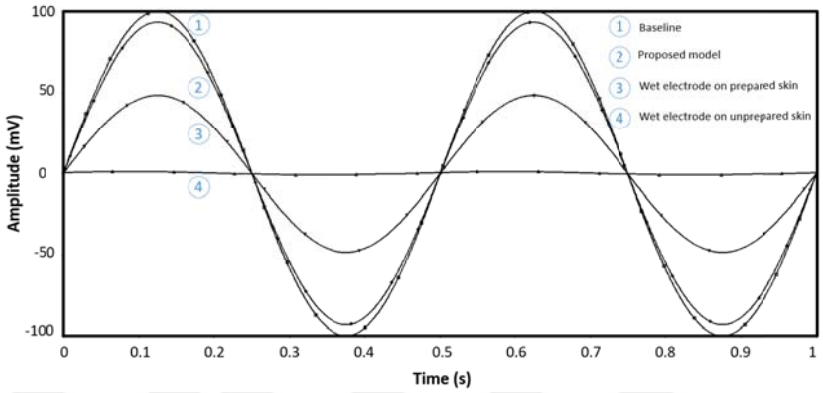

Figure 8.4 Responses of electrode circuit equivalents to the sinusoidal signal

Figure 8.5 shows the captured signal waveforms of the proposed electrode and wet electrode models for ECG signal in two cases. The simulation results, shown in Figure 8.5, are labelled 1 to 4 as the baseline, the proposed electrode on unprepared skin, wet electrode on prepared skin, and wet electrode on unprepared skin, respectively. Figure 8.5.(3) is the first case where the skin is well prepared, and the electrolytic gel is applied. The results show that the amplitude of the input signal is reduced to approximately half of the baseline. In the second case, the skin is not cleaned from hairs and stratum corneum layer, the signal quality is quite distorted, and the amplitude of the signal is reduced one-sixth of the baseline, as shown in Figure 8.5.(4) (Istanbullu & Avci, 2019).

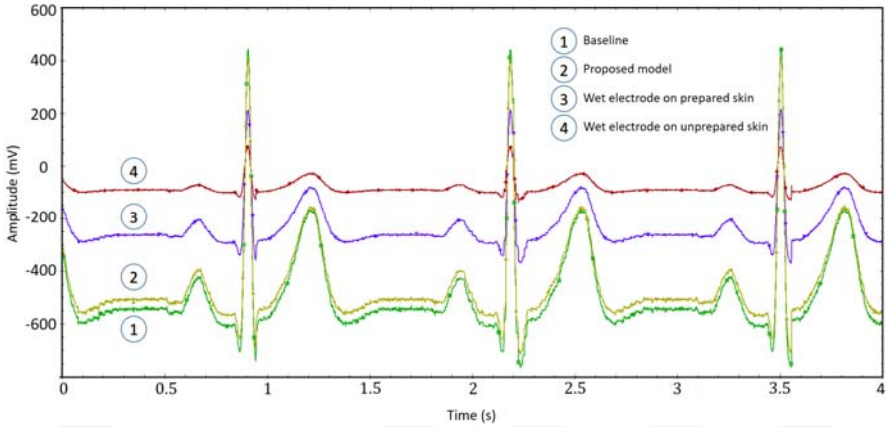

Figure 8.5. Simulation results of the standard wet and proposed electrode model for electrocardiogram signal input.

Data acquired from the standard wet electrode model for the second case show a very high half-cell potential (~480 mV), where half-cell potential of case-1 (~290 mV) is lower than that in the second measurement set. The amplitude of the signal captured by the proposed electrode is attenuated slightly and maintains the baseline amplitude at approximately 93%. Additionally, the half-cell potential of the proposed electrode model is considerably small (~30 mV) and lower than in the first and second cases.

Similarly, EMG and EEG signals, given in Figure 8.1 (b) and (c), also applied to the circuit equivalents of the three electrodes. The EMG signal is taken from a healthy person with a 4000 Hz sampling frequency, whereas the EEG signal is obtained by the 10-20 electrode system with 500 Hz sampling frequency. The EEG signal, given in the Figure 8.1 (c), is the pre-frontal (Fp1) recording. Both signal durations of EMG and EEG are 10 seconds. Signal responses of the proposed electrode, as well as wet electrodes in two cases, to the EMG and EEG inputs, are shown in Figure 8.6 and Figure 8.7, respectively.

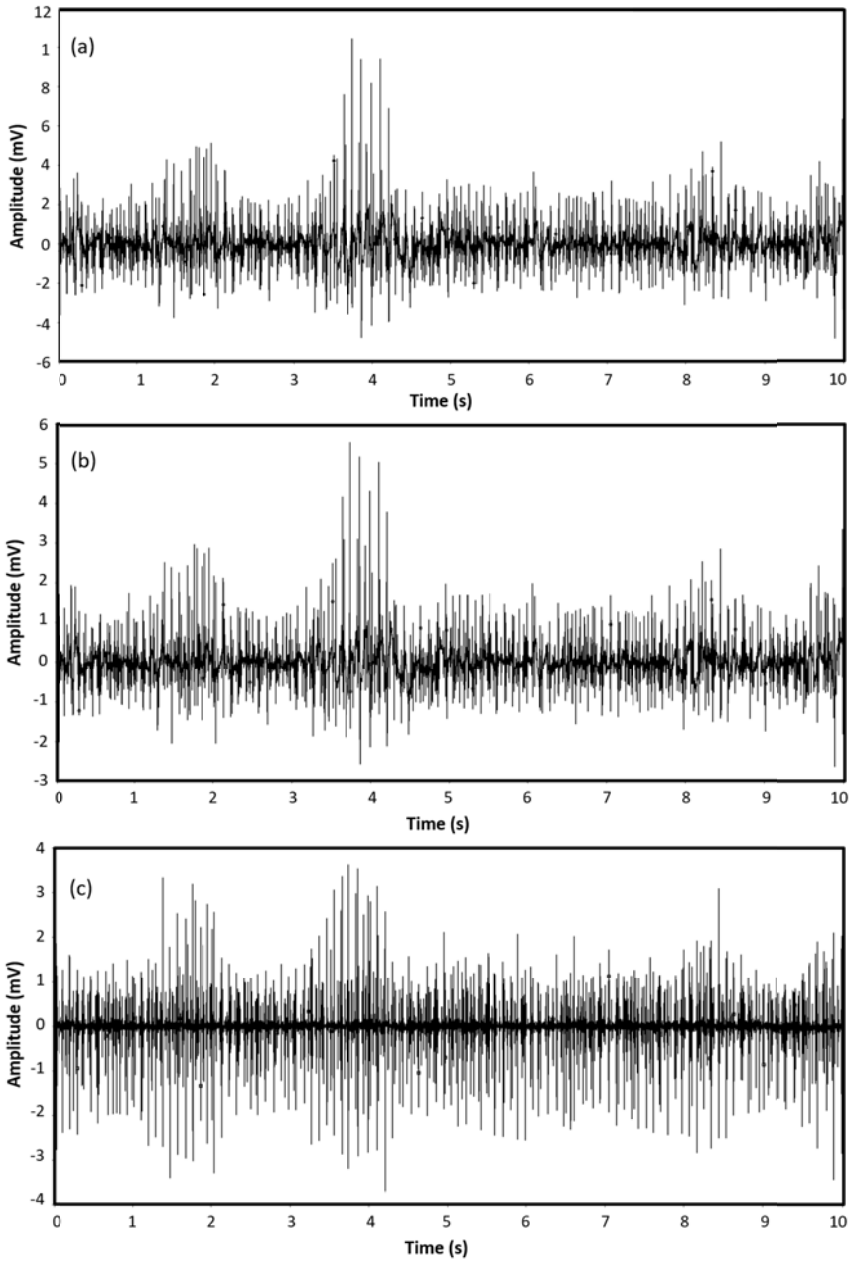

Figure 8.6 Simulation results to the EMG signal. (a) Proposed electrode , (b) Wet electrode on prepared skin (c) Wet electrode on unprepared skin.

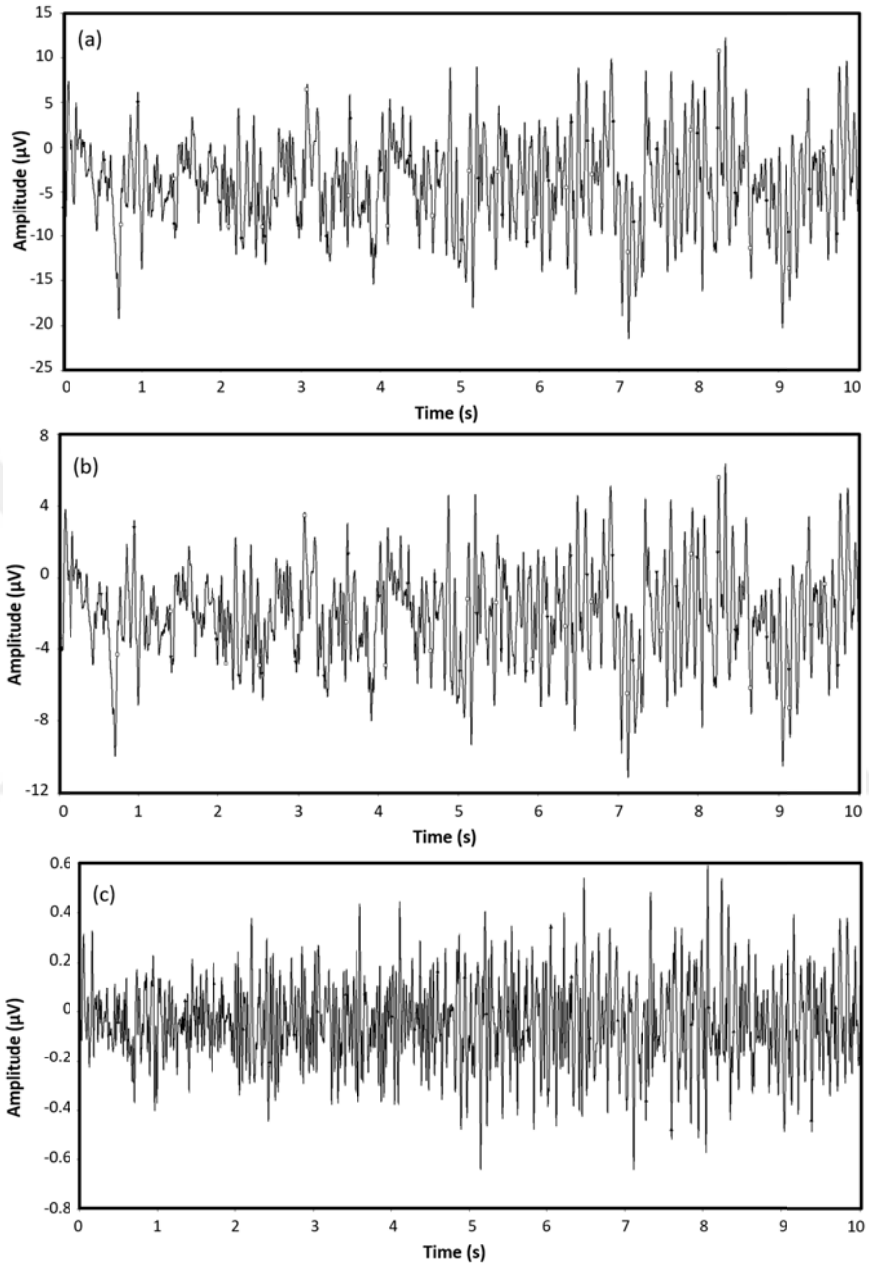

Figure 8.7 Simulation results to the EEG signal. (a) Proposed electrode , (b) Wet electrode on prepared skin (c) Wet electrode on unprepared skin.

In Fıgure 8.6 (a), the EMG signal obtained from the proposed electrode remains the amplitude of the input signal, whereas the amplitude of the signal, taken from the wet electrode on the prepared skin surface with the presence of conductive gel, is decreased approximately 60% as given in Figure 8.6 (b). Moreover, the signal acquired from the wet electrode on the unprepared skin is reduced considerably, as shown in Figure 8.6 (c).

Similarly, when the EEG signal is applied to the three electrodes, comparable results are obtained with that of ECG and EMG inputs. The signal output from the proposed electrode almost does not show voltage drop in contrast with the wet electrodes, as given in Figure 8.7 (a). The simulation results show the proposed electrode has much lower contact impedance and very high-quality signal acquisition advantages. Although skin preparation and/or gel application are performed in the both wet electrode acquisitions, the electrophysiological signal qualities are much less than that of the proposed electrode, as shown in Figure 8.7 (b) and (c).

The Fourier transforms of obtained biopotential signals prove the abovementioned considerations. Figures 8.8, 8.9 and 8.10 show the Fourier transforms of the simulation outputs for ECG, EMG and EEG signal inputs. The figures annotated with (a) show the Fourier transforms for the proposed electrode model, whereas (b) and (c) give the Fourier transforms for the wet electrode on prepared skin and the wet electrode on the unprepared skin, respectively. Figures 8.8 (a), 8.9 (a) and 8.10 (a) exhibit almost the same Fourier transform with respect to that of original signals given in Figure 8.2 (a), (b) and (c). Fourier transforms for wet electrode at the case-2 show considerable decrement on the amplitude of principal frequency components as given in Figure 8.8 (b), 8.9 (b) and 8.10 (b). It is obvious from the Fourier transforms for the wet electrode at case-1, the signal amplitude is extremely reduced. Additionally, amplitudes of noise components are increased considerably, as shown in Figure 8.8 (c), 8.9 (c) and 8.10 (c).

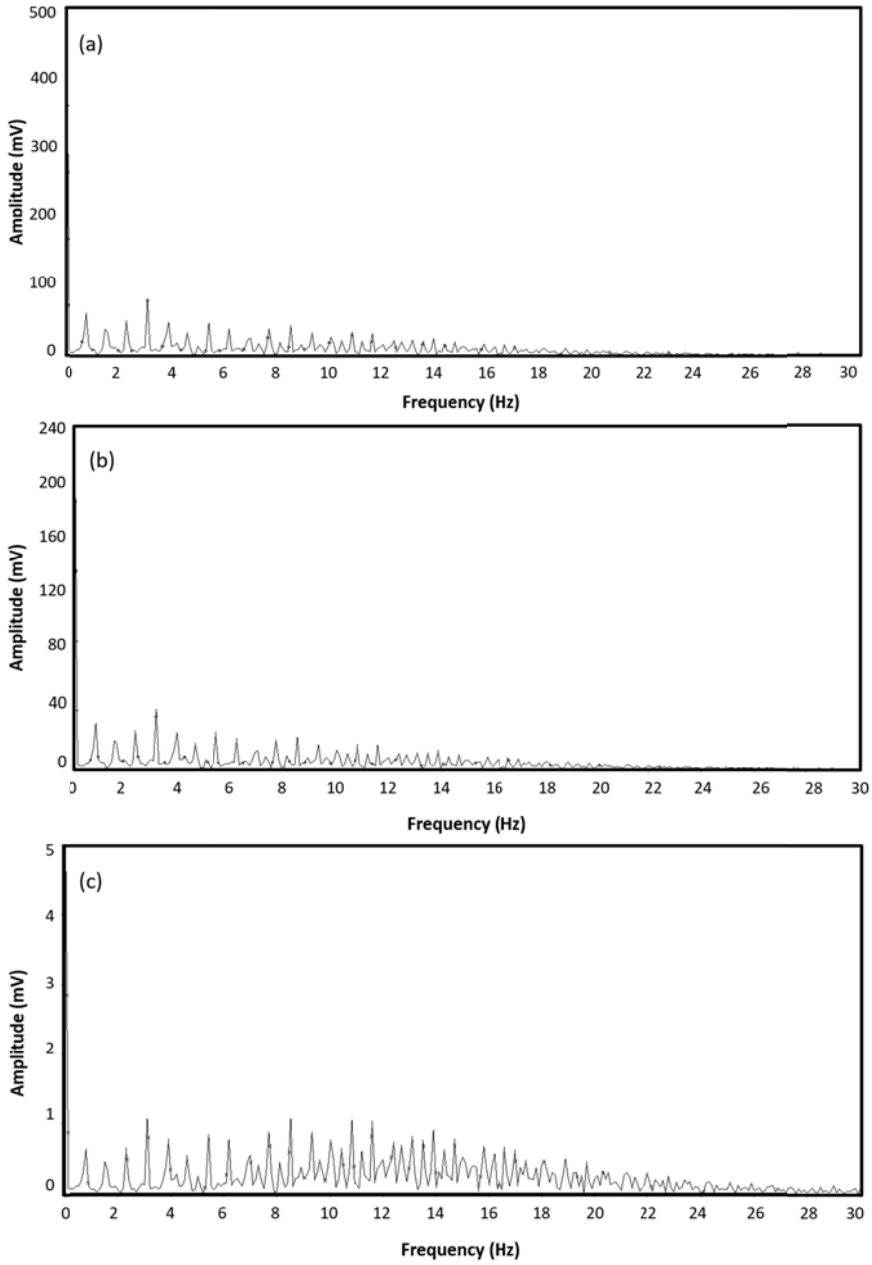

Figure 8.8. Fourier transforms of the ECG signal output for (a) Proposed electrode, (b) Wet electrode on prepared skin (c) Wet electrode on unprepared skin.

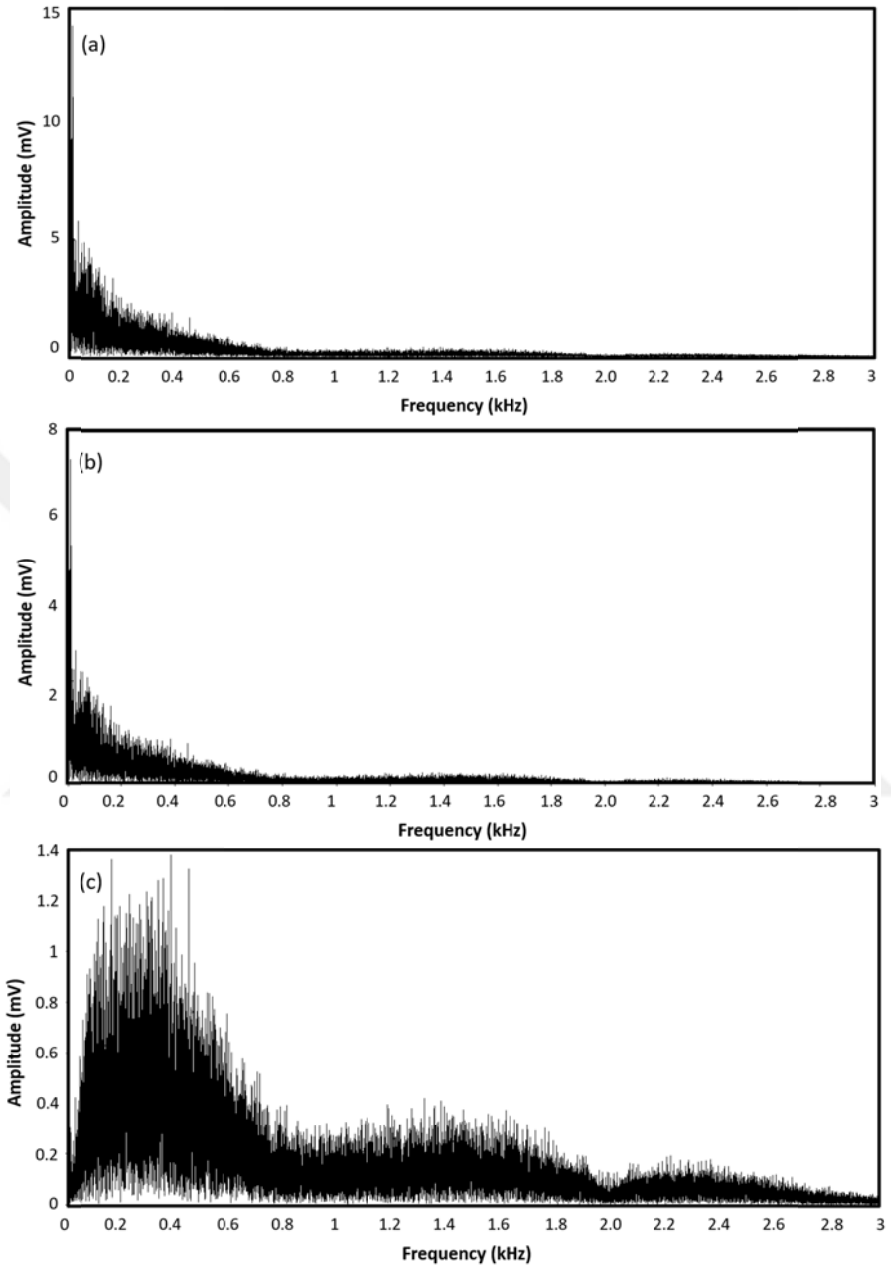

Figure 8.9. Fourier transforms of the EMG signal output for (a) Proposed electrode, (b) Wet electrode on prepared skin (c) Wet electrode on unprepared skin.

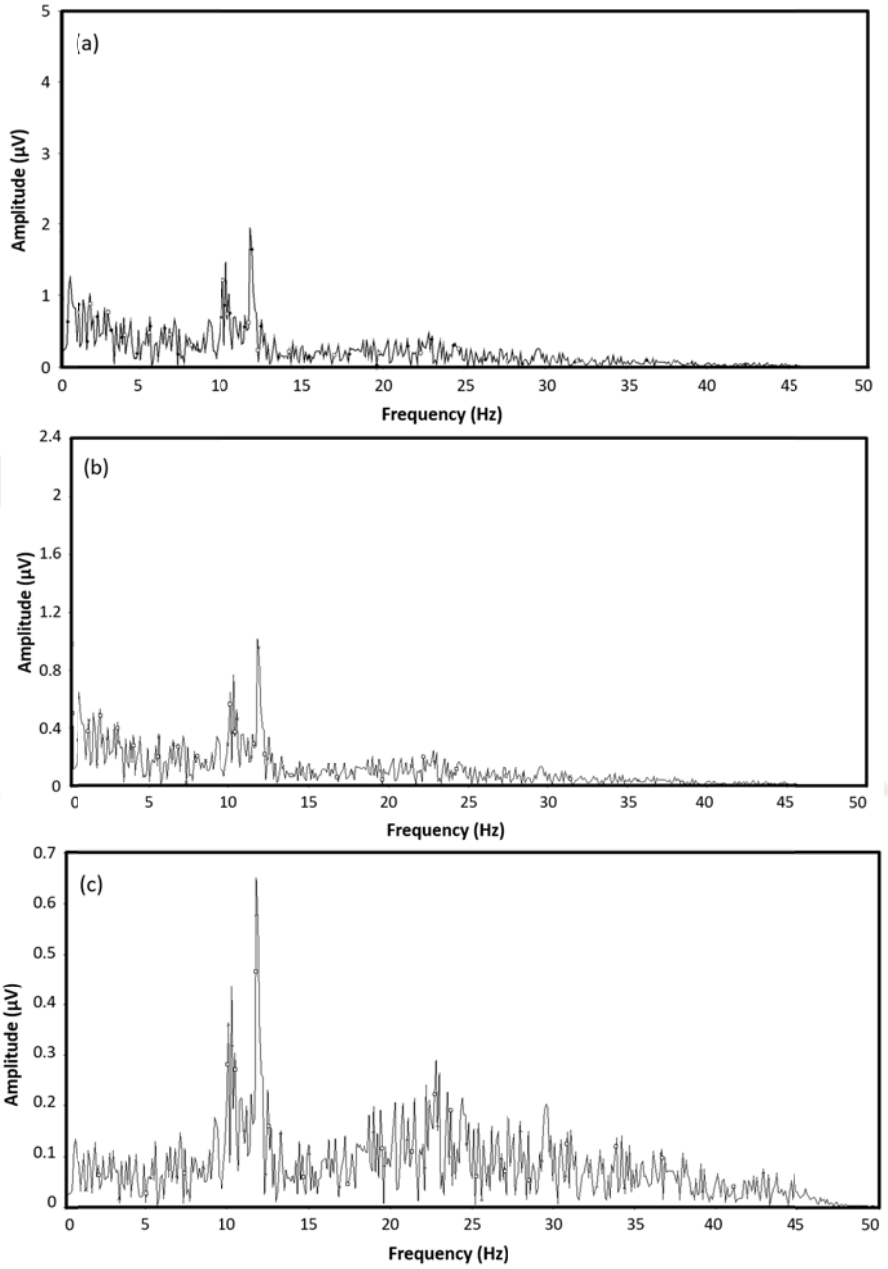

Figure 8.10. Fourier transforms of the EEG signal output for (a) Proposed electrode, (b) Wet electrode on prepared skin (c) Wet electrode on unprepared skin.

9. CONCLUSION

During electrophysiological signal acquisition on the skin, the dead layer stratum corneum affects the quality of the task. Electrolytic gel application and skin abrasions are popular solutions for signal quality improvement. However, these solutions have skin damaging or allergic reaction risks. Additionally, the electrolytic gel is not suitable for long-duration measurements. Needle-array-based solutions are alternative approaches to overcome the mentioned problems.

In this thesis, a novel MWCNT modified depletion type n-channel MOSFET-based electrophysiological active dry electrode is proposed. The vertically aligned MWCNT arrays are grown on the gate terminal of the MOSFET. The MWCNTs penetrate the stratum corneum skin layer at the microscales. This penetration eliminates the high impedance and noise effects of stratum corneum. They also provide more firm attachment and stable low impedance contact.

The microscale lengths of MWCNT minimize pain and infection risks. The properties of MWCNT do not contain any substances that are toxic to living tissues. On the other hand, an application specific MOSFET device is designed and simulated. The MOSFET provides direct charge–current conversion, high dielectric insulation of gate oxide, and low noise pre-amplification on the signal.

The effects of stratum corneum layer and the conductive electrolytic gel on the obtained biopotentials are shown in the simulation results given in previous chapters. SC layer on the human skin exhibits resistive/capacitive medium properties that lead to a voltage drop at the output of the electrode. Comparison of simulations for case-1 and case-2 proves this phenomenon. Although conductive gel reduces the significant decrease in signal amplitude, it cannot completely prevent the distortion and noise on the signal, since it cannot completely eliminate the effect of the SC layer. In contrast with the wet electrode cases, the proposed electrode simulated for unprepared skin without conductive gel. Although it is simulated at the worst case specifications, the proposed model obtained the highest

quality signals. As shown in the Fourier transforms of the biopotential signal outputs, the signal to noise ratio of the proposed electrode is higher than that of the wet electrodes. The simulation results demonstrate and prove the efficiency of the proposed electrode.

This electrode increases signal acquisition quality, reduces the noise from the stratum corneum skin layer, eliminates electrolytic gel usage, and provides stable impedance for long periods. The simulations demonstrate the efficiency and importance of the electrode. This electrode may be used for abrasion and gel-free electrophysiological signal acquisition even for long-term measurements without biocompatibility problems.

REFERENCES

AboBakr, A., Mohsen, M., Said, L. A., Madian, A. H., Elwakil, A. S., Radwan, A. G. (2019). Toward Portable Bio-impedance devices. 2019 Fourth International Conference on Advances in Computational Tools for Engineering Applications (ACTEA), 1–4.

Abu-saude, M., Consul-Pacareu, S., Morshed, B. I. (2015). Feasibility of Patterned Vertical CNT for Dry Electrode Sensing of Physiological Parameters, IEEE Topical Conference on Biomedical Wireless Technologies, Networks, and Sensing Systems (BioWireleSS), San Diego, CA, pp. 1-4.

Abu-Saude, M. J., Morshed, B. I. (2015). Patterned Vertical Carbon Nanotube Dry Electrodes for Impedimetric Sensing and Stimulation. IEEE Sensors Journal, 15(10), 5851–5858.

Ain, K., Wibowo, R. A., Soelistiono, S., Muniroh, L. (2018). Measurement of Cholesterol Concentration Based on Bioimpedance with AD5933-EVAL. Proceedings of 5th International Conference on Instrumentation, Communications, Information Technology, and Biomedical Engineering, ICICI-BME, pp. 251–254.

Allen, P. E., Holberg, D. R. (2016). CMOS Analog Circuit Design. Oxford University Press Inc., USA.

Analog Devices. (2017). AD5933, 40. Retrieved from www.analog.com

Assambo, C., Baba, A., Dozio, R., Burke, M. J. (2007). Determination of the Parameters of the Skin-Electrode Impedance Model for ECG Measurement. Proceedings of the 6th WSEAS International Conference on Electronics, Hardware, Wireless and Optical Communications. Stevens Point, Wisconsin, USA: World Scientific and Engineering Academy and Society (WSEAS). pp. 90–95

Baker, R. J. (2019). CMOS: Circuit Design, Layout, and Simulation. IEEE Press Series on Microelectronic Systems, Wiley.

Bakr, A. A., Radwan, A. G., Madian, A. H., Elwakil, A. S. (2016). Aging effect on apples bio-impedance using AD5933. 3rd International Conference on Advances in Computational Tools for Engineering Applications, ACTEA 2016, 158–161.

Banerjee, K., & Srivastava, N. (2006). Are carbon nanotubes the future of VLSI interconnections? Proceedings of the 43rd annual conference on Design automation (DAC '06), New York, USA: ACM Press. pp. 809

Bard, A. J., Faulkner, L. R., York, N., Bullet, C., Brisbane, W., Toronto, S. E. (1944). Electrochemical Methods: Fundamentals and Applications. 2nd Edition.

Bourlon, B., Miko, C., Forró, L., Glattli, D. C., Bachtold, A. (2004). Determination of the Intershell Conductance in Multiwalled Carbon Nanotubes. Physical Review Letters, 93(17), 176806.

Breniuc, L., David, V., Haba, C. G. (2014). Wearable impedance analyzer based on AD5933. EPE 2014 - Proceedings of the 2014 International Conference and Exposition on Electrical and Power Engineering, 585–590.

Broeders, J., Duchateau, S., Van Grinsven, B., Vanaken, W., Peeters, M., Cleij, T., Ceuninck, W. (2011). Miniaturised eight-channel impedance spectroscopy unit as sensor platform for biosensor applications. Physica Status Solidi (A), 208(6), 1357–1363.

Burke, P. J. (2002). Luttinger liquid theory as a model of the gigahertz electrical properties of carbon nanotubes. IEEE Transactions On Nanotechnology, 1(3), 129–144.

Charlier, J.-C., Roche, S. (2007). Electronic and transport properties of nanotubes. Reviews of Modern Physics, 79(2), 677–732.

Chen, C. J., Liu, J. T., Chang, S.-J., Lee, M.-W., Tsai, J.-Z. (2012). Development of a portable impedance detection system for monitoring the growth of mouse L929 cells. Journal of the Taiwan Institute of Chemical Engineers, 43(5), pp. 678–684.

Chen, X., Li, S., Han, F., Du, M. (2019). Research of impedance measurement system based on adaptive feedback calibration method. Proceedings of 2019 IEEE 3rd Information Technology, Networking, Electronic and Automation Control Conference, ITNEC 2019, pp. 1521–1525.

Chi, Y. M., Jung, T., Cauwenberghs, G. (2010). Dry-Contact and Noncontact Biopotential Electrodes: Methodological Review. IEEE Reviews in Biomedical Engineering, 3, pp. 106–119.

Chiou, J.-C., Ko, L.-W., Lin, C.-T., Hong, C.-T., Jung, T.-P., Liang, S.-F., Jeng, J.-L. (2006). Using novel MEMS EEG sensors in detecting drowsiness application. IEEE Biomedical Circuits and Systems Conference, pp. 33–36.

Council, E. E. (2011). Electrode Contact Impedance And Biopotential Signal Quality, MSc Thesis, Tampere University of Technology.

Cui, Z. (2009). Nanofabrication: Principles, Capabilities and Limits. Springer US.

Datta, S. (2005). Quantum Transport : Atom to Transistor. Cambridge University Press, Cambridge.

Fediai, A., Ryndyk, D. A., Cuniberti, G. (2015). Electron transport in extended carbon-nanotube/metal contacts: Ab initio based Green function method. Physical Review B - Condensed Matter and Materials Physics, 91(16), pp. 1–11.

Ferreira, J., Seoane, F., Lindecrantz, K. (2011). AD5933-based electrical bioimpedance spectrometer. Towards textile-enabled applications. Proceedings of the Annual International Conference of the IEEE Engineering in Medicine and Biology Society, EMBS, pp. 3282–3285.

Ferreira, J., Seoane, F., Lindecrantz, K. (2013). Portable bioimpedance monitor evaluation for continuous impedance measurements. Towards wearable plethysmography applications. Proceedings of the Annual International Conference of the IEEE Engineering in Medicine and Biology Society, EMBS, pp. 559–562.

Franssila, S. (2010). Introduction to Microfabrication. Wiley-Blackwell, 2nd Edition.

Gargiulo, G., Bifulco, P., Calvo, R. A., Cesarelli, M., Jin, C., Van Schaik, A. (2008). Mobile biomedical sensing with dry electrodes. ISSNIP 2008 - Proceedings of the International Conference on Intelligent Sensors, Sensor Networks and Information Processing, pp. 261–266.

Geddes, L. A., Baker, L. E. (1970). Principles of Applied Biomedical Instrumentation. The Quarterly Review of Biology, 45(2), pp. 230–231.

Grimnes;, S. (2014). Bioimpedance And Bioelectricity Basics. Academic Press, 3rd Edition

Griss, P., Enoksson, P., Tolvanen-Laakso, H. K., Merilainen, P., Ollmar, S., Stemme, G. (2001). Micromachined electrodes for biopotential measurements. Journal of Microelectromechanical Systems, 10(1), pp. 10–16.

Grozea, C., Voinescu, C. D., Fazli, S. (2011). Bristle sensors low-cost flexible passive dry EEG electrodes for neurofeedback and BCI applications. Journal of Neural Engineering, 8(2), 025008.

Hanson, G. W. (2008). Fundamentals of Nanoelectronics. Pearson/Prentice Hall.

Harris, P. J. F. (1999). Carbon nanotubes and related structures: new materials for the twenty-first century, Cambridge University Press. 294.

Hoja, J., Lentka, G. (2013). A Family of New Generation Miniaturized Impedance Analyzers for Technical Object Diagnostics. Metrology and Measurement Systems, 20(1), pp. 43–52.

Hu, Z., Ramalingame, R., Kallel, A. Y., Wendler, F., Fang, Z., Kanoun, O. (2020). Calibration of an AC Zero Potential Circuit for Two-Dimensional Impedimetric Sensor Matrices. IEEE Sensors Journal, 20(9), pp. 5019–5025.

Huigen, E., Peper, A., Grimbergen, C. (2002). Investigation into the origin of the noise of surface electrodes. Medical & Biological Engineering & Computing, 40, pp. 332–338.

Ibba, P., Falco, A., Rivadeneyra, A., Lugli, P. (2018). Low-Cost Bio-Impedance Analysis System for the Evaluation of Fruit Ripeness. Proceedings of IEEE Sensors, pp. 1–4.

Istanbullu M., A. M. (2019). Microfabrication Process Design of Low Voltage Depletion Type N-MOSFET for Biopotential Sensing. 5th International Conference on Materials Science and Nanotechnology For Next Generation (MSNG2018), Nevşehir, pp. 117–121

Istanbullu, M., Avci, M. (2019). Novel multiwalled carbon nanotube (MWCNT) modified metal oxide semiconductor field effect transistor (MOSFET) based electrode for electrophysiological measurements on human skin. Instrumentation Science & Technology, 47(5), pp. 545–563.

Janz, G., Ives, D. (1968). Silver-silver chloride electrodes. Ann NY Acad Sci, 148, pp. 210–221.

Jung, H. C., Moon, J. H., Baek, D. H., Lee, J. H., Choi, Y. Y., Hong, J. S., Lee, S. H. (2012). CNT/PDMS composite flexible dry electrodesfor long-term ECG monitoring. IEEE Transactions on Biomedical Engineering, 59(5), pp. 1472–1479.

Kaczmarek, K. A., Webster, J. G. (1989). Voltage-current characteristics of the electrotactile skin-electrode interface. Images of the Twenty-First Century. Proceedings of the Annual International Engineering in Medicine and Biology Society, vol.5. pp. 1526–1527

Kelly, B. T. (1981). Physics of graphite. Acta Cryst. A39, 192, Applied Science Publishers, London.

Kordrostami, Z., Sheikhi, M. H., Mohammadzadegan, R. (2008). Modeling electronic properties of multiwall carbon nanotubes. Fullerenes Nanotubes and Carbon Nanostructures, 16(1), pp. 66–77.

Korostynska, O., Arshak, K., Gill, E., Arshak, A., Kaneswaran, K. (2008). Bi2O3/Nb2O5 thick film capacitive pH sensor using AD5933 impedance converter. 2008 IEEE Sensors Applications Symposium, SAS-2008.

Krueger, A. (2014). Carbon Materials and Nanotechnology. Wiley-VCH, Weinheim

Li, H. J., Lu, W. G., Li, J. J., Bai, X. D., Gu, C. Z. (2005). Multichannel Ballistic Transport in Multiwall Carbon Nanotubes. Physical Review Letters, 95(8), 086601.

Li, H., Yin, W.-Y., Banerjee, K., Mao, J.-F. (2008). Circuit Modeling and Performance Analysis of Multi-Walled Carbon Nanotube Interconnects. IEEE Transactions on Electron Devices, 55(6), pp. 1328–1337.

Liu, H., Liu, W. D. (2010). Low-power and portable design of bioelectrical impedance measurement system. Proceedings - 2010 WASE International Conference on Information Engineering, ICIE 2010, 3, pp. 38–41.

LIU, Y.-L., LIN, D.-L., LIN, Y.-D. (2004). Spice Model for Computer-Aided Design of Biopotential Amplifier. Biomedical Engineering: Applications, Basis and Communications, 16(03), pp. 151–156.

Lu, F., Wang, C., Zhao, R., Du, L., Fang, Z., Guo, X., Zhao, Z. (2018). Review of Stratum Corneum Impedance Measurement in Non-Invasive Penetration Application. Biosensors, 8(2), 31.

Margo, C., Katrib, J., Nadi, M., Rouane, A. (2013). Four electrode embedded bioimpedance measurement system. 2013 IEEE Faible Tension Faible Consommation, FTFC 2013, pp. 1–4.

May, G. S., Spanos, C. J. (2006). Introduction to Semiconductor Manufacturing. In Fundamentals of Semiconductor Manufacturing and Process Control pp. 1–24. John Wiley & Sons, Ltd.

May, G. S., Sze, S. M. (2004). Fundamentals of Semiconductor Fabrication. Wiley, 1st Edition

McAdams, E. T., Jossinet, J. (2000). Nonlinear transient response of electrode—electrolyte interfaces. Medical and Biological Engineering and Computing, 38(4), pp. 427–432.

McAdams, E. T., Jossinet, J., Lackermeier, A., Risacher, F. (1996). Factors affecting electrode-gel-skin interface impedance in electrical impedance tomography. Medical and Biological Engineering and Computing, 34(6), pp. 397–408.

McLaughlin, J. A., McAdams, E. T., Anderson, J. (1994). Novel dry electrode ECG sensor system. In Proceedings of 16th Annual International Conference of the IEEE Engineering in Medicine and Biology Society. Vol. 2, pp. 804.

Melwin, A., Rajasekaran, K. (2013). Implementation of Bioimpedance Instrument Kit in ARM7. International Journal of Advanced Research in Computer Science and Software Engineering, 3(5), pp. 1271–1273.

Mestrovic, M. A., Helmer, R. J. N., Kyratzis, L., Kumar, D. (2007). Preliminary study of dry knitted fabric electrodes for physiological monitoring. Proceedings of the 2007 International Conference on Intelligent Sensors, Sensor Networks and Information Processing, ISSNIP, pp. 601–606.

Meyyappan, M. (2005). Carbon nanotubes : science and applications. Boca Raton, FL, CRC Press

Naeemi, A., Mein, J. D. (2006). Compact physical models for multiwall carbon-nanotube interconnects. IEEE Electron Device Letters, 27(5), pp. 338–340.

Neamen, D. A. (2012). Semiconductor physics and devices : basic principles. Homewood, IL: Irwin.

Neuman, M. (2010). Biopotential Electrodes. In J. Webster (Ed.), Medical Instrumentation Application and Design (Fourth Edi, pp. 189–240). Wiley.

Nordbotten, B. J. (2008). Bioimpedance Measurements Using the Integrated Circuit AD5933, MSc Thesis, University of Oslo

Papadopoulos, C. (2016). Nanofabrication: Principles and Applications. Springer International Publishing.

Park, J. Y., Rosenblatt, S., Yaish, Y., Sazonova, V., Üstunel, H., Braig, S., McEuen, P. L. (2004). Electron-phonon scattering in metallic single-walled carbon nanotubes. Nano Letters, 4(3), pp. 517–520.

Plonsey, R., Barr, R. C. (2007). Bioelectricity: A Quantitative Approach. Springer US, 3rd Edition.

Prelas, M. A., Popovici, G., Bigelow, L. K. (1998). Handbook of industrial diamonds and diamond films. CRC Press.

Punapung, A., Kaewpoonsuk, A. (2019). A Design for a Programmable Swept Frequency Module for Eddy Current Testing. IEECON 2018 - 6th International Electrical Engineering Congress, pp. 1–4.

Reich, S., Thomsen, C., Maultzsch, J. (2004). Carbon Nanotubes. Basis Concepts and Physical Properties. Angewandte Chemie International Edition. Vol. 43.

Rubi, J. M., Kjelstrup, S. (2003). Mesoscopic Nonequilibrium Thermodynamics Gives the Same Thermodynamic Basis to Butler−Volmer and Nernst Equations. The Journal of Physical Chemistry B, 107(48), pp. 13471–13477.

Ruffini, G., Dunne, S., Farrés, E., Marco-Pallarés, J., Ray, C., Mendoza, E., Grau, C. (2006). A dry electrophysiology electrode using CNT arrays. Sensors and Actuators A: Physical, 132(1), pp. 34–41.

S Datta. (2012). Lessons From Nanoelectronics. World Scientific Publishing, 2nd Edition

Saito, R., Dresselhaus, G., Dresselahus, (1998). Physical Properties of Carbon Nanotubes. Imperial College Press.

Schomer, D. L., da Silva, F. H. L. (2017). Niedermeyer's Electroencephalography Basic Principles, Clinical Applications, and Related Fields. Oxford, UK: Oxford University Press.

Searle, A., Kirkup, L. (2000). A direct comparison of wet, dry and insulating bioelectric recording electrodes. Physiological Measurement, 21(2), pp. 271–283.

Seoane, F., Ferreira, J., Sanchéz, J. J., Bragós, R. (2008). An analog front-end enables electrical impedance spectroscopy system on-chip for biomedical applications. Physiological Measurement, 29(6), pp. 267–278.

Shlyakhotka, A. V., Lyakhova, E. K., Sutyagina, A. D. (2018). Design of a device for determining stroke volume by the impedance cardiography method. Proceedings of the IEEE Conference of Russian Young Researchers in Electrical and Electronic Engineering, ElConRus 2018, Janua, pp. 1225–1226.

Simic, M. (2013). Realization of complex impedance measurement system based on the integrated circuit AD5933. 2013 21st Telecommunications Forum Telfor, TELFOR 2013 - Proceedings of Papers, (289481), pp. 573–576.

Simic, M. (2014). Realization of digital LCR meter. EPE 2014 - Proceedings of the 2014 International Conference and Exposition on Electrical and Power Engineering, (289481), pp. 769–773.

Simic, M., Stojanovic, G. M., Manjakkal, L., & Zaraska, K. (2017). Multi-sensor system for remote environmental (air and water) quality monitoring. 24th Telecommunications Forum, TELFOR 2016, pp. 5–8.

Singh, R., Colombo, L., Schuegraf, K., Doering, R., Diebold, A. (2013). Semiconductor Manufacturing. In Guide to State-of-the-Art Electron Devices. John Wiley & Sons, Ltd. pp. 121–132.

Snajdarova, M., Borik, S., Cap, I. (2017). Design of measurement device for impedance cardiography. Proceedings of 18th International Conference on Computational Problems of Electrical Engineering, CPEE 2017.

Stepanova, M., Dew, S. (2011). Nanofabrication: Techniques and Principles. Springer, Vienna.

Thakor, N. V. (2014). Biopotentials and Electrophysiology Measurement, Telehealth and Mobile Health. Boca Raton. CRC Press.

Toazza, A. L., Mendes de Azevedo, F., Neto, J. M. (1998). Microcontrolled system for measuring skin/electrode impedance in bioelectrical recordings. Proceedings of IEEE International Caracas Conference on Devices, Circuits and Systems. ICCDCS 98. pp. 278–281

Valchinov, E. S., Pallikarakis, N. E. (2004). An active electrode for biopotential recording from small localized bio-sources. Biomedical Engineering Online, 3(1), 25.

Wang, L.-F., Liu, J.-Q., Yang, B., Yang, C.-S. (2012). PDMS-Based Low Cost Flexible Dry Electrode for Long-Term EEG Measurement. IEEE Sensors Journal, 12(9), pp. 2898–2904.

Webster, J. G. (2006). Encyclopedia of Medical Devices and Instrumentation. Hoboken, NJ, USA: John Wiley & Sons, Inc.

Webster, J. G., Clark, J. W. (2010). Medical instrumentation : application and design. Hoboken, NJ: John Wiley & Sons.

Weste, N. H. E., Eshraghian, K. (1993). Principles of CMOS VLSI Design: A Systems Perspective. Addison-Wesley Publishing Company.

Xie, L., Yang, G., Mäntysalo, M., Xu, L. L., Jonsson, F., Zheng, L. R. (2012). Heterogeneous integration of bio-sensing system-on-chip and printed electronics. IEEE Journal on Emerging and Selected Topics in Circuits and Systems, 2(4), pp. 672–682.

Yamacli, S., Avci, M. (2009). Simple and accurate model for voltage–dependent resistance of metallic carbon nanotube interconnects: An ab initio study. Physics Letters A, 374(2), pp. 297–304.

Yang, Y., Zhang, W., Sun, Q. (2014). Design and preliminary test of a palm bio-impedance spectroscopy measurement system for biometric authentication. Proceedings - 2014 International Symposium on Computer, Consumer and Control, IS3C 2014, pp. 824–827.

Yazicioglu, R. F., Hoof, C. Van, Puers, R. (2008). Biopotential Readout Circuits for Portable Acquisition Systems (1st ed.). Springer Publishing Company, Incorporated.

Yoo, C. S. (2008). Semiconductor Manufacturing Technology. World Scientific Publishing Company.

Yoo, J., Yan, L., Lee, S., Kim, H., Kim, B., Yoo, H. J. (2009). An attachable ECG sensor bandage with planar-fashionable circuit board. Proceedings - International Symposium on Wearable Computers, ISWC, pp. 145–146.

Zhao, J., Hao, Z., Fu, W., & Zou, X. (2016). Design and implementation of multi-parameter portable biological information measurement system. Proceedings of the 28th Chinese Control and Decision Conference, CCDC 2016, pp. 3762–3765.

Zhivkov, I., Yordanov, R., Dobrikov, G., Yordanova, I., & Weiter, M. (2019). Computer Controlled System for Impedance Measurements. 2019 42nd International Spring Seminar on Electronics Technology (ISSE), pp. 1–5.

BIOGRAPHY

Mustafa İSTANBULLU was born in Çorum in 1988. He graduated from Çorum Anadolu Öğretmen High School in 2006 and entered the Electrical and Electronics Engineering Department at Erciyes University in the same year. He joined the Biomedical Engineering master's program at İstanbul Technical University in 2010 and completed in 2013. Between 2010 and 2013, he worked as an instructor at İstanbul Aydın University. He started his PhD education in the Electrical and Electronics Engineering Department at Çukurova University in 2013. He has been working as a research assistant in the Biomedical Engineering Department at Çukurova University since 2013.

APPENDIX

```
#Microfabrication of n-type Depletion Mode MOSFET
#Starting Athena
go Athena
#Defining Mesh
line x loc=0.0 spacing=0.1
line x loc=0.5 spacing=0.006
line x loc=1.2 spacing=0.006
line y loc=0.0 spacing=0.002
line y loc=0.2 spacing=0.005
line y loc=0.5 spacing=0.05
line y loc=0.8 spacing=0.15
#Initilize Mesh
init silicon orientation=100 c.phos=1e14 space.mul=2 two.d
#Depositing  Screening Oxide (15-25nm) to decrease the channeling effect
and to prevent contamination with substrate
diffuse time=30 temp=1000 dryo2 press=1.00 hcl=3
structure outfile=m1.str
etch oxide thick=0.02
# P-Well Implantation
implant boron dose=8e12 energy=100 pears
structure outfile=m3.str
tonyplot -st m3.str
#Well oxidation
diffuse temp=950 time=100 weto2 hcl=3
structure outfile=m4.str
tonyplot -st m4.str
#Drive-in
diffus time=50 temp=1000 t.rate=4.00 dryo2 press=0.10 hcl=3
diffus time=220 Temp=1200 nitro press=1
```

```
diffus time=90 temp=1200 t.rate=-4.444 nitro press=1
structure outfile=m5.str
tonyplot -st m5.str
#Oxide removal
etch oxide all
structure outfile=m6.str
tonyplot -st m6.str
#Tip or Extension(LDD-light doped drain) Formation
 implant phosphor dose=3.0e13 energy=20 pearson
structure outfile=mx.str
tonyplot -st mx.str
#Sacrificial Cleaning
diffus time=20 temp=1000 dryo2 press=1 hcl=3
etch oxide all
#Depositing gate oxide
diffus time=15 temp=925 dryo2 press=1.00 hcl=3
structure outfile=m8.str
tonyplot -st m8.str
#Threshold adjusting implantation
implant boron dose=9.5e11 energy=10 pearson
#Depositing polysilicon
depo poly thick=0.3 divi=10
etch poly left p1.x=0.95
structure outfile=m10.str
tonyplot -st m10.str
#Light drain/source doping
method fermi compress
diffuse time=3 temp=900 weto2 press=1.0
implant phosphor dose=3.0e13 energy=20 pearson
```

```
structure outfile=m11.str
tonyplot -st m11.str
#LPCVD step and anisotropic etching
rate.depo mach=SiLPCVD cvd oxide step.cov=0.6 dep.rate=0.1 u.m
deposit mach=SiLPCVD time=3.5 minute div=15
rate.etch mach=SiO2 rie oxide dir=0.15 iso=0.00 u.m
Etch mach=SiO2 time=140 second dx.mult=0.5
structure outfile=m12.str
tonyplot -st m12.str
#Heavy doping to form Source/Drain
implant arsenic dose=5.0e15 energy=50 pearson
structure outfile=m13.str
tonyplot -st m13.str
# Thermal annealing
method fermi compress
diffuse time=1 temp=1000 nitro press=1.0
#Contact opening
rate.depo mach=SiLPCVD cvd oxide step.cov=0.6 dep.rate=0.1 u.m
deposit mach=SiLPCVD time=3.5 minute div=15
etch oxide left p1.x=0.5
structure outfile=m15.str
#tonyplot -st m15.str
#Metal deposition
rate.depo machine=SputteringAl aluminum n.m sigma.dep=0.80 uni
dep.rate=100 angle1=60
deposit machine=SputteringAl time=3.5 minutes div=50
etch aluminum right p1.x=0.6
#Mirroring
structure mirror right
```

```
#Definitions of terminals
electrode name=gate x=1.2 y=0.1
electrode name=source x=0.1
electrode name=drain x=2.3
electrode name=substrate backside
structure outfile=nmos.str
tonyplot -st nmos.str
#Extracting threshold voltage
extract name="n1dvt" 1dvt ntype vb=0.0 qss=1e10 x.val=1.2
#Starting Atlas to obtain electrical characteristic curves
go atlas
contact name=gate n.poly
contact name=drain aluminum
interface qf=3e10
models cvt srh print
solve init
#For Id-Vd curve
solve vgate=1.1 outfile=solve1_1
solve vgate=2.2 outfile=solve2_2
solve vgate=3.3 outfile=solve3_3
load infile=solve1_1
log outfile=NMOSvg1_1.log
solve name=drain vdrain=0 vfinal=3.3 vstep=0.3
load infile=solve2_2
log outfile=NMOSvg2_2.log
solve name=drain vdrain=0 vfinal=3.3 vstep=0.3
load infile=solve3_3
log outfile=NMOSvg3_3.log
solve name=drain vdrain=0 vfinal=3.3 vstep=0.3
```

```
tonyplot -overlay NMOSvg1_1.log NMOSvg2_2.log NMOSvg3_3.log
#For Id-Vg curve
solve vdrain=0.2 outfile=solve0_2
solve vdrain=0.4 outfile=solve0_4
solve vdrain=0.6 outfile=solve0_6
load infile=solve0_2
log outfile=NMOSvd0_2.log
solve name=gate vgate=-10 vfinal=10 vstep=0.2
load infile=solve0_4
log outfile=NMOSvd0_4.log
solve name=gate vgate=-10 vfinal=10 vstep=0.2
load infile=solve0_6
log outfile=NMOSvd0_6.log
solve name=gate vgate=-10 vfinal=10 vstep=0.2
tonyplot -overlay NMOSvd0_2.log NMOSvd0_4.log NMOSvd0_6.log
quit
```